Prestrain effect of anisotropic ductile damage in API grade X100 line pipe steel

Yasuhiro Shinohara

ParisTech
INSTITUT DES SCIENCES ET TECHNOLOGIES
PARIS INSTITUTE OF TECHNOLOGY

MINES ParisTech

École doctorale n° 432 : Sciences des Métiers de l'Ingénieur

Doctorat ParisTech

T H È S E

pour obtenir le grade de docteur délivré par

l'École nationale supérieure des mines de Paris

Spécialité « Science et Génie des Matériaux »

Yasuhiro SHINOHARA

thèse soutenue le 3 Mars 2014

Prestrain effect on anisotropic ductile damage in API grade X100 line pipe steel

Effet d'une pré-déformation sur l'endommagement anisotrope d'un acier pour pipeline de grade API X100

Directeur de thèse: **Jacques BESSON**
Maître de thèse: **Yazid MADI**

Jury

M. Zhiliang ZHANG	Professeur, NTNU (Norway)	Président
Mme Anne-Marie HABRAKEN	Professeur, Université de Liège	Rapporteur
Mme Sandrine THUILLIER	Professeur, Université Bretagne-Sud	Rapporteur
M. Tudor BALAN	Professeur, Arts et Métiers ParisTech, Metz	Examinateur
M. Jacques BESSON	Directeur de Recherche, Mines ParisTech	Examinateur
M. Yazid MADI	Enseignant-chercheur, Ermess, EPF-Ecole d'ingénieurs	Examinateur

T H È S E

MINES ParisTech
Centre des Matériaux - UMR CNRS 7633
B.P. 87 - 91003 EVRY Cedex

Contents

List of Figures

List of Tables

Acknowledgements

I would like to express my deepest gratitude to my academic supervisors Professor J. Besson and Dr Y. Madi for their great encouragement, all members of the Mechanics and Materials group for their advice and all staffs of the Technical Divisions for their kind support.

I am particularly grateful to Dr A. Yoshie and Dr T. Hara from Nippon Steel Corporation (now Nippon Steel & Sumitomo Metal Corporation) for giving me the opportunity to study at Ecole des Mines de Paris.

I would like to thank Dr E. Tsuru for fruitful discussions and valuable suggestions, which helped in conducting finite element simulation of pipe bending experiments.

I would like also to thank Mr K. Nagai for his kind help with experimetanl work at Nippon Steel Corporation.

I gratefully appreciate the Personnel Division of Nippon Steel Corporation for a grant and a finacial support that made it possible to complete this study.

Finaly, I wish to express my gratitude to Junko, my wife, for her dedicated support to my life in Paris. I am also grateful my daughters, Ayane and Seina, for their encouragement.

Chapter -I-

Introduction

Contents

Résumé en français :

Les aciers à haute résistance sont de plus en plus utilisés pour réduire les coûts d'exploitation des gazoducs et satisfaire la demande grandissante en énergie fossile (gaz naturel et pétrole). L'anisotropie de comportement finale des pipelines, liée au de procédé de fabrication des tubes (laminage d'une tôle suivi d'un formage UOE, par exemple), affecte le comportement en service. Plusieurs études montrent notamment que la charge limite de flexion, caractéristique importante du fait des mouvements de terrain auxquels sont soumis les pipelines dans les zones arctiques, est grandement affectée par l'anisotropie. Cette charge limite est évaluée par des règles de « Strain Based Design » tirant partie de la plasticité du matériau (conception basée sur la déformation) contrairement au cas classique basé sur des règles de « Stress Based Design » (conception basée sur la contrainte).

L'objectif premier de la thèse est de mieux comprendre l'anisotropie plastique et la ténacité des aciers à haute résistance pour pipelines. Une seconde étape consistera à développer un modèle phénoménologique capable de modéliser le comportement et l'endommagement de la nuance X100.

Cette thèse contient sept chapitres. Après cette introduction (chapitre 1), le chapitre 2 présente le matériau de l'étude (X100) et traite des procédures expérimentales. Les principaux résultats de la thèse sont abordés au travers des quatre autres chapitres, écrits sous forme de d'articles de journaux. Le chapitre 3 présente un modèle phénoménologique d'anisotropie plastique combinant les écrouissages isotrope et cinématique qui permet de rendre compte du comportement ductile de cet acier à haute résistance. Une application du modèle est alors réalisée pour déterminer le moment de flexion d'une structure tubulaire en présence d'un défaut. Le travail expérimental

effectué sur l'effet de la pré-déformation sur la ductilité et ténacité dans une plaque d'acier X100 est présenté dans le chapitre 4. Le chapitre 5 traite du modèle d'endommagement anisotrope établi pour représenter l'anisotropie du matériau. Deux méthodologies sont abordées et discutées pour identifier les paramètres du modèle : calculs de cellules en utilisant le modèle de plasticité anisotrope et identification sur la base des essais sur éprouvettes entaillées. La validation du modèle est alors réalisée par la simulation des éprouvettes fissurées CT et SENB. Le chapitre 6 reprend les simulations du chapitre 4 démontrant l'effet de pré-déformation avec cette fois l'application du modèle « complet » (plasticité anisotrope avec écrouissage isotrope et cinématique et endommagement anisotrope). Le chapitre 7 présente enfin les conclusions de la thèse.

I.1 Background

I.1.1 Demand for high strength steel linepipe

While consumption of energy is increasing worldwide as illustrated in Figure I.1 [IEA 2009], the demand for global environmental preservation becomes strong. Natural gas is the cleanest of all the fossil fuels because the combustion of natural gas releases lower level of carbon dioxides, compared with other fuels such as coal and oil. Thus demand for natural gas is rising in every regions of the world.

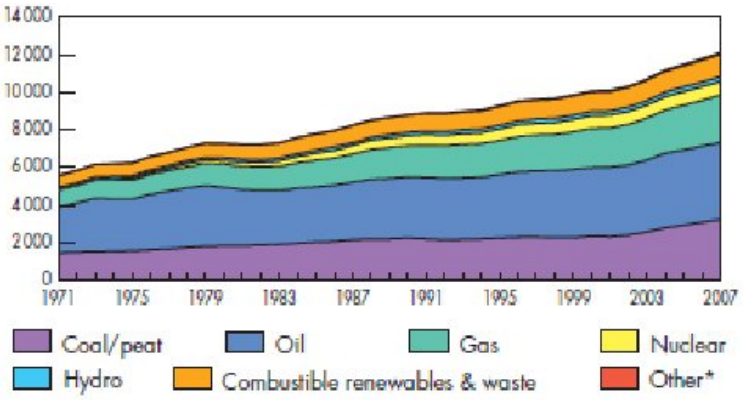

Figure I.1 : Change in world total primary energy supply

Pipelines have been a key component in the long-distance transportation of natural gas. Reduction in cost of the pipelines is one way to improve the economics of the gas transportation from the production area to consumers. Use of higher strength steel linepipes can make many benefits in pipe line projects, such as lower amount of steel required, lower transportation and lower laying costs. Figure I.2 shows change in pipe weight and pipe cost of X80, X100 and X120 grade steel linepipes for a given pipeline project [Asahi et al. 2009]. With respect to X80 grades, X120 linepipes have potential for pipe cost saving of about 15%. Furthermore, logistic and laying cost may be redued by more than 10% [Corbet et al. 2003]. X90, X100 and X120 high grade steel linepipes were standardized as ISO3183 and API 5L in 2007. X100 steel has already been manufactured in Japanese and European steel pipe mills for some comercial natural gas pipeline projects in Canada. X120 steel was also made in Japanese pipe works for small-scale laying tests and operational trails.

I.1.2 UOE Pipe process

Although there are various types of steel pipe process, UOE pipes are commonly used for natural gas pipeline structures. Figure I.3 illustrates the UOE pipe manufacturing process. The process consists of

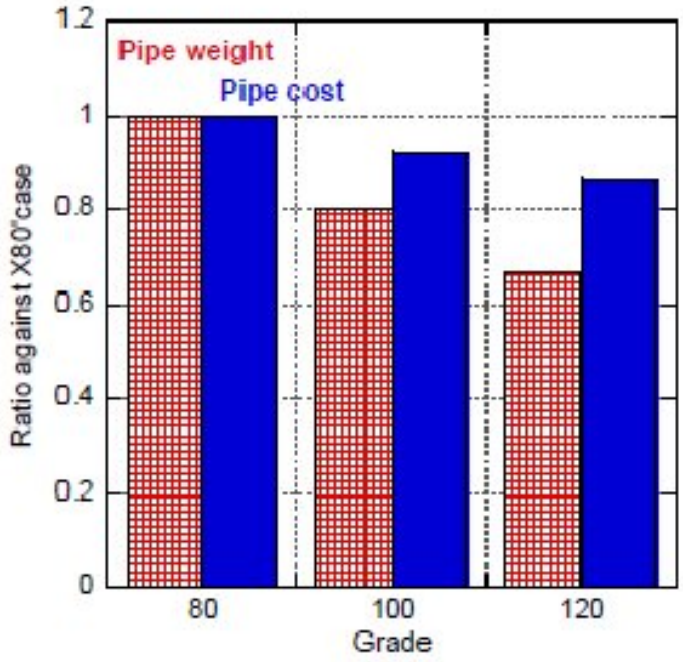

Figure I.2 : Comparison of pipe weight and cost among X80, X100 and X120 steels

two press forming steps such as U-ing and O-ing, welding stages including tack welding, inside seam and outside seam welding and a mechanical expansion. All the pressing and expansion processes are conducted in cold. Consequently, UOE pipes have anisotropic yield strength and plastic hardening as shown in Figure I.4 [Tsuru et al. 2005]. Moreover, UOE pipes have strength distribution along the circumferential direction. Figure I.5 demonstrates the fluctuation of a X80 grade UOE line pipe [Tsuru et al. 2008].

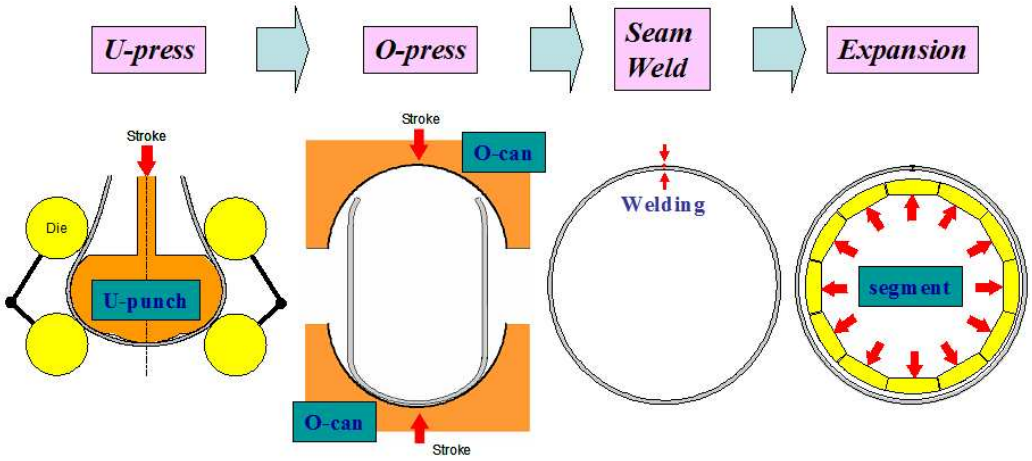

Figure I.3 : Schematic illustration of UOE pipe manufacturing process.

I.1.3 Strain-based design application

Development natural of gas fields are often far from major consumers because the potential locations are harsh environments. The main product fields are located in the Arctic area that includes Russia,

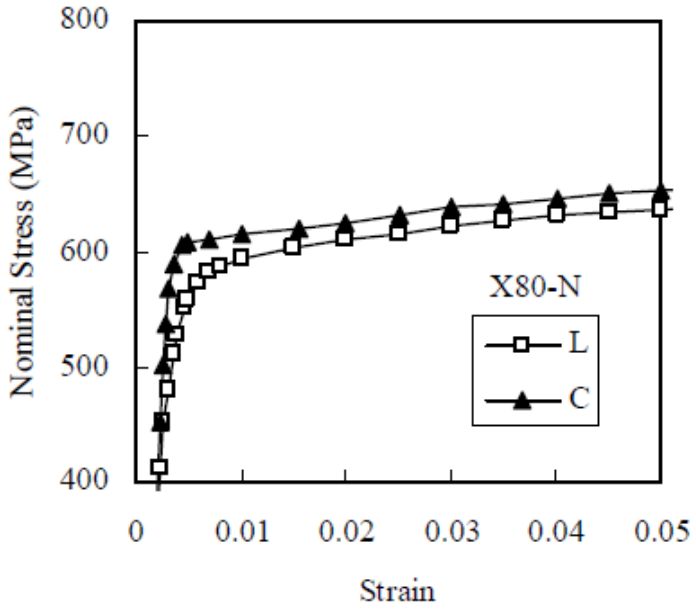

Figure I.4 : Nominal stress-strain curves of a X80 grade UOE linepipe.

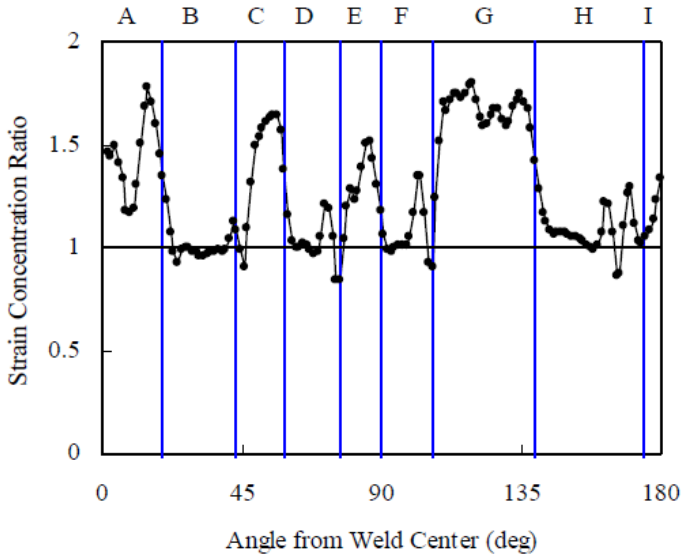

Figure I.5 : Strength distribution along the circumferential direction of a X80 grade UOE linepine.

Alaska in the U.S. and Canada. Figure I.6 shows a map of the North Pole dividing permafrost area into some regions such as isolated, sporadic, discontinuous and continuous one. Pipeline routes from Alaska or Far East of Russia inevitably pass through the discontinuous area to the consumers. Line pipes laid under the ground in the discontinuous permafrost are subjected to external load by as frost heave or thaw settlement, as shown in Figure I.7 [Lillig 2008]. Frost heave occurs due to ice forming under soil during freezing condition in winter. The event results in lifting the buried pipes. On the other hand, thaw settlement happens by unfreezing ice beneath soil in summer. The occurrence makes the linepipes go down.

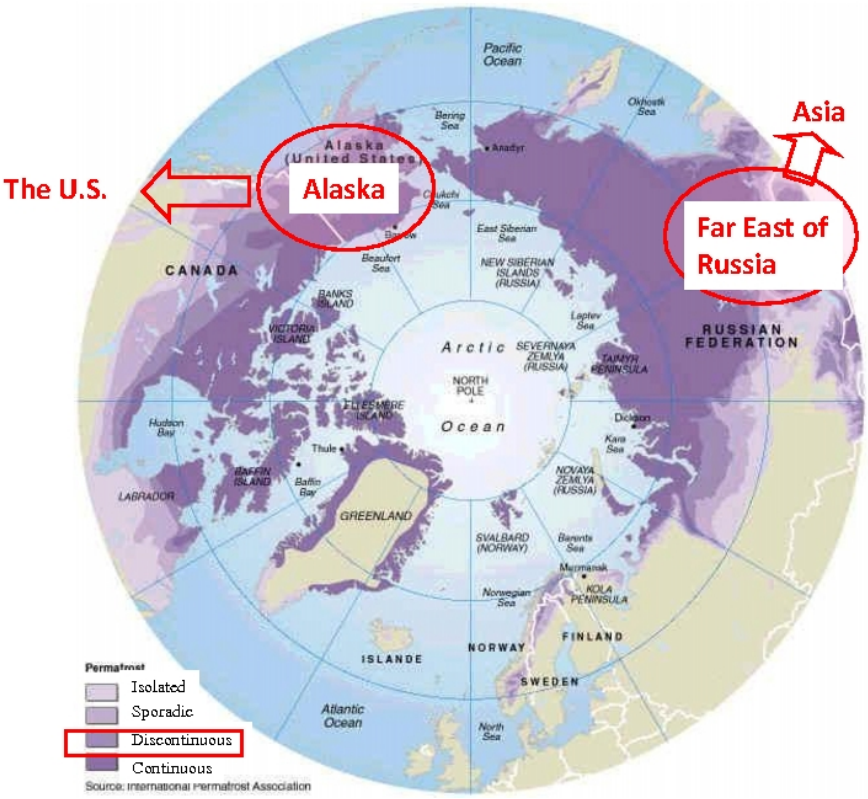

Figure I.6 : Distribution of discontinuous permafrost area in the Arctic region

The load events are usually displacement-controlled [Glover and Rothwell 2008]. Thus strain-based design (SBD) is essential to the harsh environment, while stress-based design of a pipeline is normally preferred. To achieve a safe and reliable pipeline operation in the harsh area, accurate prediction of the plastic strain imposed by the ground movement are required. Plastic bending deformation is applied to linepipes installed in such a field. In the SBD, the designers need to consider the imposed strain on both tensile and compressive sides of the bended pipe [Tsuru et al. 2008, Igi et al. 2008]. Normally, full size pipe bending tests are carried out to evaluate the strain limit for buckling on compressive point [Zimmerman et al. 1995], while curved wide plate tests are performed to predict the strain limit for ductile failure on the tension side [Fairchild et al. 2008]. Numerical simulations by finite element analysis are also conducted for specifying the effective mechanical properties of the tested pipes and checking the predicted values against the experimental results.

The detailed mechanical properties of a line pipe have been clarified in the previous works [Tsuru et al. 2008, Shinohara et al. 2008]. The line pipe has anisotropic hardening; a stress-strain curve is quite different between the longitudinal direction and the circumferential direction. The characteristic is mainly due to plastic strain developed in the pipe forming process. Furthermore, sharp texture of the mother plate, which is introduced during thermo mechanical control process (TMCP) at the plate mill,

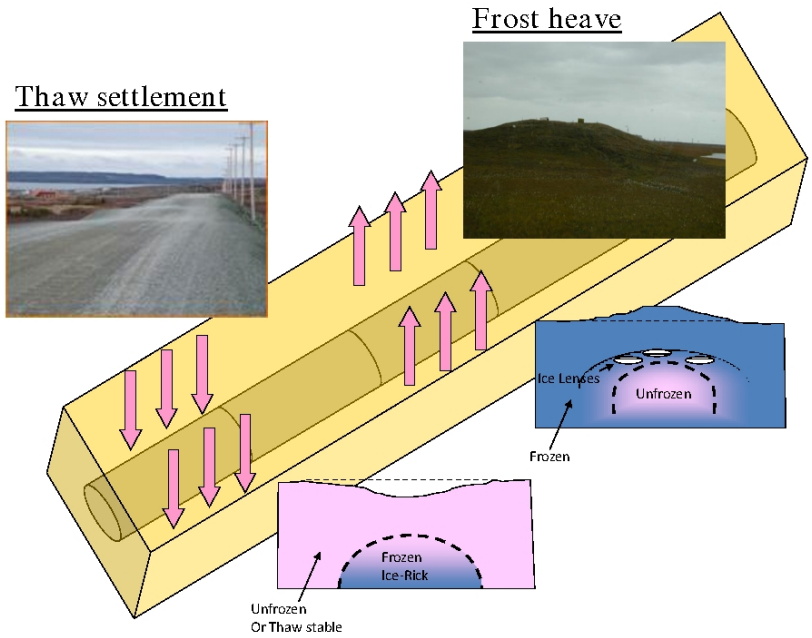

Figure I.7 : Schematic illustration of line pipe deformation due to thaw settlement or frost heave

encourages the anisotropy, especially in high strength line pipes (above X80 grade). Recently, It was pointed out that a buckling strain limit of the bended pipe is significantly affected by the anisotropic properties [Tsuru et al. 2008]. It was also reported that anisotropic hardening has an influence on ductile crack driving force of a pipe pressured by the inner gas [Wang and Liu 2007]. However, no useful constitutive model is developed for accurate prediction of the strain limits in the SBD and thus there have been few attempts to clarify the influence of the anisotropy on the buckling resistance and the ductility. Development of a model to represent anisotropic hardening in a line pipe, therefore, is necessary in the SBD.

I.2 Thesis Aims

The aims of this thesis is to better understand anisotropic ductility and toughness in high strength line pipe steel and then to develop a constitutive model representing anisotropic ductility and toughness as well as plastic anisotropy.

In detail the following aims are to be achieved.

- Development of a combined phenomenological model for anisotropic hardening behavior in high strength linepipe steel and its application to pipe bending simulation
- Investigation of prestrain effect on ductility and toughness in X100 high strength steel.
- Experimental and numerical evaluation of anisotropic fracture toughness of the X100 material.
- Development of a damage model incorporated with anisotropic yield function and kinematic hardening model and its application to fracture toughness test simulations for the X100 steel.

I.3 Thesis structure

This thesis contains seven chapters. Following this introduction (Chapter 1), Chapter 2 contains all the experimental methods conducted in this thesis and the used material information. The results of the research work carried out in this thesis are the given in four further chapters, drawing closely on four journal papers. Chapter 3 contains a paper presenting a combined phenomenological model which can represent anisotropic hardening behavior in high strength line pipe steel. Experimental work performed on effect of prestrain on ductility and toughness in a steel plate for the API X100 grade line pipe is given in Chapter 4. Chapter 5 contains a paper on damage model representing anisotropic ductility and toughness in high strength steel. The advanced damage model including kinematic hardening is shown in Chapter 6. Chapter 7 presents the conclusions of this thesis.

Chapter -II-

Material characterisation and experimental procedures

Contents

Résumé en français :

L'objet de ce chapitre est de présenter le matériau d'étude et d'aborder les procédures expérimentales. Les objectifs étant de comprendre les mécanismes de rupture des tôles en X100 et de construire une base de données expérimentales permettant d'identifier les paramètres des modèles et de valider leur efficacité.

Le matériau d'étude est fourni par Nippon Steel Corporation sous forme d'une plaque d'acier de 16 mm de nuance API X100[1]. Il appartient à la classe des aciers dits HSLA (High Strength Low Alloy Steels).L'obtention d'une bonne limite d'élasticité et d'une bonne ténacité résulte d'un processus de réduction des impuretés et d'un traitement thermo-mécanique contrôlé (TMCP) au cours du laminage de la brame obtenue par coulée continue jusqu'à l'obtention de la tôle. Le refroidissement rapide induit par une trempe à l'eau permet d'obtenir une structure ferrito-bainitique

[1] ce qui signifie que la limite minimale garantie dans le plan de laminage est de 100ksi, soit 690 MPa

assez fine : la taille moyenne des grains polygonaux de ferrite étant de 4 μm. La bainite contient des précipités d'austénite-martensite (MA) dont le volume est d'environ 3 $\%$. La forme des inclusions primaires est contrôlée par l'addition de Calcium et de Titane (Ti) pour obtenir de fines inclusions globulaires de sulfure de calcium (CaS) et d'oxydes de titane (TiO) dont la fraction volume reste assez faible (2.10^{-4}).

L'effet de pré-déformation a été étudié au travers de prélèvements de matériau sur de grandes éprouvettes de traction soumises à des niveaux de déformation contrôlée. Des niveaux allant jusqu'à 6 $\%$ de pré-déformation ont été appliqués selon la direction T (Transverse au laminage) correspondant au pré-chargement que peut subir un tube lors de sa mise en forme.

De nombreux essais ont été réalisés sur le tôles non déformées et les matériaux pré-déformées avec 7 types d'éprouvettes. L'éprouvette de traction (ST) est utilisée pour caractériser le comportement élasto-plastique selon les directions L (direction de laminage), T (direction transverse) et D (direction diagonale dans le plan L-T). Les éprouvettes entaillées (NT) sont utilisées pour étudier les propriétés d'endommagement et le comportement pour des états de triaxialité différents. Les éprouvettes PE permettent de caractériser le comportement du matériau en déformation plane. Elles permettent notamment de discriminer le critère de contrainte équivalente qui pour ce type de matériau peut être différent du critère de Von Mises. Les éprouvettes de fissuration CT (Compact Tensile), SENB (Single Edge Notch Bending) et SENT (Single Edge Notch Tensile) permettent de réaliser une propagation stable de la fissure selon différents taux de confinement plastique. Ces essais ont plusieurs objectifs : i) étudier la propagation ductile sur une éprouvette où la triaxialité des contraintes au cœur de l'éprouvette est plus sévère que dans le cas des éprouvettes NT et obtenir une base expérimentale permettant de valider les modèles d'endommagement ductile utilisés. ii) Caractériser l'anisotropie de rupture macroscopique en termes de paramètres de ténacité J_0 et de résistance à la déchirure $\partial J/\partial(\Delta a)$. On notera pour ces essais la nomenclature suivante : i) L-T : L- direction de sollicitation et T- direction de propagation de la fissure, ii) T-L : T- direction de sollicitation et L- direction de propagation de la fissure.

II.1 Material characterisation

A high strength steel plate for a line pipe has been considered in this work, designated API Grade X100. The used material was supplied by Nippon Steel Corporation.

The manufacturing process of the tested steel is shown in Figure II.1. First of all, hot metal was subjected to desiliconization, dephosphorization and desulphurization in the pretreatment of the hot metal. Next, in the LD-converter, the reduction in carbon and nitrogen contents was conducted by decarburization and denitrification treatments. In the vacuum degassing, oxygen content was removed. Alloying elements were added in both the LD-converter and the vacuum degassing processes. After the refining treatments, a slab was made through the continuous casting process. In the casting process, soft reduction technology was applied, in order to reduce center segregation of the cast slab. After reheating, the slab was thermomechanically rolled into a 16mm thick plate, and then subjected to accelerated cooling in the heavy plate mill.

The chemical composition of the tested API Grade X100 steel is shown in Table II.1. C content was reduced to 0.05$\%$ in order to improve low temperature toughness of the plate. Mn, Ni, Cr and Cu were added to the steel to achieve the specified minimum strength of the X100 grade. Ti was included and Al content was kept less than 0.01$\%$ to obtain fine TiO particles, which was efficient to improve toughness of the heat affected zone in a welding joint. Nb was also added into the steel, in order to improve strength and toughness at the same time.

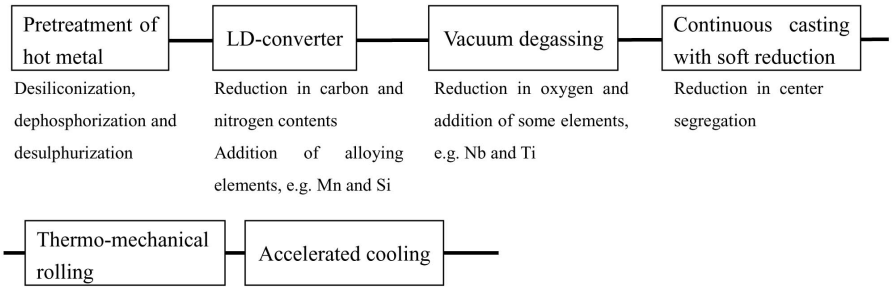

Figure II.1 : Manufacturing process of X100 steel plate

Table II.1 : Chemical composition of the used steel (weight%)

C	Si	Mn	P	S	Ti	N
0.051	0.20	1.95	0.007	0.0015	0.012	0.004

Other alloying elements: Ni, Cr, Cu, Nb.

Figure II.2 shows a pseudo three-dimensional scanning electron microscope (SEM) micrograph of the X100 steel used in this study. Due to heavy rolling condition during the thermomechanical control process, each grain enlarged along the L-direction. A SEM image of the tested steel is shown in Figure II.3. The microstructure was composed of fine polygonal ferrite and bainite structure. In the bainite, martensite-austenite (MA) constituent was precipitated. The volume of M-A constituent is about 3%. The average size of polygonal ferrite was around 4 micron.

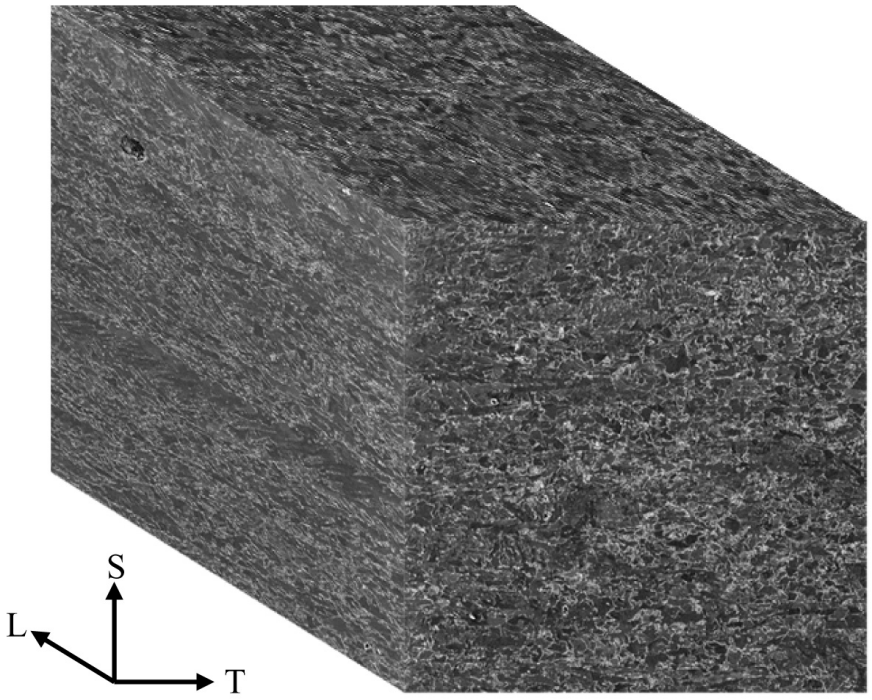

Figure II.2 : Pseudo three-dimensional SEM micrograph in X100 steel.

Figure II.4 shows hardness distribution along through-thickness direction at three positions in

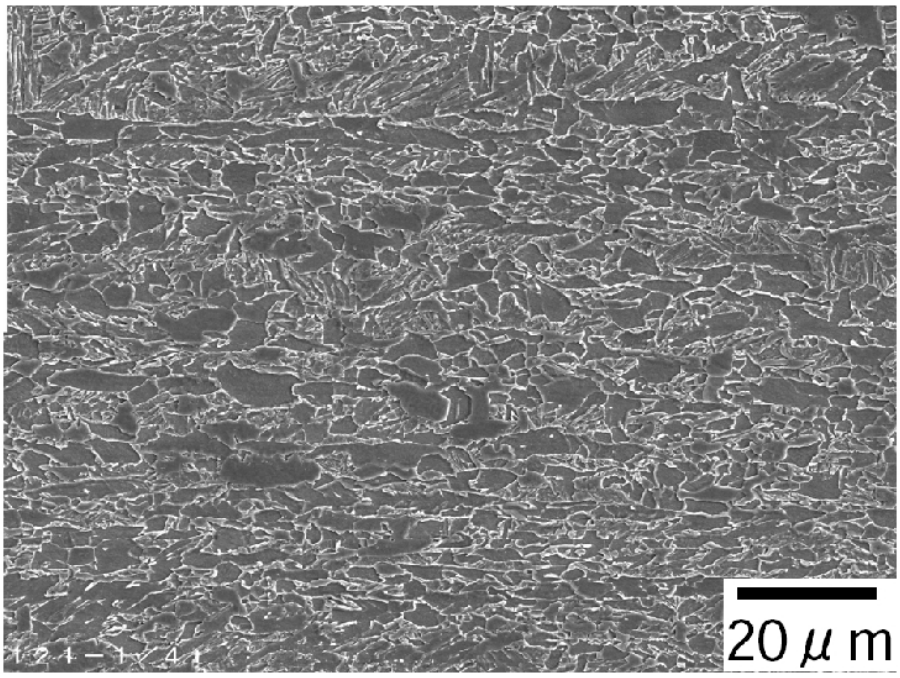

Figure II.3 : SEM image of the tested X100 steel.

the tested steel. Hardness was measured at 1mm intervals from a surface of the plate. The loading force was 98N for the hardness test. The average Vickers hardness was Hv233, from which the ultimate strength of the steel could be estimated approximately at 746MPa. The hardness values were almost uniform through the thickness of the steel plate. No hardening around the surface of the plate appeared, because of optimization of accelerated cooling condition.

Generally speaking, ductile rupture coincides with void nucleation, growth and coalescence. Figure II.5 demonstrates an example SEM photo of fracture surface of X100 steel used in this study. The primary void nucleates at a inclusion. The inclusion are mainly calcium sulfides (CaS) or/and titanium oxides.The image indicates that it is very important to detect the inclusion volume fraction to carry out precise damage simulation later.

Figure II.6 shows a back scattering image on the cross section of the tested steel. On the back scattering image, one can easily distinguish inclusions from base metal. Black particles are inclusions. 100 photographs were taken at different positions on the cross section and then total number and the average diameter of inclusions so that the volume fraction of the inclusions could be estimated. The calculated volume fraction was 2.02×10^{-4}.

Due to the thermomechanical hot rolling process, the tested steel has an anisotropic mechanical properties. This is the reason why it is important to keep track of the material principal axes. In the following the longitudinal direction corresponding to the rolling direction is referred to as L; the transverse direction is referred to as T and the short transverse (thickness) direction is referred to as S. D stands for the diagonal direction on L-T plane formed by the L-direction and T-direction.

II.2 Preparation of prestrained material

In order to prepare prestrained material, an interrupted tensile test has been performed on a 4000 kN tensile machine. A large-scale flat tensile specimen used for the prestrain test is shown in Figure II.7. The specimen was designed to produce a 200mm$\times$100mm zone at the center of the specimen where plastic strain was uniform. prestrain was applied up to 6% along T-direction which corresponds to

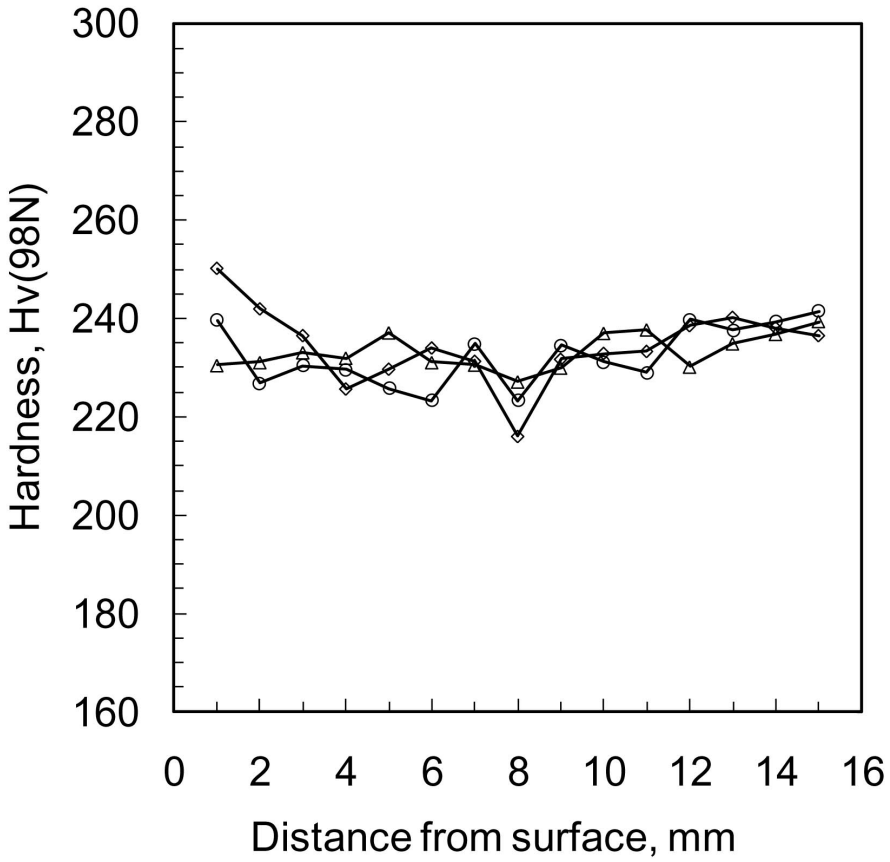

Figure II.4 : Hardness distribution of the used X100 steel.

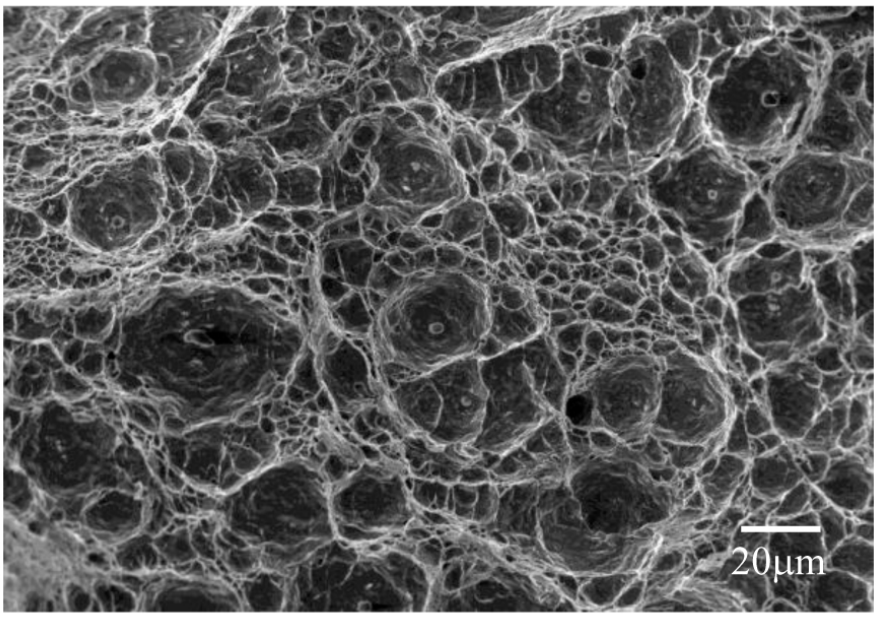

Figure II.5 : Typical ductile fracture surface of X100 steel.

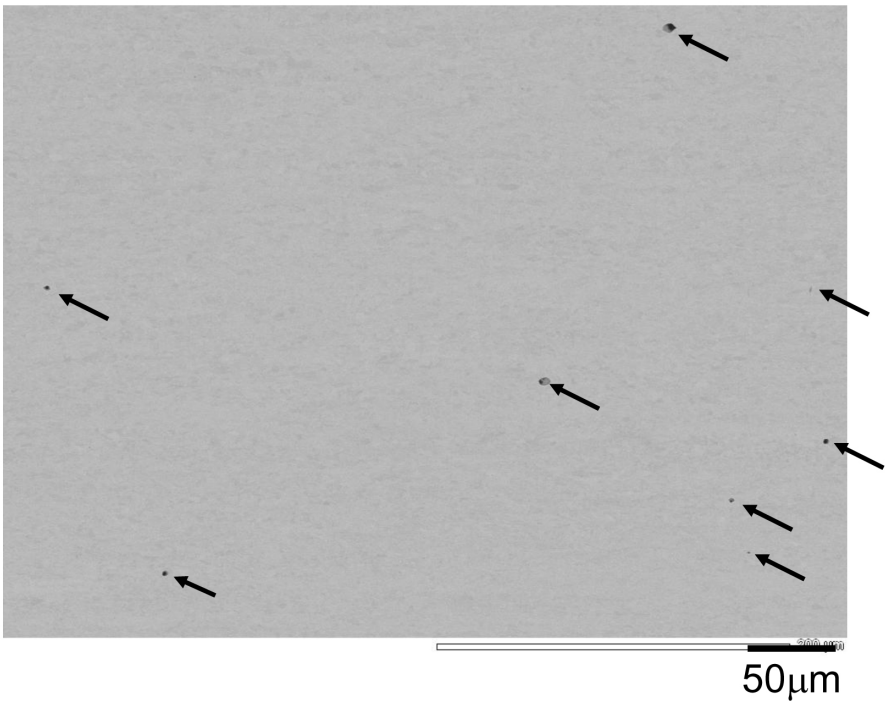

Figure II.6 : Back scattering image of X100 steel.

prestraining direction during pipe forming process. Strain gauges were glued on the test specimen in order to check the applied prestrain level. The displacement rate for all the tests was 13.3mm/min (strain rate approximately of $10^{-4}s^{-1}$).

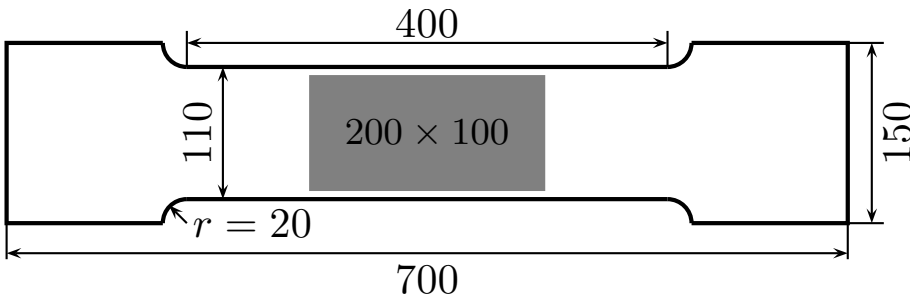

Figure II.7 : Schematic illustration of large tensile specimen for prestraining (dimension in mm). The gray area indicates the zone where prestrain is homogeneous.

II.3 Mechanical testing

In this study, mechanical tests have been performed for X100 plates under as-received and prestrained states. Three types of tensile specimen have been utilized: (a) smooth tensile bars, (b) notched tensile bars, (c) plane deformation tensile sheets. Three types of fracture toughness test specimens have been also used: (a) compact tensile specimen, (b) single-edge-notched bend specimen and (c) single-edge-notched tensile specimen. All tests have been carried out on a servo-hydraulic testing machine.

II.3.1 Smooth bar tensile test

Smooth bar tensile tests were carried out for as-received and prestrained materials, in order to obtain the basic tensile properties. The tensile specimen is shown in Figure II.8. For clarification of anisotropic plasticity, the testing specimen was cut along three different directions (L, T and D directions). Two extensometers were attached to the specimen, in order to measure axial and radial strain of the specimen at the same time, as demonstrated in Figure II.9. The initial length of the longitudinal extensometer (MTS632.11.F.21(2248)) is 9mm. The diametrical extensometer (MTS632.02C.21(1526)) was carefully set up along S-direction because diameter reduction was quite different at each circumferential position due to plastic anisotropy. The test was performed in machine displacement control. The displacement rate was 1mm/min (strain rate of $5.10^{-4}s^{-1}$).

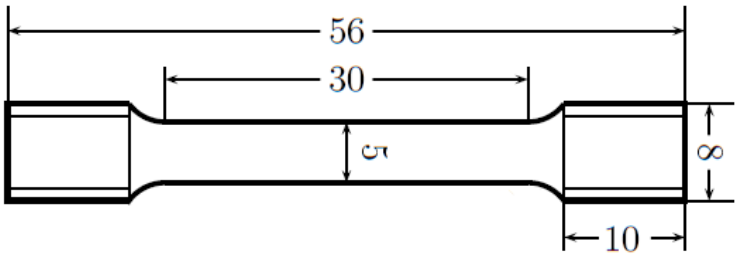

Figure II.8 : Schematic illustration of smooth bar tensile specimen (dimensions in mm).

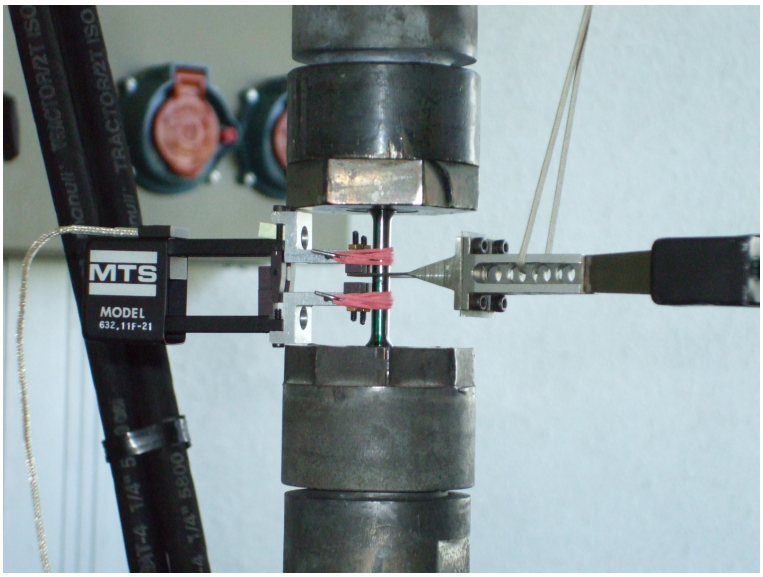

Figure II.9 : Photograph of a mounted smooth bar tensile test sample.

II.3.2 Notched bar tensile test

In order to characterize ductile fracture properties of the tested X100 steel, axisymmetric notched bar tensile tests have been conducted in the L and T directions. The notch shape strongly correlates with the stress triaxiality ratio, which is important to study effect of stress level on ductile fracture mechanism, at the center of the tensile specimen. In this study, three types of notch tensile specimen have been utilized, as illustrated in Figure II.10. Among three specimens, the notch radius was different (0.6mm, 1.2mm and 2.4mm), while the diameter of the minimal section was constant (6mm). Axial and diametrical extensometers were set up on the notch specimen as shown

in Figure II.11. The initial length of the longitudinal extensometer (MTS632.11F.21(2248)) was 8.8mm. The radial extensometer (MTS632.02C.21(1526)) was attached to the minimal section along S-direction. All notched tensile specimens have been tested under the longitudinal strain control; the displacement ratio of NT1, NT2 and NT4 specimen was 0.036mm/min, 0.072mm/min and 0.144mm/min, respectively.

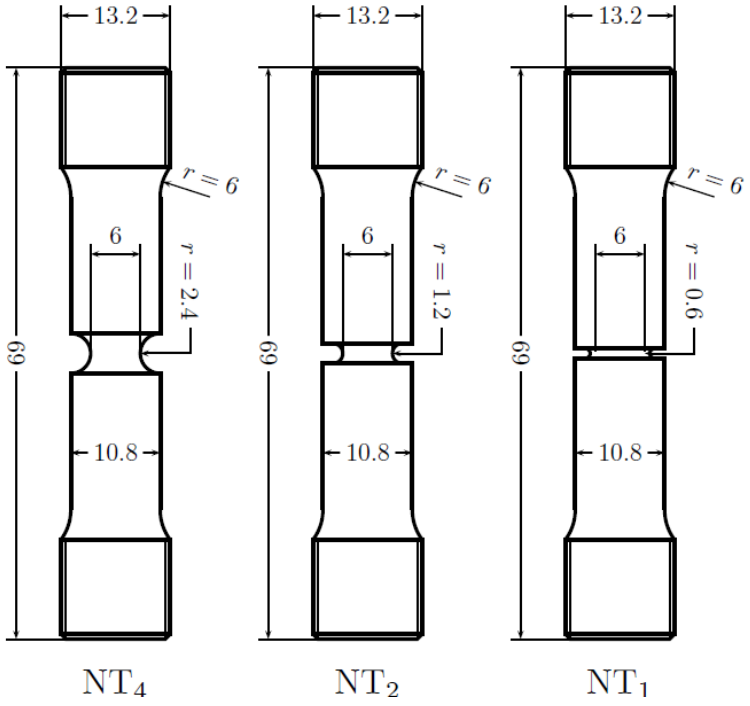

Figure II.10 : Schematic illustration of notched bar tensile specimens (dimensions in mm).

II.3.3 Plane strain tensile test

As shown in Figure II.12, a wide and relatively thin tensile specimen was used to characterize plastic behavior in a plane strain state. The specimen width and thickness was 20mm and 2mm, respectively. The plane deformation test was conducted in the L and T directions with an imposed displacement rate corresponding to a mean strain rate of $5.0 \times 10^{-4}\,\mathrm{s}^{-1}$ at the center of the test specimen. During the test, both axial and thickness strains were measured by two extensometers (MTS632.11F-20 for the axial strain and a homemade for the thickness strain), as illustrated in Figure II.13.

II.3.4 Fracture toughness tests

For determination of ductile tearing resistance of X100 steel in various stress states, three types of fracture toughness test specimens were used in this study. The used specimens were compact tensile (C(T)), single-edged bend (SE(B)) and single-edged tensile (SE(T)). All specimens contained notches that were sharpened by pre-fatigue test. The fracture toughness samples had different crack-tip constraint; the C(T) specimen had highest crack-tip constraint, whereas the SE(T) specimen had lowest one. Each test procedure is described as follows.

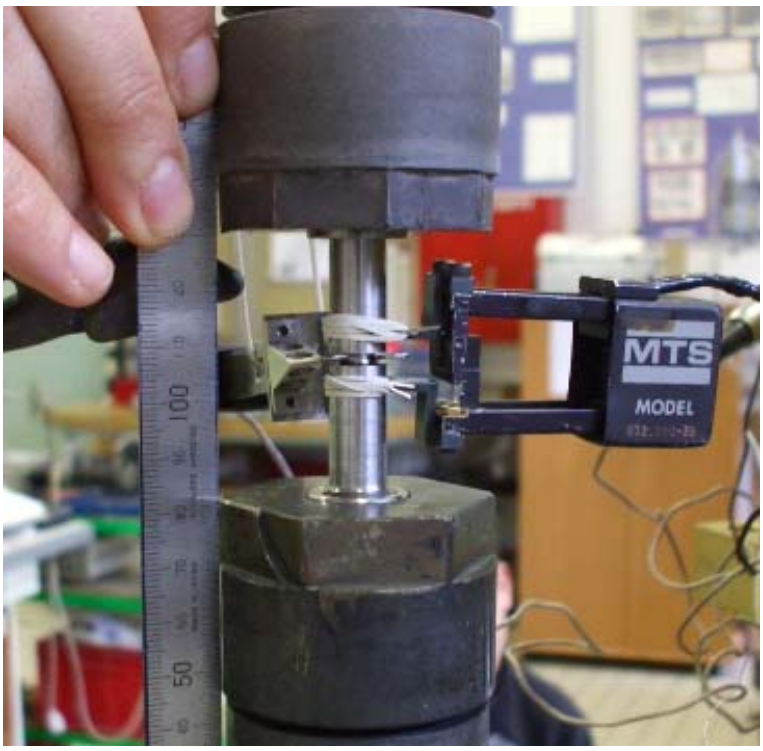

Figure II.11 : Photograph of a mounted notched bar tensile test sample.

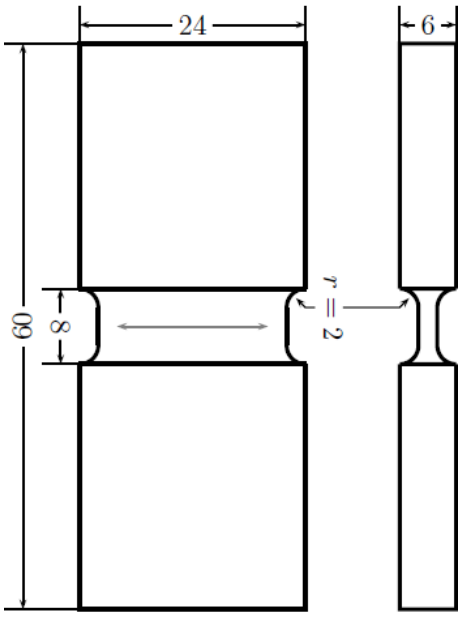

Figure II.12 : Schematic illustration of plane deformation tensile specimen (dimensions in mm).

a) Compact tensile test

The C(T) specimen geometry is shown in Figure II.14. L-T (resp. T-L) configuration was investigated in which L (res. T) corresponds to the loading direction and T (resp. L) to the crack propagation direction. The specimen thickness, B, and width, W, was 12.5 mm and 25.0 mm, respectively. No

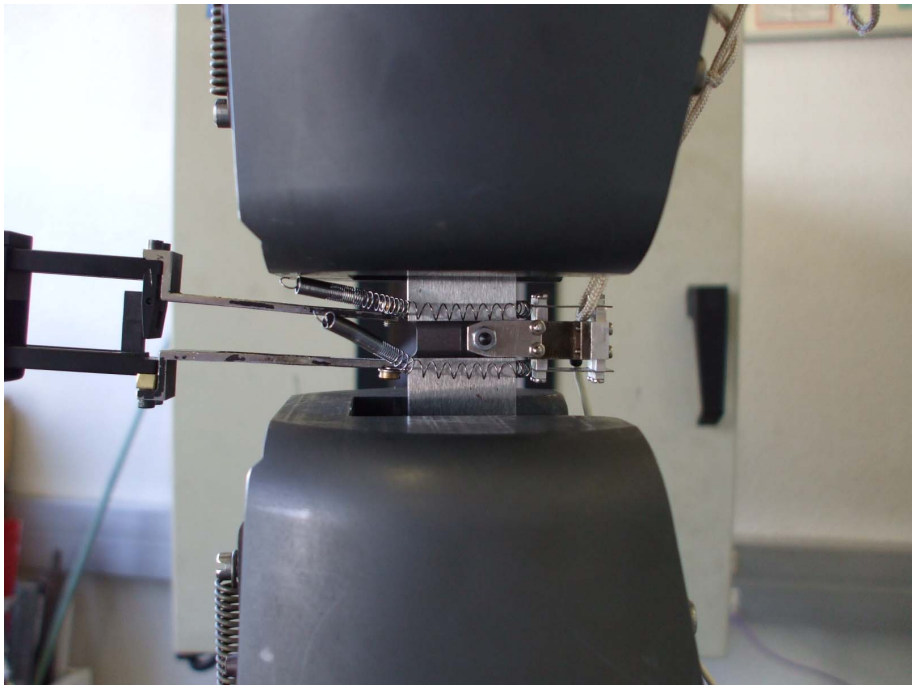

Figure II.13 : Photograph of a mounted plane deformation tensile test sample.

side grooves were machined on the specimen surfaces.

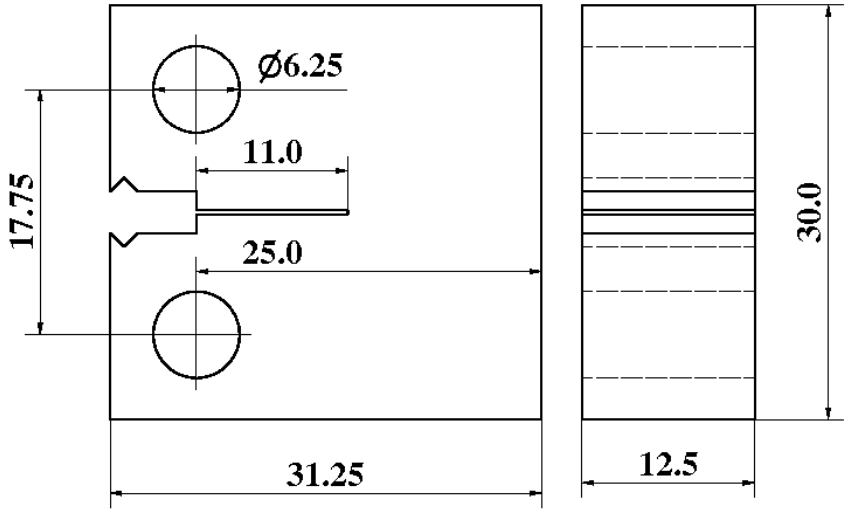

Figure II.14 : Schematic illustration of C(T) test specimen (dimensions in mm).

All specimens with a machine notch of 11.0 mm were pre-cracked in fatigue so that a total initial crack length of all specimens could be between $0.56W$ and $0.62W$. The fatigue force was controlled with less than 3.6 kN, monitoring the fatigue crack extension on both sides of the specimen. The force ratio was 0.1 and the fatigue frequency was 40 Hz.

The J-Δa resistance curve was determined using multi-specimen technique in accordance with ASTM-1820 [ASTM 2006] for as received and prestrained (2, 4 and 6 $\%$) X100 steels. The fracture toughness test was conducted under displacement control at ambient temperature. The displacement rate was 1 mm/min. Force and displacement were simultaneously recorded during the test, in order

to evaluate J. The ductile crack extention, Δa, was directly determined on a fracture surface of the tested specimen which was broken at liquid nitrogen temperature after unloading.

b) Single-edge-notched bend test

The SE(B) specimen geometry is shown in Figure II.15. Both L-T and T-L configurations were investigated for as-received and 6 $\%$ prestrained X100 steels. The specimen thickness, B, and width, W, was 10.0 mm and 20.0 mm, respectively. No side grooves were machined on the specimen surfaces.

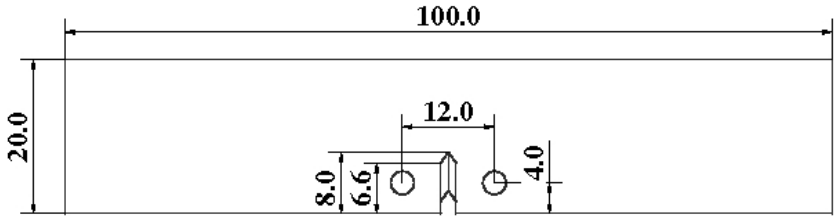

Figure II.15 : Schematic illustration of SE(B) test specimen (dimensions in mm).

All specimens with a chevron notch of 8.0 mm were pre-cracked in fatigue so that a total initial crack length of all specimens could be between $0.48W$ and $0.50W$. The fatigue force was controlled with less than 2.9 kN, monitoring the fatigue crack extension on both sides of the specimen. The force ratio was 0.1 and the fatigue frequency was 40 Hz.

The J-Δa resistance curve was determined using multi-specimen technique in accordance with ASTM-1820. The fracture toughness test was conducted under displacement control at ambient temperature. The displacement rate was 1 mm/min. Force and crack mouth opening displacement (CMOD) were simultaneously recorded during the test, in order to evaluate J. The ductile crack extension, Δa, was directly determined on a fracture surface of the tested specimen which was broken at liquid nitrogen temperature after unloading.

c) Single-edge-notched tension test

The SE(T) specimen geometry is illustrated in Figure II.16. Both L-T and T-L configurations were investigated for as-received X100 steel. The specimen thickness, B, and width, W, was 12.5 mm and 25.0 mm, respectively. No side grooves were machined on the specimen surfaces.

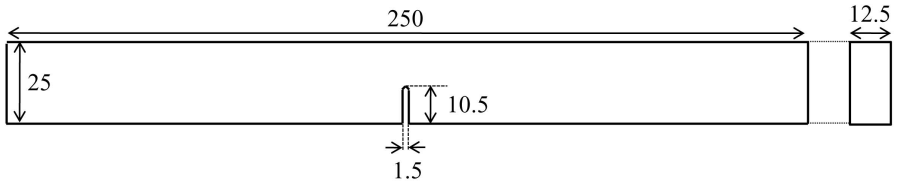

Figure II.16 : Schematic illustration of SE(T) test specimen (dimensions in mm).

All specimens with a machined notch of 10.5 mm were pre-cracked in fatigue so that a total initial crack length of all specimens could be between $0.52W$ and $0.54W$. The fatigue force was controlled with less than 5.0 kN, monitoring of the fatigue crack extension on both sides of the specimen. The force ratio was 0.1 and the fatigue frequency was 40 Hz.

The J-Δa resistance curve was determined using multi-specimen technique in accordance with DNV-RP-F108. The fracture toughness test was conducted under displacement control with clamped

end conditions at ambient temperature. The distance between the grips was 250 mm and the displacement rate was 1.0 mm/min. Force and CMOD were simultaneously recorded during the test, in order to evaluate J. The ductile crack extension, Δa, was directly determined on a fracture surface of the tested specimen which was broken at liquid nitrogen temperature after unloading.

d) Calculation of J integral value

J is divided in elastic and plastic components as follows:

$$J = J_{el} + J_{pl} \tag{II.1}$$

where J_{el} and J_{pl} is elastic and plastic component, respectivly. The elastic J_{el} is defined as:

$$J_{el} = \frac{K^2(1-\nu^2)}{E} \tag{II.2}$$

K is inferred through the following equation at the final load.

$$K = \frac{P}{BW^{1/2}} f(a/W) \tag{II.3}$$

For a CT specimen,

$$f(a/W) = \frac{[(2+\frac{a}{W})(0.886+4.64(\frac{a}{W})-13.32(\frac{a}{W})^2+14.72(\frac{a}{W})^3-5.6(\frac{a}{W})^4]}{(1-\frac{a}{W})^{3/2}} \tag{II.4}$$

and a SENB specimen,

$$f(a/W) = \frac{3(\frac{a}{W})^{1/2}[1.99-(\frac{a}{W})(1-\frac{a}{W})(2.15-3.93(\frac{a}{W})+2.7(\frac{a}{W})^2)]}{2(1+2\frac{a}{W})(1-\frac{a}{W})^{3/2}} \tag{II.5}$$

and a clamped SENT specimen,

$$f(a/W) = \frac{2\tan(\frac{\pi a}{2W})}{\cos(\frac{\pi a}{2W})}[0.752+2.02(\frac{a}{W})+0.37(1-\sin(\frac{\pi a}{2W}))] \tag{II.6}$$

where a is the physical crack advance length and W is the specimen width. The plasitc J is estimated from the plastic area under the loda-displacemnet curve.

The plastic part of J is expressed as:

$$J_{pl} = \frac{\eta A_p}{B(W-a)} \tag{II.7}$$

where A_p is the plastic area under the load-displacement curve and B is the specimen thickness. η is a dimensionless parameter which depends on both the specimen type and on the geometry.

For a CT specimen,

$$\eta = 2 + 0.522\frac{(W-a_0)}{W} \tag{II.8}$$

and a SENB specimen,

$$\eta = 3.785 - 3.101\left(\frac{a_0}{W}\right) + 2.018\left(\frac{a_0}{W}\right)^2 \tag{II.9}$$

according to ASTM-1820.

In the case of clamped SENT specimens several formulas exist in the literature but a well accepted standard is still missing. The following formula is proposed by DET NORSK VERITAS [DNV 2006]:

$$\begin{aligned}\eta &= 0.85\Bigg\{\left(196.719\exp(-\left(\frac{W-a_0}{W}\right)-64.642\right)\left(\frac{a_0}{W}\right)^5 \\ &+\left(-493.511\exp\left(-\frac{W-a_0}{W}\right)+138.837\right)\left(\frac{a_0}{W}\right)^4 \\ &+\left(463.503\exp\left(-\frac{W-a_0}{W}\right)-106.207\right)\left(\frac{a_0}{W}\right)^3 \\ &+\left(-201.862\exp\left(-\frac{W-a_0}{W}\right)+34.532\right)\left(\frac{a_0}{W}\right)^2 \\ &+\left(39.413\exp\left(-\frac{W-a_0}{W}\right)-4.525\right)\left(\frac{a_0}{W}\right) \\ &+\left(-2.064\exp(\left(-\frac{W-a_0}{W}\right)+1.039\right)\Bigg\}\end{aligned} \tag{II.10}$$

where a_0 is the crack length. The following formula was also proposed by Cravero and Ruggieri [2007]

$$\eta = 1.0398 - 0.687(W-a_0)/W \tag{II.11}$$

This simple formula will be used in this work.

Chapter -III-

Model for the representation of anisotropic hardening behavior

Contents

Résumé en français :

Le chapitre 3 est un article de journal publié dans European Journal of Mechanics — A/Solids [Shinohara et al. 2010].

Cet article présente d'abord les résultats expérimentaux (tractions lisses ST, tractions entaillées NT et déformations planes PE) permettant de caractériser le comportement élasto-plastique du

matériau selon les directions L (direction de laminage), T (direction transverse) et D (direction diagonale dans le plan LT). Les essais de traction (courbes contrainte-déformation et ratio des déformations non axiales) montrent un comportement anisotrope les directions L et T de la tôle. Les essais sur éprouvettes pré-déformées mettent en évidence un écrouissage mixte isotrope et cinématique. Un modèle phénoménologique anisotrope combinant les écrouissages isotrope et cinématique qui permet de rendre compte du comportement plastique de cet acier est alors présenté. Le modèle est identifié sur la base des résultats expérimentaux en utilisant la méthode d'identification développée dans [Bron et Besson 2004]. Les nombreux essais utilisés pour l'identification sont bien représentés tant au niveau contrainte que déformation anisotrope. Le modèle est validé sur des essais non utilisés pour cette identification. Les surfaces de plasticité représentées se distinguent nettement des surfaces de von Mises. La comparaison des surfaces initiales et après pré-déformation illustre un écrouissage cinématique important. Une application du modèle est alors réalisée pour déterminer la charge limite de flexion (moment de flexion maximum) d'une structure tubulaire en présence d'un défaut. Les simulations numériques montrent un effet négatif de la pré-déformation sur le flambement du tube en présence de défaut : augmentation de la charge limite alors que l'angle conduisant au flambement diminue nettement.

Foreword

This chapter was published as a journal paper in European Journal of Mechanics — A/Solids [Shinohara et al. 2010]. The elastoplastic behaviour of high strength line pipe steels including plastic anisotropy and kinematic hardening is presented here.

Abstract

Line pipes have anisotropic mechanical properties, such as tensile strength, ductility and toughness. These properties depend on both prestrain during the cold forming process and on the anisotropy of the mother plates. In this study, a phenomenological model combining isotropic and kinematic hardening is developed to represent anisotropic hardening behavior of high strength steel line pipes. The model is adjusted on experiments carried out on smooth and notched axisymmetric bars and plane strain specimens. The model is used to simulate bending tests carried out on large pipes containing a geometric imperfection. Numerical results suggest that prestraining in pipe forming process significantly affects the bending capacity of pipes.

III.1 Introduction

As consumption of energy is increasing worldwide, the demand for development of natural resources such as oil and gas in remote locations becomes strong. These development areas are often far from the major consumers because the potential locations are harsh environments where ground movement may occur due to loading by offshore ice, discontinuous permafrost or seismic activity. Ground movement will impose some strain demand on the pipelines (see e.g. [Lee et al. 2009]). For these reasons, strain-based design (SBD) is essential in the case of these types of harsh environments, while stress-based design of a pipeline is normally preferred. To achieve a safe and reliable pipeline operation in a harsh area, accurate prediction of the plastic strain imposed by the ground movement are required.

A pipe installed in such a field is subjected to plastic bending deformation. In SBD, the designers need to consider the imposed strain on both tensile and compressive sides of the bended pipe. Normally, full size pipe bending tests are carried out to evaluate the strain limit for buckling on compressive point, while curved wide plate tests are performed to predict the strain limit for ductile

failure on the tension side [Fairchild et al. 2008]. Numerical simulations by finite element analysis are also conducted for specifying the effective mechanical properties of the tested pipes and checking the predicted values against the experimental results [Tsuru et al. 2008].

The detailed mechanical properties of a line pipe have been clarified in the previous works [Tsuru et al. 2008, Shinohara et al. 2008]. The line pipe has anisotropic hardening; a stress-strain curve is quite different between the longitudinal direction and the circumferential direction. These characteristics are mainly due to plastic strain developed during pipe forming. Furthermore, sharp texture of the mother plate, which is generated during thermomechanical control process (TMCP) at the plate mill, encourages anisotropy, especially in high strength line pipes (above X80 grade). Recently, it was pointed out that a buckling strain limit of the bended pipe is significantly affected by the anisotropic properties [Tsuru et al. 2008]. It was also reported that anisotropic hardening has an influence on ductile crack driving force of a pipe pressured by the inner gas [Wang and Liu 2007, Baek et al. 2010]. However SBD of pipelines and in particular plastic instability of pipes have been investigated using rather simple models (i.e. von Mises or Hill plasticity with pure isotropic hardening) which could lead to poor predictions. Development of a model to represent anisotropic hardening and prestrain effect in a line pipe is therefore needed for SBD.

To simulate plastic behavior of the material after prestraining, it is necessary to combine isotropic and kinematic hardening together with plastic anisotropy. Several modeling strategies can be used. The first one, which will be used in this work, is based on phenomenological models which allow for a relatively simple identification of material parameters. As they use few material state variables, they can be used to perform large-scale computations. Mixed nonlinear isotropic and kinematic hardening can be represented following the approach proposed by [Chaboche 1986]. The model has been applied to aluminium alloys under cyclic loading [Hopperstad et al. 1995a;b]. Other authors employed such a model to represent transient hardening of prestrained dual phase steels [Tarigopula et al. 2008; 2009]. In these cases an isotropic stress measure was used to define the yield function. von Mises stress measure is often used but the measure proposed in [Logan and Hosford 1980] can also be used as in [Tarigopula et al. 2008]. However, high strength pipeline steels have a strong anisotropic plasticity [Tanguy et al. 2008, Rivalin et al. 2000b], so that an anisotropic yield function should be used. In [Chaboche 2008] it was proposed to use Hill quadratic function [Hill 1950] together with mixed isotropic/kinematic hardening. However it is known that this function can hardly represent actual experimental data so that more complex yield function have been proposed in the literature [Barlat et al. 1991, Kim et al. 2007, Bron and Besson 2004, Karafillis and Boyce 1993]. However these complex yield surfaces have only been used assuming pure isotropic hardening. The second strategy is based on micromechanical polycrystalline models which use a physically based description of plastic slip in each grain and rules to describe the intergranular interaction [Zouhal et al. 1996, Hoc and Forest 2001, Sai et al. 2006]. Using the experimentally measured texture can help reducing the number of material parameters which need to be fitted. However parameters must be introduced to represent hardening of slip systems, interaction between slip systems and interaction between grains. In addition they use a large number of state variables thus significantly increasing the computation cost so that simulating structures becomes difficult. A third strategy is based on relatively simple macroscopic description but uses physically based state variables such as dislocation densities (see the original work by [Mecking and Kocks 1981]). Following this methodology, some authors [Haddadi et al. 2006] achieved accurate representations of the Bauschinger effect and transient hardening phenomena by prestraining, using a microstructural models proposed in [Teodosiu and Hu 1995].

In this work, experiments are carried out on a API X100 grade line pipe steel plate in the as received state and for several levels of plastic prestrain. Experiments are carried out on smooth and notched axisymmetric bars and plane strain specimens along various loading directions to study both anisotropy and the effect of prestrain. A set of constitutive equations incorporating plastic anisotropy and mixed isotropic/kinematic hardening is proposed to represent the behavior of the material. The

model is adjusted on the experimental data base and used to carry out simulation of large scale pipe bending experiments.

III.2 Material and experimental procedure

III.2.1 Material

The material used in this study is a high-strength steel plate with 16mm thickness for line pipes produced in a commercial heavy plate mill. The chemical composition is shown in Tab. III.1. The plate was made through TMCP and accelerated cooling process in the mill. The microstructure is dual phase consisting of fine polygonal ferrite and bainite structure (see Fig. III.1).

Table III.1 : Chemical composition of the used steel (weight%)

C	Si	Mn	P	S	Ti	N
0.051	0.20	1.95	0.007	0.0015	0.012	0.004

Other alloying elements: Ni, Cr, Cu, Nb.

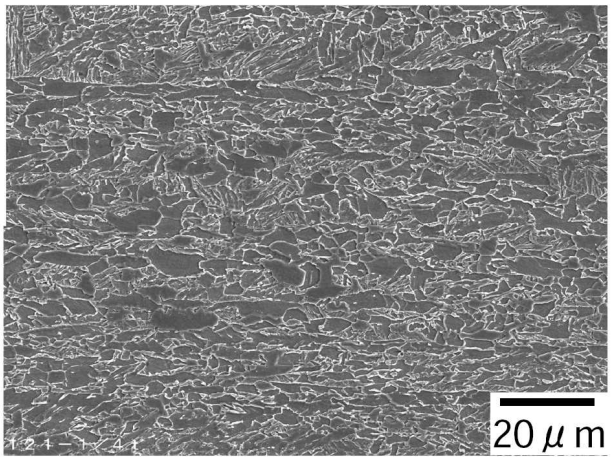

Figure III.1 : SEM image of the steel plate used in this study (Nital etching).

The steel has anisotropic mechanical properties due to development of the crystallographic texture by TMCP, hence it is important to keep track of the material principal axes. In the following, the longitudinal direction, which is corresponding to the rolling direction, is referred to as L; the transverse direction is referred to as T and the short transverse (thickness) direction is referred to as S. D stands for the diagonal direction (45° between directions L and T in the sheet plane). The steel strength after UOE forming [1] meets the API X100 grade specification where the yield strength is required 100 kpsi (or 690MPa) and higher.

[1] UOE forming is a manufacturing process where the plate material is first deformed into an U-shape then an O-shape. The pipe seam is then welded. The pipe is finally Expanded using an internal mandrel. To achieve low ovality, the pipe is typically expanded by 0.8–1.3% from its diameter after the O-step [Herynk et al. 2007].

III.2.2 Experimental procedure

To obtain prestrained materials, prestrain tests were first conducted, using a 4000 kN tensile testing machine. Large flat tensile specimens (see Fig. III.2) were machined so that a 200mm$\times$100mm zone, where applied strain is uniform, could be produced at the center of the specimen. Strain gages were glued on the surface of tested specimens to check the actual prestrain level. The level of prestraining is up to 6.6%. Prestrain was performed along the T direction which corresponds to the main deformation direction during UOE forming.

A comprehensive characterisation of the mechanical properties of the steel was conducted along three different directions (L, T and D) using several types of tensile test specimens. The used geometries are presented in Fig. III.3. All tests were performed at room temperature on a servo-hydraulic testing machine for the as-received and prestrained materials. Test specimens include smooth tensile bars (ST), axisymmetric notched bars with various notch radii (NT$_\chi$) and plane strain specimens (PE). Notched bars, which are often used to characterize rupture (see e.g. [Mackenzie et al. 1977]), are employed here as they allow to induce stresses in directions perpendicular to the main loading direction (in particular along the S direction) and consequently allow to test multi-axial stress states using a simple experimental setup. In addition notched bars allow to reach high levels of deformation so that the hardening behaviour is determined over a wide range for plastic strain. This is an alternative to the sole use of tensile bars which then need to be analysed beyond necking to reach high deformation levels [Mirone 2004, Zhang et al. 1999].

In the case of ST specimens, strain was measured using an extensometer with a gauge length equal to $L_0 = 9$ mm. ΔL denotes the gauge length variation. The imposed strain rate was: $\Delta\dot{L}/L_0 = 5.\,10^{-4}$ s^{-1}. In the case of ST and NT$_\chi$ specimens the diameter reduction ($\Delta\Phi_{\mathrm{S}}$) in the minimum cross section was measured along the S direction along which deformation is maximum. For PE specimens, thickness reduction (Δe) was measured at the center of the specimen. For both NT$_\chi$ and PE specimens the machine cross-head speed was selected so as to obtain a measured strain rate approximately equal to $5.\,10^{-4}$ s^{-1}. In the following F denotes the force, S_0 the initial specimen minimum cross section, Φ_0 the initial specimen minimum diameter and e_0 the initial PE specimen thickness.

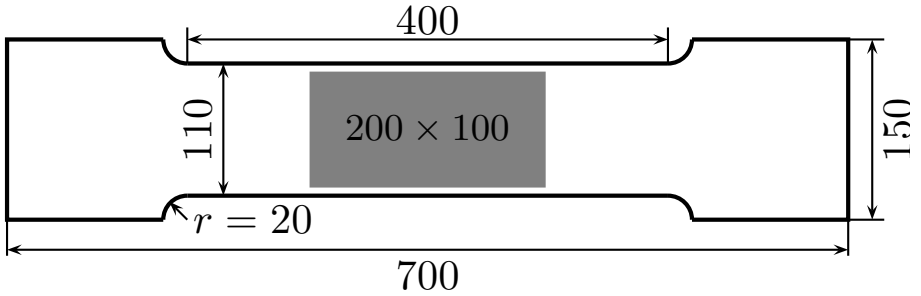

Figure III.2 : Large tensile specimen for prestraining (dimension in mm). The gray area indicates the zone where prestrain is homogeneous.

III.3 Experimental results

III.3.1 Smooth tensile bars

Fig. III.4(a) shows nominal stress (F/S_0) vs nominal strain ($\Delta L/L_0$) curves in different loading directions of smooth tensile bar tests in the as received state. Flow stress depends on the loading direction. The flow stress in T load direction is the highest, while the one in D direction is the

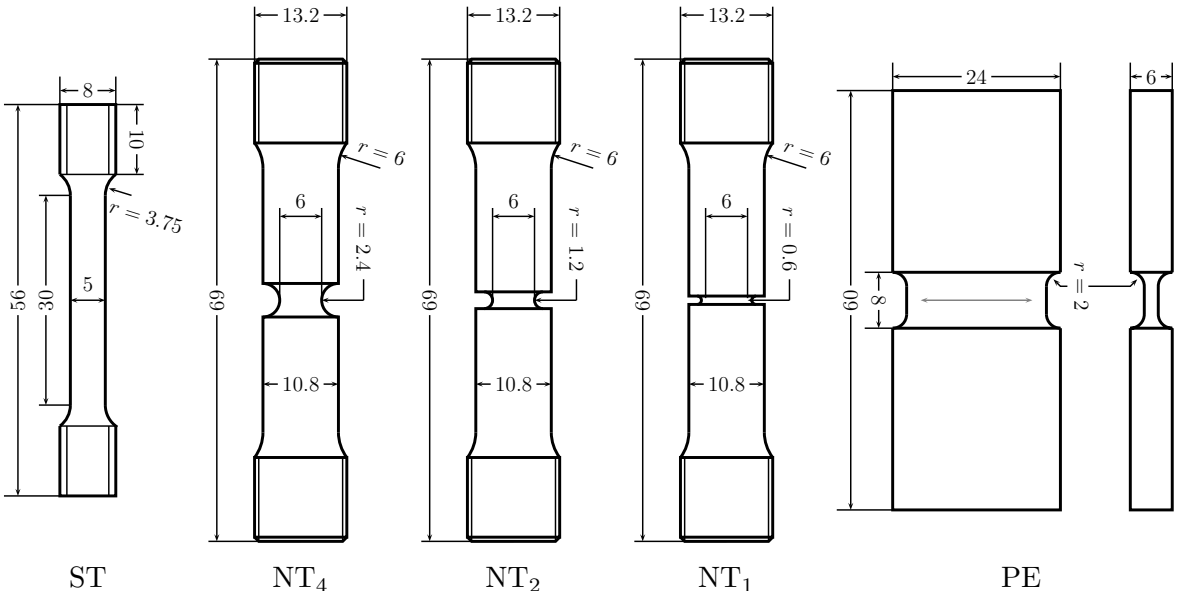

Figure III.3 : Test specimens: ST: smooth tensile bar, $NT_{\chi=1,\,2,\,4}$: axisymmetric notched bars, PE: plane strain specimens (the gray line indicates the plane strain direction).

lowest. Plastic flow behavior also depends on the loading direction as shown in Fig. III.4(b) where the diameter reduction $\Delta\Phi_S/\Phi_0$ is plotted as a function of the elongation $\Delta L/L_0$. In L and T loading, plastic anisotropy is obvious. Deformation along the S direction is larger than in the isotropic case so that initially round cross sections deform into ellipses (see e.g. [Tanguy et al. 2008]). On the other hand, D loading leads to an "isotropic" diameter reduction.

True stress-true strain curves of the smooth bar test for prestrained materials are shown in Fig. III.5. True stress-true strain curves are computed assuming volume conservation. The method is applied up to the ultimate tensile test (UTS). Stress-strain curves of the prestrained materials are shifted by the amount of prestrain. In T direction, which corresponds to the prestraining direction, tensile tests on prestrained materials corresponds to elastic reloading up to the flow curve of the as-received material with a sharp transition between elastic and plastic regimes. Beyond yielding, curves coincide with that of the as-received material. On the other hand, in L direction (orthogonal one to the prestraining) and D direction (the 45° direction from T), the yield stress is higher than that of the as-received material but work hardening is rate continuously changing at the early strain stages with a smooth transition between elastic and plastic regimes. This behaviour is characteristic of mixed isotropic/kinematic hardening evidenced by performing strain-path changes [Tarigopula et al. 2009].

III.3.2 Notched bars

Fig. III.6 shows the normalized load (F/S_0) as a function of diameter reduction ($\Delta\Phi_S/\Phi_0$) for the various notched bars and for all prestrain levels. For a given testing condition (i.e. loading direction and prestrain level), maximum load increases with notch severity [Bridgman 1952, Mackenzie et al. 1977] and ductility (characterized by the sharp load drop point) is reduced [Devillers-Guerville et al. 1997] as could be expected. A transient hardening (i.e. smooth transition between elastic and plastic regimes) behaviour is obtained for all cases. The transient hardening behaviour is still present for T loading on prestrained materials due to the development of a deformation gradient inside the notch (geometrical effect). With increasing prestrain level, maximum load increases and the radial strain at which the maximum load is reached decreases. For a given sample geometry and a given prestrain

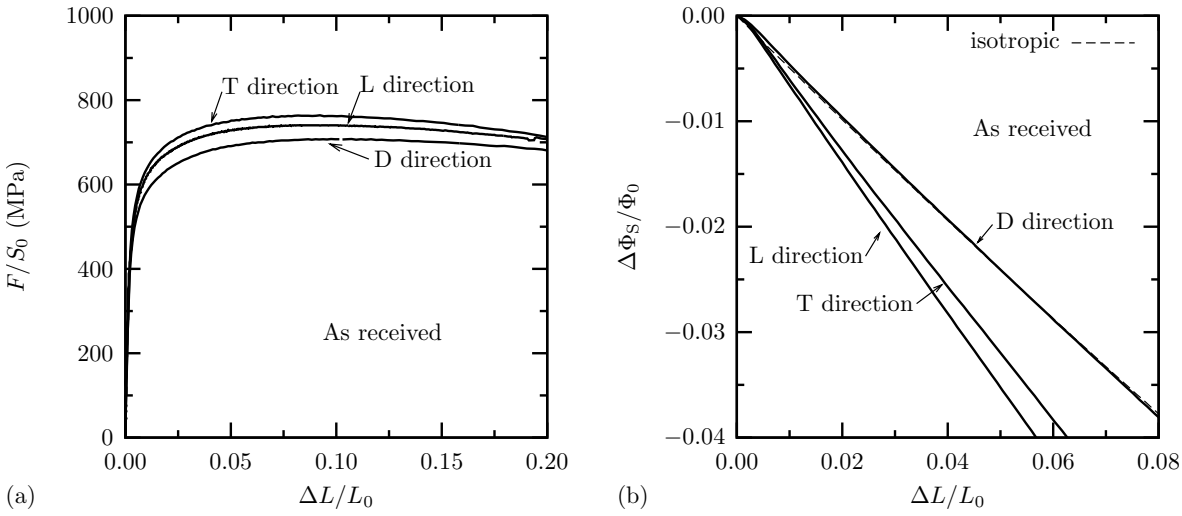

Figure III.4 : (a) Nominal stress-strain curves in smooth bar tests of as-received steel. (b) Diameter reduction along the S direction as a function of elongation for L,T and D loading directions. The isotropic case corresponds to the equation: $\Delta\Phi_S/\Phi_0 = (1 + \Delta L/L_0)^{-\frac{1}{2}} - 1$.

level, the maximum load is higher for T-loading due to both prestrain and the higher yield limit in the T-direction.

III.3.3 Plane strain specimens

Nominal stress-strain curves of plain strain tests for the as-received and 6% prestrained materials are shown in Fig. III.7. In the as-received state, flow stress in T load direction is larger than that in L. Especially, yield strength is much larger in T loading than in L. After 6% prestraining, work hardening is almost lost in both directions and the flow stress in T is still higher than in L.

III.3.4 Strain rate sensitivity

The material strain rate sensitivity was tested using three different strain rate : 5.10^{-5}, 5.10^{-4} and 5.10^{-3} s^{-1}. Results are shown on Fig. III.8 for the as received material loaded along the L direction. A slight strain rate dependence is observed with stresses increasing with increasing strain rate.

III.4 Constitutive model

III.4.1 Constitutive equations

The steel used in this study presents both anisotropic plasticity and kinematic hardening. The model proposed in the following accounts for both phenomena. In order to represent kinematic hardening, a back stress $\underline{X}$ is introduced [Chaboche 1989]. The yield surface is expressed using the difference ($\underline{B}$) between the Cauchy stress $\underline{\sigma}$ and the back stress: $\underline{B} = \underline{\sigma} - \underline{X}$. In order to account the anisotropic plasticity it is necessary to use an anisotropic stress measure to define the yield surface. The model proposed in [Bron and Besson 2004] is used in the following. It consists in a generalization of of previously published models [Karafillis and Boyce 1993, Barlat et al. 1991]. For any symmetric

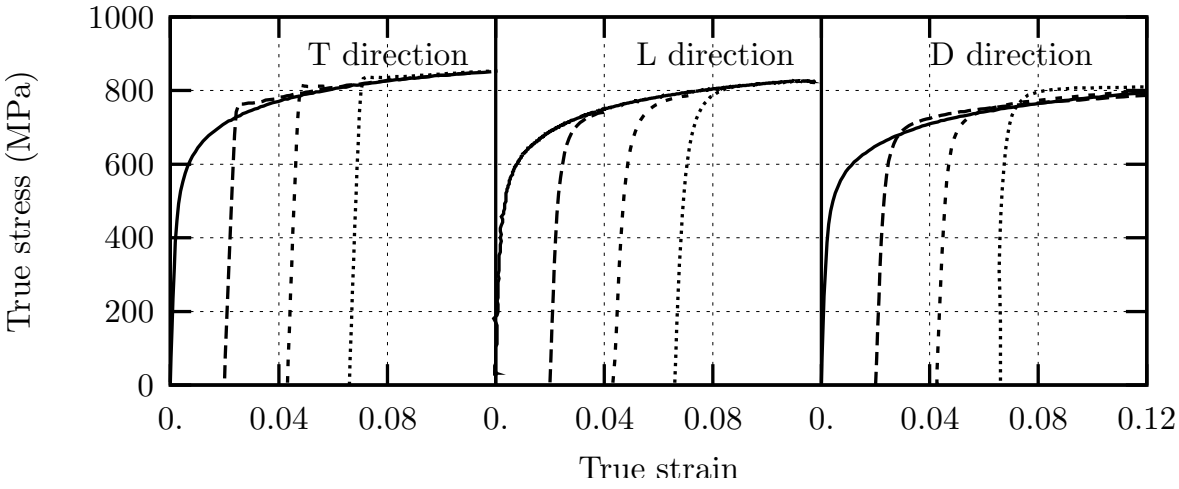

Figure III.5 : True stress-strain curves in smooth bar tests of as-received and prestrain steels.

second order tensor $\underline{T}$, the anisotropic scalar measure (T_E) is defined as:

$$\underline{T} \;\rightarrow\; T_E = \left(\sum_{k=1}^{N} \alpha_k T_{Ek}^a \right)^{1/a} \tag{III.1}$$

with $\sum_k \alpha_k = 1$ and $\alpha_k \geq 0, \forall k$. a is a model coefficient. The function $T_E(\underline{T})$ is positive and homogeneous of degree 1. T_{Ek} are secondary anisotropic scalar measures. In the following, two measures will be used ($N = 2$) as in [Bron and Besson 2004, Tanguy et al. 2008]. One first defines two modified deviators:

$$\underline{T}_k = \underline{\underline{L}}_k : \underline{T} \qquad k = 1, 2 \tag{III.2}$$

where the fourth order tensor $\underline{\underline{L}}_k$ is expressed as using Voigt notations:

$$\underline{\underline{L}}_k = \begin{pmatrix} \frac{1}{3}(c^k_{\mathrm{LL}} + c^k_{\mathrm{SS}}) & -\frac{1}{3}c^k_{\mathrm{SS}} & -\frac{1}{3}c^k_{\mathrm{LL}} & 0 & 0 & 0 \\ -\frac{1}{3}c^k_{\mathrm{SS}} & \frac{1}{3}(c^k_{\mathrm{SS}} + c^k_{\mathrm{TT}}) & -\frac{1}{3}c^k_{\mathrm{TT}} & 0 & 0 & 0 \\ -\frac{1}{3}c^k_{\mathrm{LL}} & -\frac{1}{3}c^k_{\mathrm{TT}} & \frac{1}{3}(c^k_{\mathrm{TT}} + c^k_{\mathrm{LL}}) & 0 & 0 & 0 \\ 0 & 0 & 0 & c^k_{\mathrm{TL}} & 0 & 0 \\ 0 & 0 & 0 & 0 & c^k_{\mathrm{LS}} & 0 \\ 0 & 0 & 0 & 0 & 0 & c^k_{\mathrm{ST}} \end{pmatrix} \tag{III.3}$$

$c^{1,2}_{\mathrm{TT...ST}}$ are model coefficients. The eigenvalues of $\underline{T}_k$ are then computed: $T^1_k \geq T^2_k \geq T^3_k$. T_{E1} is then computed as:

$$T_{E1} = \left(\frac{1}{2} \left(|T^2_1 - T^3_1|^{b_1} + |T^3_1 - T^1_1|^{b_1} + |T^1_1 - T^2_1|^{b_1} \right) \right)^{1/b_1} \tag{III.4}$$

and T_{E2} as:

$$T_{E2} = \left(\frac{3^{b_2}}{2^{b_2} + 2} \left(|T^1_2|^{b_2} + |T^2_2|^{b_2} + |T^3_2|^{b_2} \right) \right)^{1/b_2} \tag{III.5}$$

These definitions introduce two other model coefficients: b_1 and b_2.

The yield surface is then expressed using the above definition of the anisotropic stress measure as:

$$\phi = B_E - R(p) \tag{III.6}$$

where $R(p)$ represents isotropic hardening. Plastic flow is then computed using the normality rule as:

$$\underline{\dot{\varepsilon}_p} = \dot{p}\frac{\partial \phi}{\partial \underline{\sigma}} = \dot{p}\frac{\partial B_E}{\partial \underline{\sigma}} \tag{III.7}$$

where $\dot{p}$ is the plastic multiplier such that $\underline{\dot{\varepsilon}_p} : \underline{B} = \dot{p}B_E$. The evolution of the back stress is written using recall term to obtain non-linear (Armstrong–Frederick type) kinematic hardening [Chaboche 2008]:

$$\underline{\dot{X}} = \frac{2}{3}C\underline{\dot{\varepsilon}_p} - \dot{p}D\underline{X} \tag{III.8}$$

C and D are material parameters. In this study, only one back stress was used. The model can easily be extended to allow for a superposition of back-stresses [Chaboche 2008, Samrout et al. 1997]. To account for the slight strain rate dependence of the material, the plastic multiplier is expressed using Norton's law as:

$$\dot{p} = \dot{\varepsilon}_0(\phi/\sigma_0)^n \tag{III.9}$$

Finally a specific form for the R function was chosen as:

$$R(p) = R_0\left(1 + Q_1(1 - \exp(-k_1 p)) + Q_2(1 - \exp(-k_2 p))\right) \tag{III.10}$$

III.4.2 Numerical analysis

The proposed model in this study is implemented in the FE software Z-set [Besson and Foerch 1997, Foerch et al. 1997]. An implicit scheme is used to integrate the constitutive equations. The consistent tangent matrix is computed using the method proposed in [Simo and Taylor 1985]. Finite strains are accounted using a corotational frame as in [Sidoroff and Dogui 2001].

III.4.3 Parameter identification

The model developed in this study is complex and has several material parameters to be adjusted; the anisotropic yield function parameters (a, b_1, b_2, α, $c^1_{\mathrm{TT...ST}}$, $c^2_{\mathrm{TT...ST}}$), the kinematic hardening parameters (C and D) and the isotropic hardening parameters (R_0, Q_1, Q_2,b_1, b_2). In the following the model was simplified assuming $a = b_1 = b_2$. The parameter adjustment is carried out according to previous work [Bron and Besson 2004]. Tensile tests along L, T and D directions are used as well as all tests of notched bars with different minimum radii for the as-received and prestrained materials. In case of tensile smooth bars, force-axial displacement curves are used together with the relationship between axial and diameter displacement (Fig. III.4-b). In case of notched bars, force-diameter reduction curves are used. In both cases, diameter displacement is measured along S direction. Adjusted material model parameters are shown in Tab. III.2.

III.5 Numerical results and discussion

Fig. III.9-(a)-(c) show the comparison of experimental and simulated true stress—true axial strain curves of smooth bar tests in different directions. For tests carried out on prestrained materials, the curves are shifted by the amount of plastic strain introduced by prestraining. As can be seen from these figures, the developed kinematic model can describe transient hardening at the early strain stage, which is dependent on reloading direction, after prestraining up to 0.06. For T loading direction, which is parallel to the prestrain direction, no transient stress-strain response is found, while in L and

Table III.2 : Material model parameters

Elastic properties	
Young's modulus E	200 GPa
Poisson's ratio ν	0.3
Kinematic hardening	
C, D	39794 MPa, 287
Isotropic hardening	
R_0	375.5 MPa
Q_1, k_1, Q_2, k_2	0.15, 78.6, 0.46, 18.8
Strain rate dependence	
$\dot{\varepsilon}_0$, σ_0, n	1 s^{-1}, 55 MPa, 5
Anisotropic yield model	
$a = b_1 = b_2$, α_1, α_2	8.74, 0.7, 0.3
c^1_{TT}, c^1_{LL} , c^1_{SS}	1.05, 0.82, 0.66
c^1_{TL}, c^1_{LS} , c^1_{TS}	0.93, 1.15, 1.19
c^2_{TT}, c^2_{LL} , c^2_{SS}	0.94, 1.05, 0.74
c^2_{TL}, c^2_{LS} , c^2_{TS}	0.80, 0.99, 1.17

D directions, which are orthogonal and diagonal to the prestraining direction respectively, a significant change in stress-strain curve in the small strain region is indicated after the reloading.

Furthermore, as the developed model includes anisotropic yield function, it can represent anisotropic plastic flow for all loading directions as shown in Fig. III.9-(d).

Fig. III.10 compares the experimental and simulated force-diameter reduction curves of NT specimens for both the as-received and prestrained materials. Because the developed model does not incorporate a damage model representing ductile failure, simulated and experimental curves are, here, compared up to ductile initiation point. For all types of notched bar specimens, the agreement is good up to the drop point for both load orientations and all prestrain levels. The results indicate that the developed model could be used for accurate prediction of stress triaxiality and equivalent strain at ductile fracture initiation which both are the most important factors [Ohata and Toyoda 2004, Decamp et al. 1997] to develop a damage model representing ductility of anisotropic steels in the future.

Diameter reduction along the S direction as function of longitudinal strain of NT specimens loaded in T and L load directions is shown in Fig. III.11 for the three notch geometries (as received state). The developed model can also represent anisotropic flow behavior in all NT specimens. Note that this set of data was not used for fitting material parameters.

Fig. III.12 presents experimental and numerical stress-strain curves of tensile tests done in a plane strain state for as-received and 6% prestrained material. The simulations by the identified model accurately predict stress-strain responses in L direction (orthogonal to prestrain load) as well as in T direction (parallel to prestrain) for the as-received and the prestrained steels.

Fig. III.13 shows the simulated yield surface for biaxial loading in the T–L plane after prestraining to the different experimentally prescribed levels (T direction). It is shown that hardening in initially strongly kinematic (as received $\rightarrow$ 2%) leading to a translation of the yield surface. Due to the high value of parameter D, $\underline{X}$ rapidly reaches its saturation value and hardening tends to become more isotropic (2%$\rightarrow$ 6%) with the yield surface growing.

III.6 Application to pipe bending simulation

The strain-based design methodology requires to carry out tests on large pipe elements (see e.g. [Timms et al. 2009, Tsuru and Agata 2009]). The purpose of this section is to propose a finite element simulation of such tests taking into account the anisotropic material behaviour. Using the developed constitutive model, bending simulation of a pipe prestrained during the forming process was conducted to clarify the prestrain effect on the buckling capacity. In this study, prestraining was assumed to be monotonic plane strain tension along T direction and prestrain ($\varepsilon_{\mathrm{TT}}$) was applied up to 6 %. The zero strain direction corresponds to the L direction which is representative of UOE forming.

III.6.1 Finite element simulation of pipe bending experiments

The finite element model for pipe is shown in Fig. III.14. The nominal diameter ($D_n = 2R$) to the thickness (t) ratio of the pipe was 47. The length (L) was 8 times the diameter. Due to symmetries, only $\frac{1}{4}$ of the the pipe was actually meshed. A local material frame is used to define the material principal directions (T, L and S) with respect to the pipe: L corresponds to the pipe axis and is constant whereas T and S vary depending on the angular position. All calculations were performed using 3D linear elements (eight nodes) using full integration and a F-bar formulation to avoid spurious pressure oscillations [Hughes 1980]. An initial internal pressure, P, equal to 80% of the burst pressure (P_c) is applied to the tube. P_c is given by:

$$P_c = \frac{2t}{D_n}\sigma_{\mathrm{X100}} \tag{III.11}$$

where $\sigma_{\mathrm{X100}} = 100$ kpsi$= 690$ MPa (so that $P = 23.5$ MPa) . The bending angle (θ) is then applied rotating a rigid plate attached on one pipe end. The rotation axis is allowed to move freely along the pipe axis to avoid generating spurious axial tensile forces. Simulations are carried out assuming either (i) pure bending or (ii) bending assuming an end-capped pipe so that an axial force equal to $\pi R^2 P$ is generated. In the following bending moments will be normalized by the pure bending limit load [Huh et al. 2007] assuming a flow stress equal to σ_{X100}:

$$M_0 = D_n^2 t \sigma_{\mathrm{X100}} \tag{III.12}$$

In order to trigger buckling at the center of the pipe, a small geometric imperfection was inserted. It consists in a radial perturbation of the pipe diameter given following the shell theory proposed by Timoshenko [Tsuru et al. 2008]. The perturbation is characterized by a wave length λ equal to :

$$\lambda = 2\pi \left(\frac{D_n^2 t^2}{48(1-\nu^2)} \right)^{\frac{1}{4}} \tag{III.13}$$

so that $\lambda = 16.75t$ in the present case. The prescribed relative perturbation δ is expressed as: $\delta = (D_M - D_m)/D_n$ where D_M and D_m as respectively the maximum and minimum diameters (see Fig. III.14). The radial perturbation is expressed as:

$$\Delta R = \delta \frac{D_n}{4} \cos\left(2\pi \frac{z}{\lambda}\right) \quad \text{for} \quad |z| < \frac{3}{4}\lambda \quad \text{and} \quad 0 \quad \text{otherwise} \tag{III.14}$$

where z denotes the longitudinal position (with $z = 0$ at the center of the pipe segment).

III.6.2 Simulation results

Fig. III.15 shows the effect of prestrain (between 0 and 6%) on bending behaviour under both pure bend and capped-end conditions. In both conditions, prestraining strongly affects the peak moment

(M_c) and the angle at the onset of buckling (θ_c), i.e. the angle corresponding to M_c. Both moment and angle are much higher under the end-capped condition than under pure bending. With increasing prestrain the peak moment increases while the critical angle decreases. In particular, the critical angle of a pipe bended under end–capped condition is strongly reduced by prestraining. A bulge is formed on the compressive side of the pipe (see Fig. III.15) for bending angles larger than θ_c is observed experimentally (see e.g. [Timms et al. 2009]). In long distance gas pipeline projects using the high design factor , the pipes buried under the ground might be subjected to move under end–capped condition. Furthermore, prestrain level due to pipe forming fluctuates along the circumferential direction of a line pipe. In the case of UOE pipes, the deviation of prestrain is distributed between -20% and $+50\%$ of the average prestrain level. Hence this numerical study suggests that prestrain history in pipe manufacturing process should be precisely controlled for line pipes used in strain-based design.

Fig. III.16 shows the effect of defect size on the critical bending moment and on the critical bending angle for a prestrain level equal to 2%. The simulation of bending was performed under two conditions: pure bending and end–capped. The critical buckling moment is not significantly affected by the pipe defect size. On the other hand, the defect size absolutely deteriorates the critical angle, especially under the end-capped condition. These results are similar to the previous study [Tsuru and Agata 2009].

III.7 Conclusions

In this study, a phenomenological model has been developed for anisotropic materials with combined isotropic/kinematic hardening. The generic model was applied to describe the behaviour of a X100 grade line pipe steel. For this type of material, plastic anisotropy is caused by the specific crystallographic texture existing in the mother plate as well as by prestrain induced by cold forming. Incorporating kinematic hardening in the model is crucial to be able to represent prestrain induced anisotropy. The model was identified using tensile tests carried out on smooth and notched axisymmetric bars and plane strain specimens. In order to distinguish isotropic and kinematic hardening, these tests were carried out on as-received plate material as well as on prestrained materials. The model was implemented in a finite element code and used to perform simulations of large scale pipe bending experiments. The numerical results suggest that prestraining in the pipe forming process significantly affects the bending capacity of pipes.

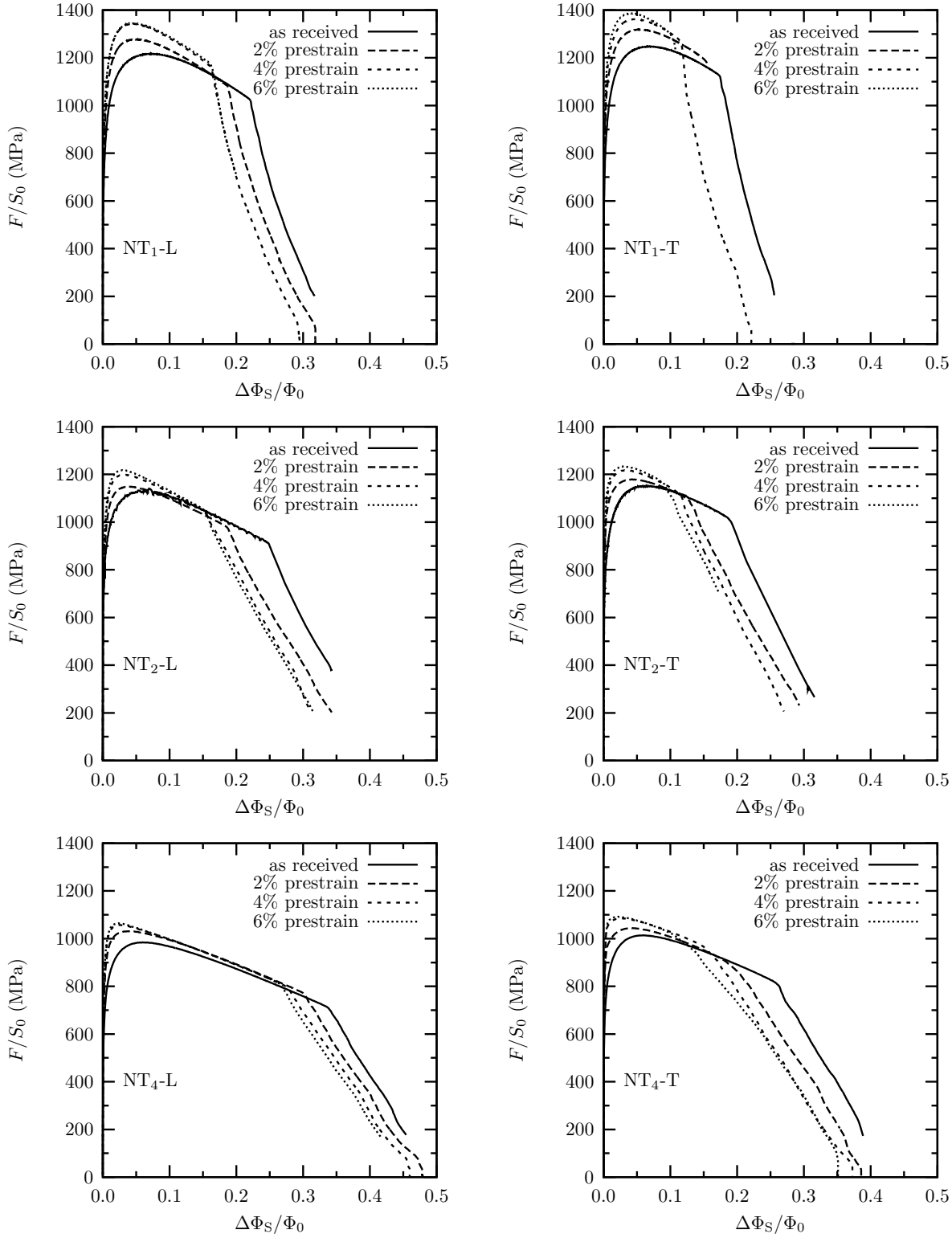

Figure III.6 : Force-diameter reduction curves in notched bar tests of as-received and prestrained steels

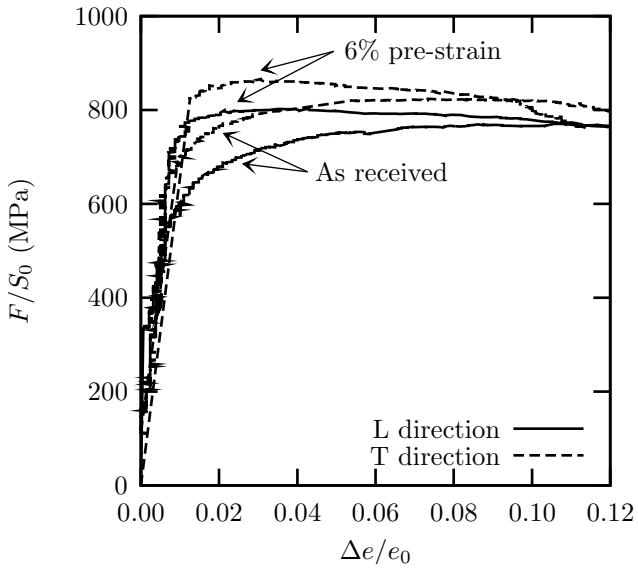

Figure III.7 : Force-thickness reduction curves in plain strain tests of as-receive ed and prestrain steels

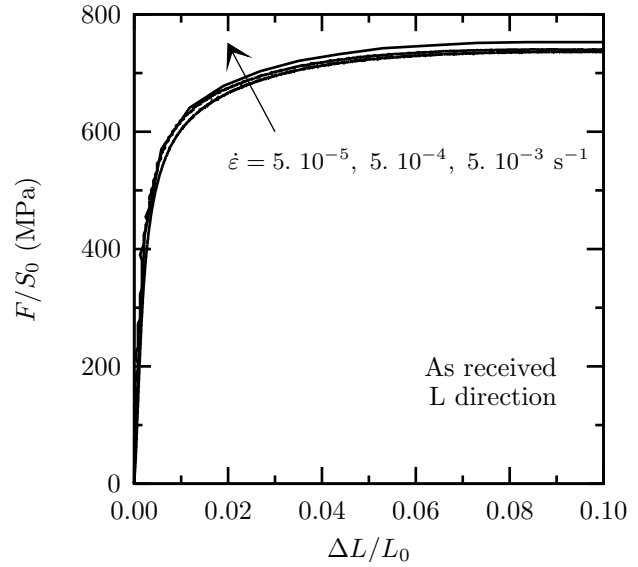

Figure III.8 : Nominal stress-strain curves for various imposed strain rates (L direction, as-received steel).

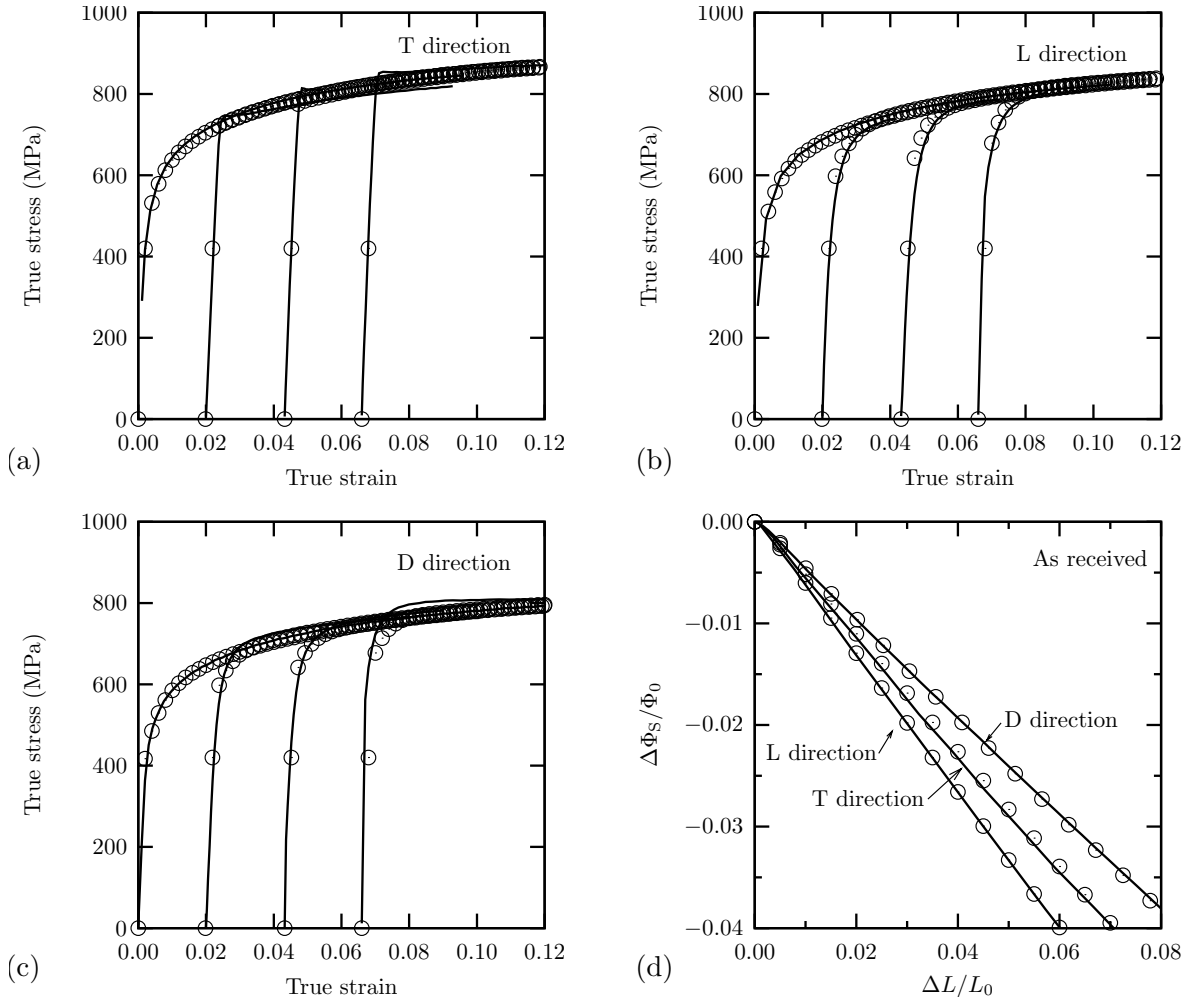

Figure III.9 : Comparison of experimental (lines) and simulated (symbols) true stress-strain curves in smooth bar tests for T (a), L (b) and D (c) loading. (d) Diameter variation as a function of elongation for various loading directions (as received state).

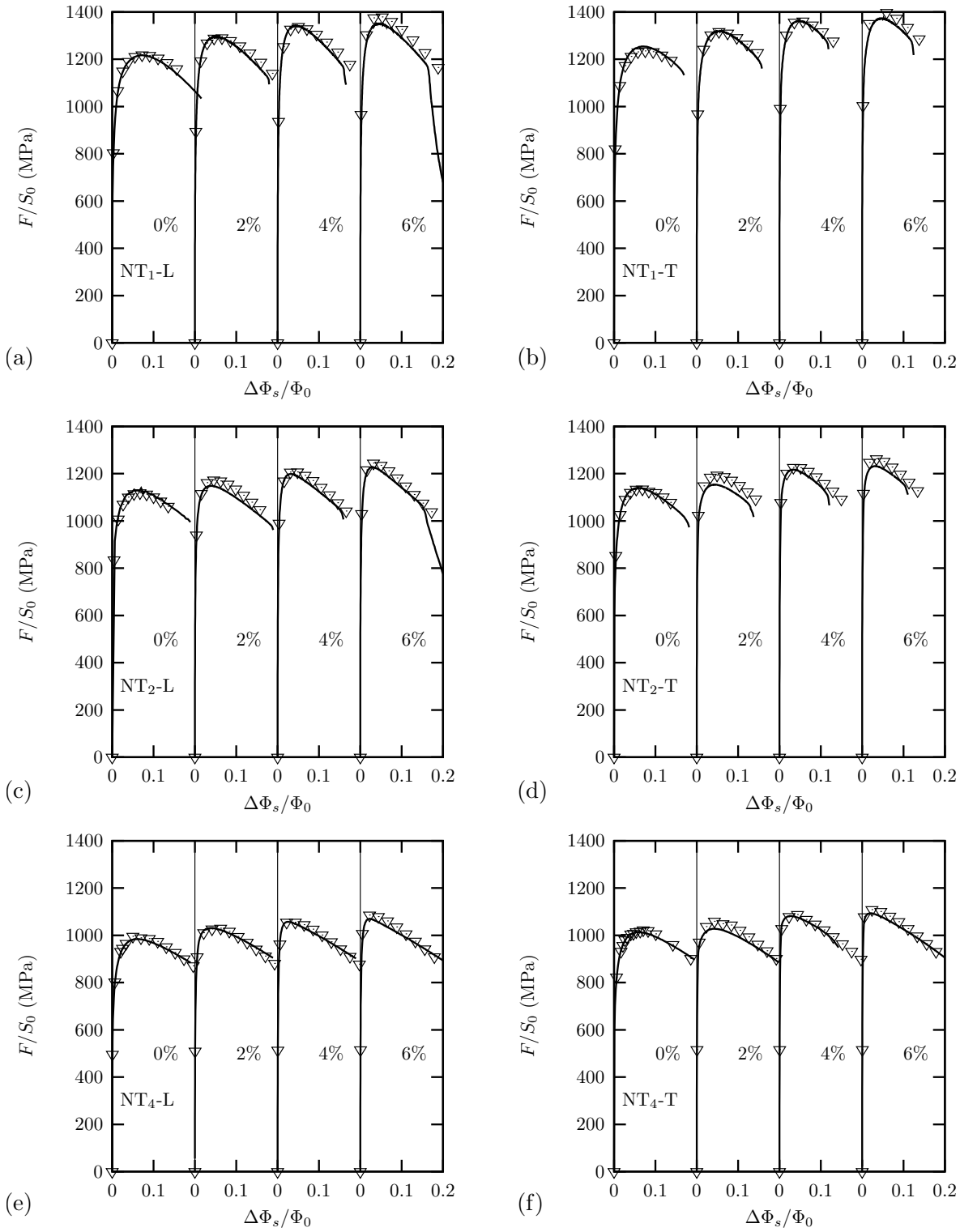

Figure III.10 : Comparison of experimental (lines) and simulated (symbols) force-diameter reduction curves in notched bar tests

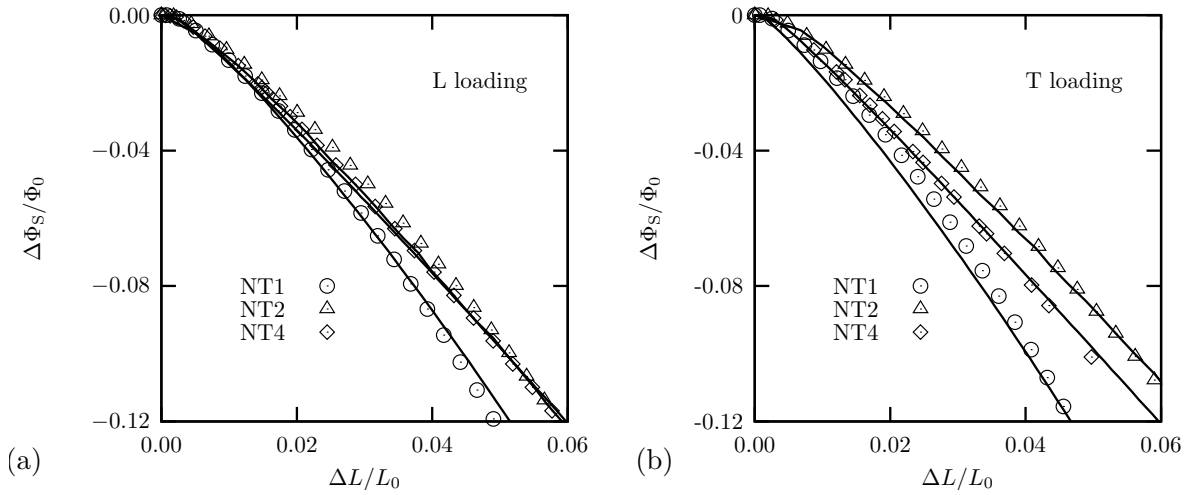

Figure III.11 : Comparison of experimental (lines) and simulated (symbols) diameter reduction-longitudinal strain curves in notched bar tests (as received state).

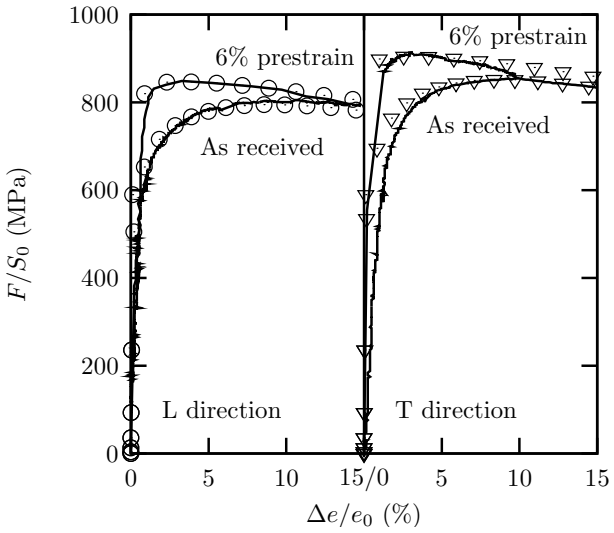

Figure III.12 : Comparison of experimental (lines) and simulated (symbols) results of plain strain tests.

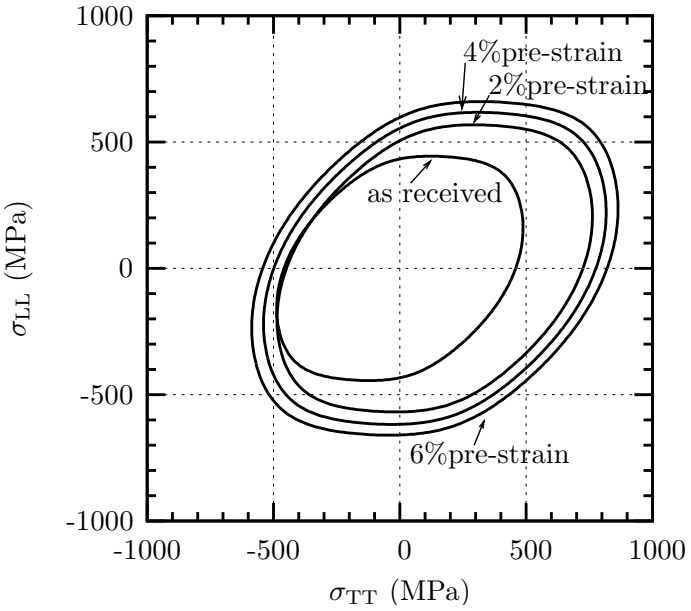

Figure III.13 : The calculated yield loci of the used steel before and after prestraining.

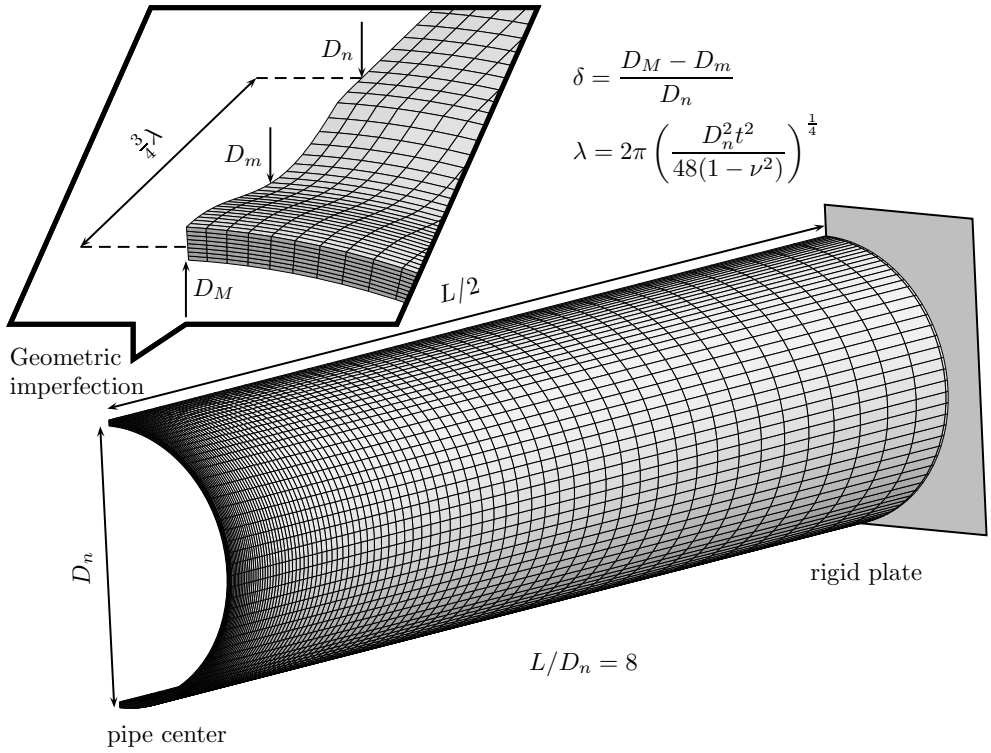

Figure III.14 : FEA model of pipe bending and geometric imperfection ($\delta = 5\%$).

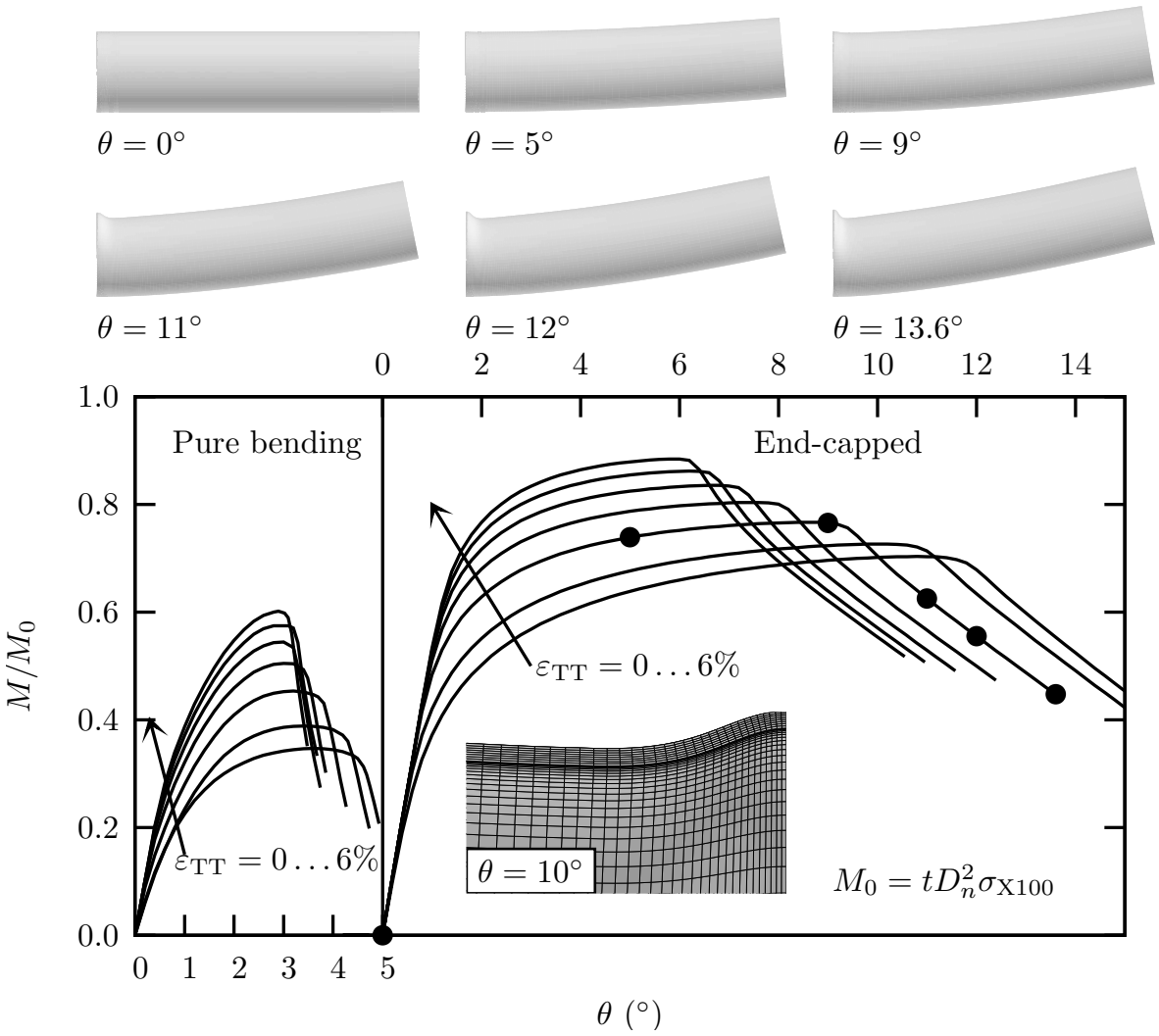

Figure III.15 : Effect of prestrain on bending resistance. Deformed pipes correspond to the simulation assuming end-capped condition and a prestrain level of 2%. Symbols on the curve correspond to the various loading steps. A detail of the bulge formed during load drop is also shown for the same conditions at $\theta = 10°$.

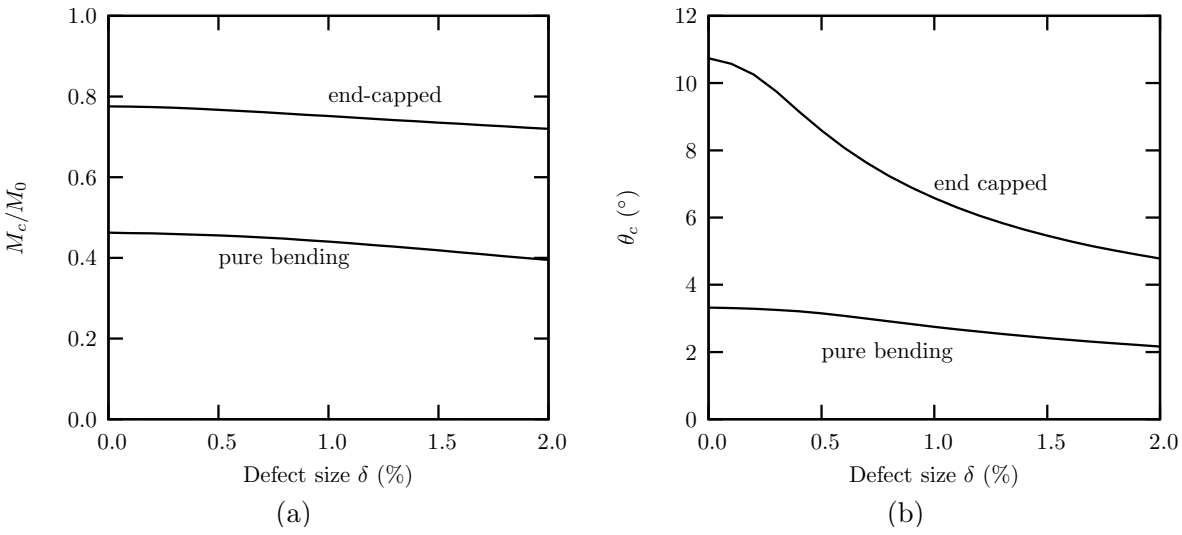

Figure III.16 : Effect of geometric imperfection on strain capacity (2% prestrain).

Chapter -IV-

Prestrain effect on ductility and toughness in a high strength line pipe steel

Contents

Résumé en français :

Le chapitre 4 expose les résultats expérimentaux relatifs aux effets observés de la pré-déformation sur la ductilité et la ténacité du matériau.

Les essais de traction sur éprouvettes lisses initiales ou pré-déformées montrent un effet d'anisotropie. L'anisotropie de rupture est clairement mis en évidence au travers des sections elliptiques après rupture pour les directions L et T. Le matériau chargé dans la direction T perd sa réserve d'écrouissage en cas de déformation et strictionne dès le début de la plastification pour une pré-déformation de 4 ou 6 $\%$. Les essais de traction sur éprouvettes entaillées montrent également une anisotropie selon la direction de traction. On observe de plus une ductilité qui décroit linéairement avec la pré-déformation et qui classiquement se réduit lorsque la triaxialité augmente.

Les essais de ténacité montrent une valeur J_0 (initiation à la rupture) indépendante de la géométrie (CT, SENB et SENT) et de la direction de sollicitation mais sensible à la pré-déformation. Par contre, à l'inverse la propagation de la rupture, représenté par le module $\partial J/\partial(\Delta a)$, est fortement dépendante de ces deux paramètres mais très peu de la pré-déformation.

Enfin, des observations des surfaces de rupture au MEB ont été réalisés pour les éprouvettes de traction (ST et NT) et les éprouvettes CT. L'examen des faciès de rupture met en évidence deux populations de vides : ceux qui nucléent en premier autour des inclusions primaires d'oxydes de Ti et ceux qui apparaissent ensuite au niveau des inclusions secondaires de carbures de fer. Les éprouvettes avec un taux de triaxialité élevé (éprouvettes CT et NT les plus sévères) montrent un taux de nucléation et de croissance importants des inclusions primaires alors que les éprouvettes lisses ST et les éprouvettes entaillées les moins sévères révèlent la présence de la seconde population. Un faible effet de direction de chargement ou de la pré-déformation est observé.

IV.1 Introduction

Demand for development of natural resources becomes strong as consumption of energy is increasing around the world. Natural gas is the cleanest of all fossil fuels. Generally, gas is transported from the product to consumer area by pipeline. Application of higher strength steel line pipes leads to many benefits in a gas pipeline project, such as lower amount of steel required, lower transportation cost and lower laying cost. X90, X100 and X120 high grade steel lines pipes were standardized as ISO3183 and API 5L. X100 and X120 steel has been already made for small-scale laying tests and operational trails [Asahi et al. 2009].

Generally, line pipes have been required to have high ductile crack initiation and tearing resistance for prevention of ductile running failure along the longitudinal direction of the pipe body by an accident during operation. Thus pipeline material standards recommend the use of Charpy impact and drop weight tearing tests, in order to evaluate fracture toughness of line pipes. The toughness value obtained from such small-scale tests correlates with full-scale pipe burst test result on lower grade steel line pipes [Maxey 1981, Wiedenhoff et al. 1984, Civallero et al. 1981], whereas the correlation no longer holds for high grade line pipes such as X100 and X120 [Makino et al. 2008].

In addition, high strength line pipes subjected to environmental loads from offshore ice, discontinuous permafrost and seismic activity have been recently required to be able to exhibit plastic strain capacity in strain-based design [Lillig 2008]. In the design, tensile strain limit should be considered for welded line pipes. Defects are, generally speaking, embedded in a girth weld portion including weld metal (WM) and heat-affected zone(HAZ) of a pipe. Weld material is required to over-match in order to prevent ductile failure from the initial defects in the WM. On the other hand, ductile crack propagates from initial crack located in the HAZ into the pipe body. Crack tearing is affected by the overmaching level and yield to tensile ratio of the pipe material. Small-scale fracture tests such as compact tension (CT), single-edge notched bend (SENB) and single-edge notched tension (SENT) are used to evaluate the ductile crack initiation and tearing resistance. There still remain problems in prediction of the tensile strain limit for a full-scale pipe structure, using fracture toughness values obtained by the small-scale tests.

As described above, the transferability of toughness between small test specimens and larger structure is an important issue in assessment of pipeline structure integrity. Thus it is necessary to use a validated model linking ductile fracture micromechanisms to full-scale component behavior.

Mechanical tensile properties of a high strength steel line pipe have been revealed in the previous works [Tsuru et al. 2008, Shinohara et al. 2008]. A high strength line pipe has anisotropic hardening; the stress-strain curve is quite different between the longitudinal direction and the circumferential direction. The anisotropy of the high strength pipe is due to crystallographic texture of the mother plate that is sharpened through thermo-mechanical control process (TMCP) in a heavy plate mill. The anisotropic hardening is further enhanced during a pipe forming process because plastic strain is introduced to the pipe. It is also important to note that whereas the material has a very high yield stress, its hardening capability is limited. This causes for instance early necking during tensile tests.

The uniform elongation is between 6 and 8% for the mother plate but tends to decrease after UOE forming as this process involves plastic (pre)straining of the material.

Some experimental tests and numerical analysis have been conducted for prestrain effect on ductile fracture [Sivaprasad et al. 2000, Enami 2005, Baek et al. 2010]. In HSLA steels, ductile fracture toughness remained invariant up to 2% prestrain, whereas the toughness was deteriorated with prestrain beyond 2% [Sivaprasad et al. 2000]. In the case of conventional structural steel, compressive prestrain up to 30% leaded to cleavage cracking and reduced ductility significantly [Enami 2005]. In API 5L X65 line pipes, prestrain up to 5% had little effect on decreasing ductile fracture toughness of specimens loaded along the longitudinal direction while Charpy impact energy along the transverse direction considerably decreased with increasing the prestrain level [Baek et al. 2010].

In this study a grade X100 line pipe steels was tested in the as-received state and in several prestrained states (2, 4 and 6%) to evaluate the effect of prestrain on both ductility and toughness. Test specimens include tensile tests on smooth and notched bars and tests on precracked specimens (CT, SENB and SENT).

IV.2 Material and experimental procedure

The used material is a high strength steel plate with a 16 mm thickness which is used to manufacture line pipes produced in a commercial heavy plate mill. The chemical composition is shown in Tab. IV.1. The plate was made through TMCP and accelerated cooling process in the mill. The material has a dual phase microstructure consisting of fine polygonal ferrite and bainite structure as shown in Fig. IV.1.

Table IV.1 : Chemical composition of the used steel (weight %).

C	Si	Mn	P	S	Ti	N
0.051	0.20	1.95	0.007	0.0015	0.012	0.004

Others: Ni, Cr, Cu, Nb.

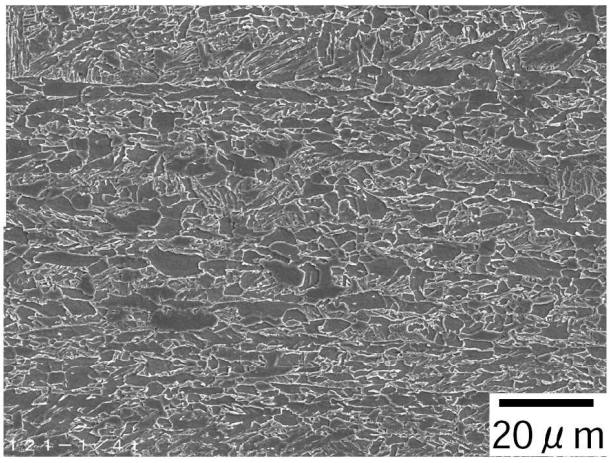

Figure IV.1 : SEM image of the steel plate used in this study (Nital etching).

The steel has anisotropic mechanical properties due to development of a specific crystallographic texture by TMCP ; hence it it important to keep track of the material principal axes. In the following,

the longitudinal direction, which is corresponding to the rolling direction, is referred to as L; the transverse direction is referred to as T, the diagonal direction in the L—T plane is referred to as D and the short transverse (thickness) direction is referred to as S.

Prestrain tests were first conducted, using a 4000 kN tensile testing machine. Large flat tensile specimens (see Fig. IV.2) were machined so that a 200mm×100mm zone, where applied strain is uniform, could be produced at the center of the specimen. Strain gauges were glued on the surface of tested specimens to check the actual prestrain level. The level of prestraining was up to 6%. Prestrain was performed along the T direction which corresponds to the main deformation direction during pipe forming.

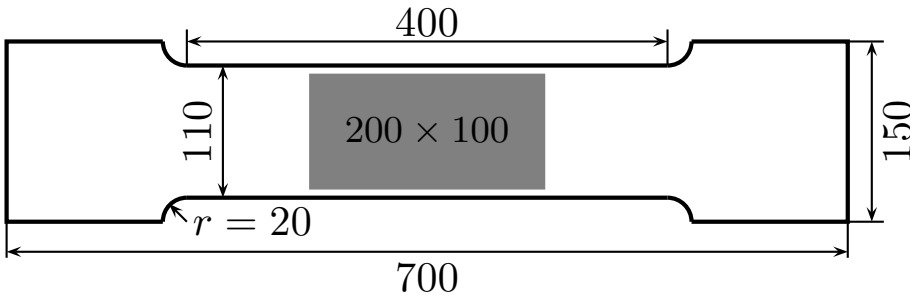

Figure IV.2 : Large tensile specimen for prestraining (dimension in mm). The gray area indicates the zone where prestrain is homogeneous.

A comprehensive characterisation of the mechanical properties of the steel was conducted along three different directions (L, T and D) using several types of tensile test specimens. The used geometries are presented in Fig. IV.3. All tests were performed at room temperature on a servo-hydraulic testing machine for the as-received and prestrained materials. Test specimens include smooth tensile bars (ST), axisymmetric notched bars with various notch radii (NT$_\chi$) and plane strain specimens (PE). Notched bars, which are often used to characterize rupture (see e.g. [Mackenzie et al. 1977]), are employed in this study as they allow to induce stresses in directions perpendicular to the main loading direction (in particular along the S direction) and consequently allow to test multi-axial stress states using a simple experimental setup. In addition notched bars allow to reach high levels of deformation so that the hardening behaviour is determined over a wide range of plastic strain. This is an alternative to the sole use of tensile bars which then need to be analysed beyond necking to reach high deformation levels [Mirone 2004, Zhang et al. 1999].

In the case of ST specimens, strain was measured using an extensometer with an initial gauge length of $L_0 = 9$ mm. ΔL denotes the gauge length variation. The imposed strain rate was: $\Delta\dot{L}/L_0 = 5.\,10^{-4}$ s^{-1}. In the case of ST and NT$_\chi$ specimens the diameter reduction ($\Delta\Phi_{\mathrm{S}}$) in the minimum cross section was measured along the S direction along which deformation is maximum. For PE specimens, thickness reduction (Δe) was measured at the center of the specimen. For both NT$_\chi$ and PE specimens the machine cross-head speed was selected so as to obtain a measured strain rate approximately of $5.\,10^{-4}$ s^{-1}. In the following F denotes the force, S_0 the initial specimen minimum cross section, Φ_0 the initial specimen minimum diameter and e_0 the initial PE specimen thickness.

For determination of ductile tearing resistance of the steel, three types of specimens, such as compact tensile (CT), single-edge notch bend (SENB) and single-edge notch tensile (SENT), were used. Their geometry was shown in Fig. IV.4. In all specimens, the thickness, B was 12.5 mm. CT and SENB specimens were pre-cracked in fatigue so that a total initial crack length of all specimens could be between $0.51W$ and $0.62W$. An initial crack of a SENT specimen was made by electron discharged machining without fatigue pre-cracking (the final notch radius is about 100 μm).

The J—Δa resistance curve was determined using multi-specimen technique in accordance with

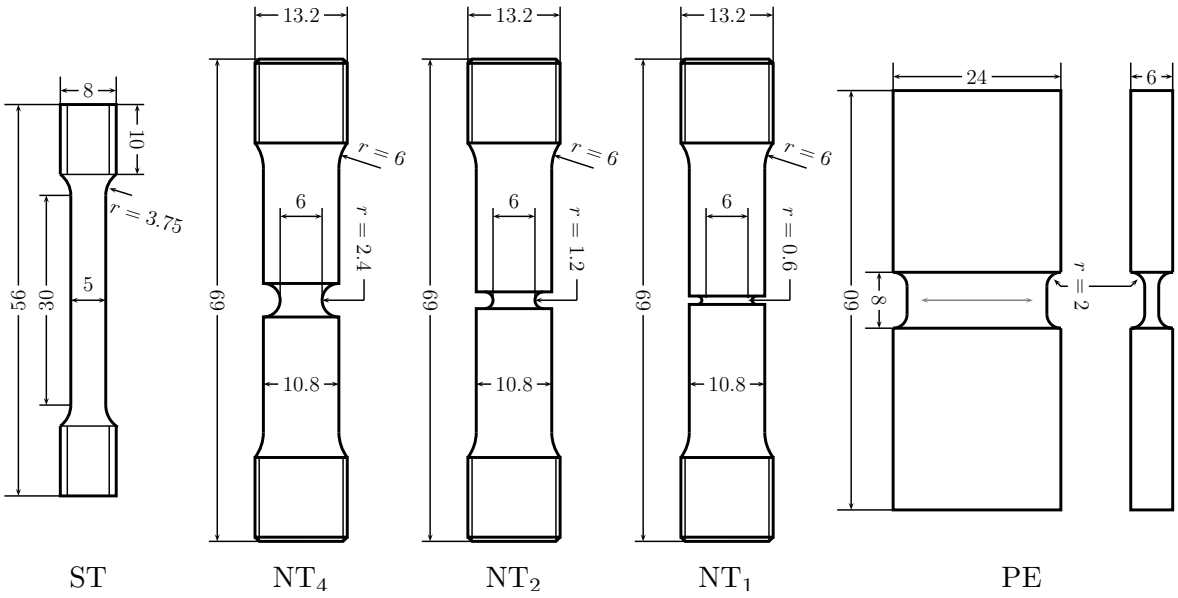

Figure IV.3 : Test specimens: smooth tensile bar, axisymmetric notched bars, and plane strain specimens (the gray line indicates the plane strain direction).

ASTM-1820 [ASTM 2006] for as received and prestrained materials. The fracture toughness test was conducted under displacement control at ambient temperature. The displacement rate was 1 mm/min. Force and displacement were simultaneously recorded during the test, in order to calculate J as follows:

$$J = J_{el} + J_{pl} \tag{IV.1}$$

where: J_{el} = elastic component of J, and J_{pl} = plastic component of J. J_{el} can be calculated from the following equation:

$$J_{el} = \frac{K^2(1-\nu^2)}{E} \tag{IV.2}$$

where: K = stress-intensity factor with $a = a_0$. J_{pl} can be calculated from the following equation:

$$J_{pl} = \frac{\eta A_{pl}}{B(W-a)} \tag{IV.3}$$

where: A_{pl} = plastic area under the load versus load-line displacement and $\eta = 1.9$ for SENB specimens, $2+0.522(W-a)/W$ for CT specimens, $1.0398-0.687(W-a)/W$ for SENT specimens. Values for parameter η were obtained from [ASTM 2006] for CT and SENB specimens. The formula proposed by Cravero and Ruggieri [2007] was used in the case of SENT specimens. The ductile crack extension, Δa, was directly determined on a fracture surface of the tested specimens, which were broken at liquid nitrogen temperature after unloading, by means of the 9-point averaging method

IV.3 Experimental results

IV.3.1 Tensile tests

Nominal stress-strain curves of smooth bar tests loaded along different directions are shown in Fig. IV.5 for the as-received and prestrained materials. Curves are plotted up to the ultimate stress

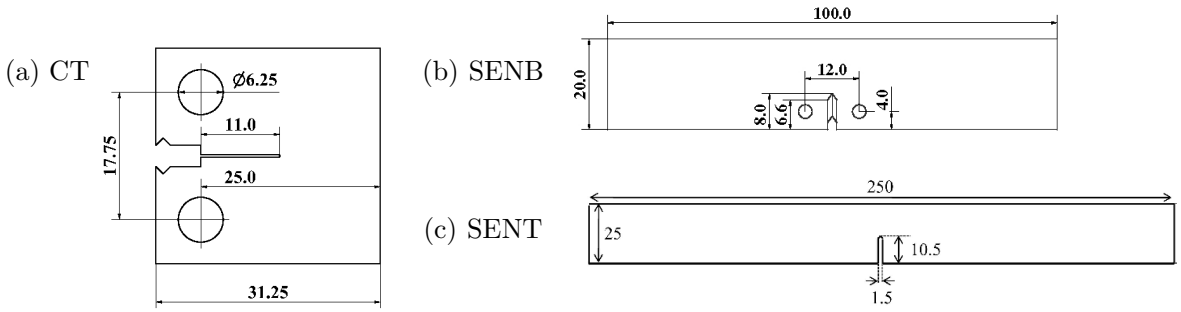

Figure IV.4 : Fracture mechanics testing: (a) compact tension (CT); (b) single-edge notched bend (SENB); (c) single-edge notched tension (SENT) specimens (all dimensions in mm).

point, which corresponds with the onset of necking. Flow stress in all directions increases with increasing prestrain level. Prestraining causes immediate appearance of necking in the T direction when prestrain levels is over 4%. The prestrained material has no longer hardening capability along the T direction. Some hardening capability is retained along L and D loading directions for all prestrain levels. These effects have been explained by the presence of kinematic hardening [Shinohara et al. 2010]. In addition, plastic deformation of the initially circular cross section depends on the loading direction. A fracture surface of the smooth tensile bar specimens is shown in Fig. IV.5. The photograph indicates plastic anisotropy in L and T directions. In that case plastic deformation is larger along the S direction. Plastic deformation appears as being isotropic in the case of D loading.

Fig. IV.6 shows force-diameter reduction for the various notched bar specimens in the L and T directions for the as-received and prestrained materials. Diameter reduction is measured along the S direction. In all types of notched bar specimens, the ultimate stress increases with the prestrain level. A sharp load drop point, which corresponds to the onset of a macroscopic crack at the center of a specimen, is observed. The critical diameter reduction at which the drop point is observed is referred to as $\Delta\Phi_S|_c$. The corresponding critical strain is defined as:

$$E_c = \frac{\Delta\Phi_S|_c}{\Phi_0} \tag{IV.4}$$

For a given prestrain level, E_c decreases with increasing notch severity. This corresponds to the well known effect of stress triaxiality (which increases with notch severity) on ductile damage development. For a given specimen type, the maximum load increases with increasing prestrain level due to work hardening. The critical strain at the onset of fracture, E_c, decreases with increasing prestrain.

Nominal stress-strain curves of plane strain specimens for the as-received and 6% prestrained materials are shown in Fig. IV.7. Flow stress in T loading direction is higher than in L direction. Prestrain causes flow stress higher and deteriorates work hardening in both loading directions.

Ductility for all types of tensile specimens is illustrated in Fig. IV.8. Ductility is characterized by the fracture area reduction, Z, which is defined as:

$$Z = \frac{A_0 - A_R}{A_0} \tag{IV.5}$$

where A_0 is the initial cross-section area and A_R the cross-section area at the fracture of the tested specimen. Ductility decreases with increasing notch severity; the reduction area of ST specimens is maximum whereas that of NT_1 specimen is minimum. The value is linearly decreasing by prestrain

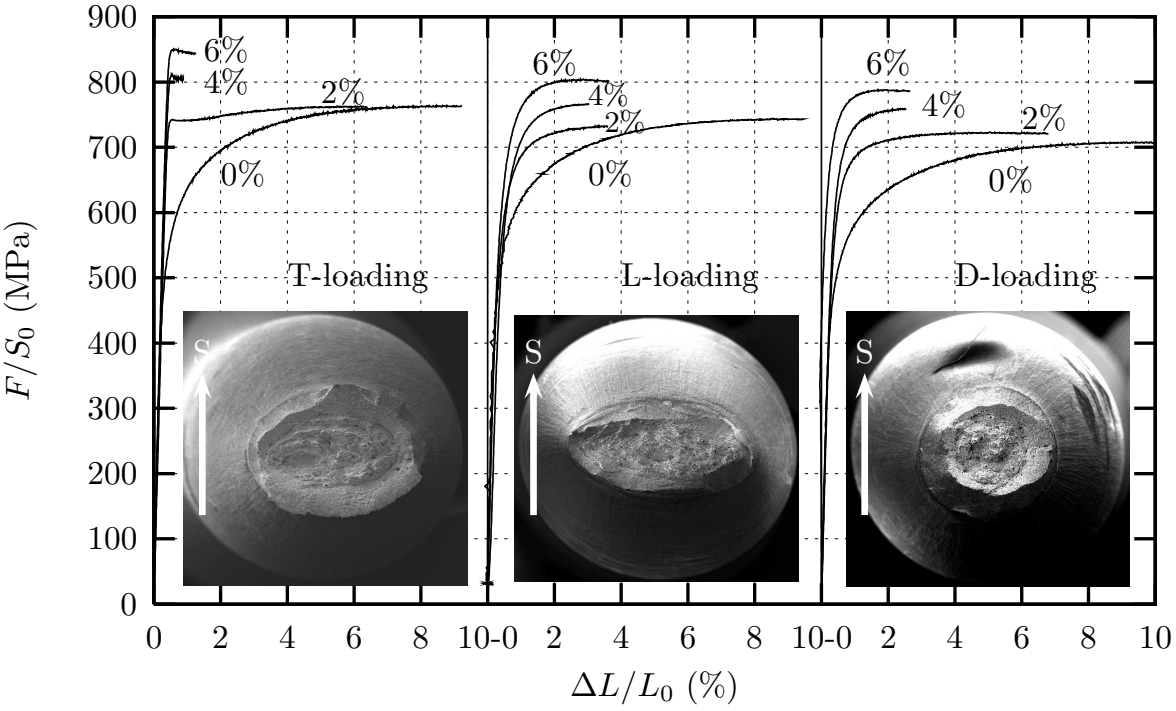

Figure IV.5 : Nominal stress (F/S_0) as a function of strain for T, L and D loading directions for the different prestrain levels.

level in all test cases. It is observed that Z is approximately reduced by the prestrain level ε_p^0 so that one gets:

$$Z(\varepsilon_p^0) = Z(0) - \varepsilon_p^0 \tag{IV.6}$$

In addition, Z is slightly higher in L loading direction than in T loading one showing that the material has an anisotropic ductility.

Effect of prestrain on ductile crack initiation behavior is shown in Fig. IV.9. The relative diameter reduction at crack initiation, E_c, is plotted for notched specimens as a function of the prestrain level. E_c decreases with increasing notch severity; the value is maximum in NT_4 and minimum in NT_1 specimen. It also depends on the loading direction; it is much higher in L loading direction than T direction. E_c is also lowered by prestrain. Dashed lines in Fig. IV.9 indicate a linear drop of the crack initiation strain against the prestrain level. E_c can be approximated as:

$$E_c(\varepsilon_p^0) = E_c(0) - \varepsilon_p^0 \tag{IV.7}$$

This trend is well observed for NT_4 specimens whereas some deviation is observed for NT_1 and NT_2 specimens.

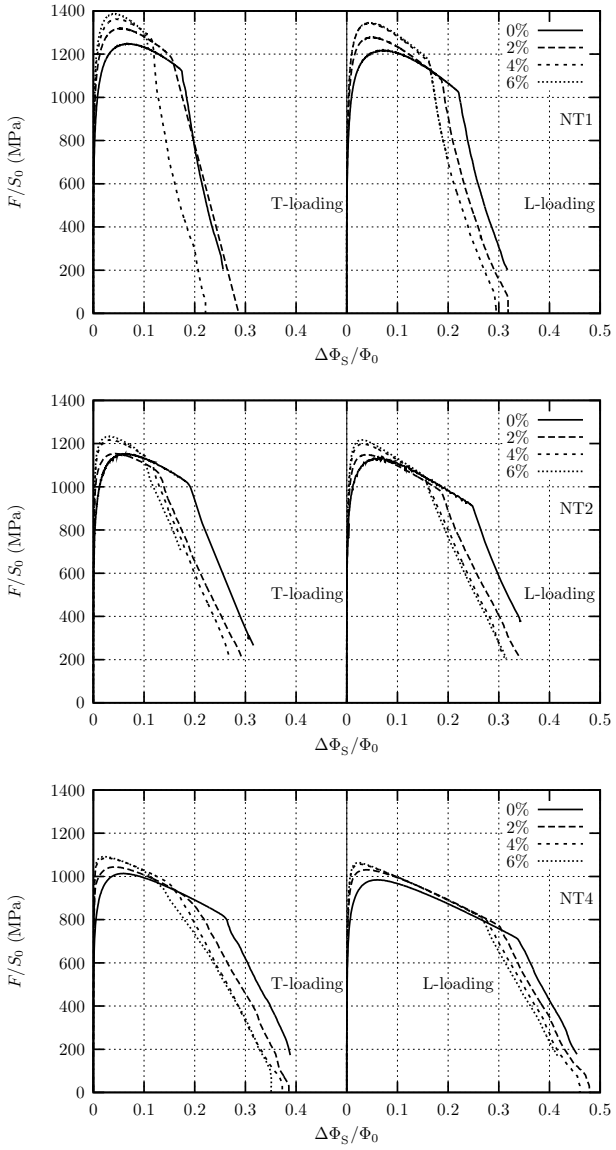

Figure IV.6 : Force-diameter reduction curves in notched bar tests of as-received and prestrained steels

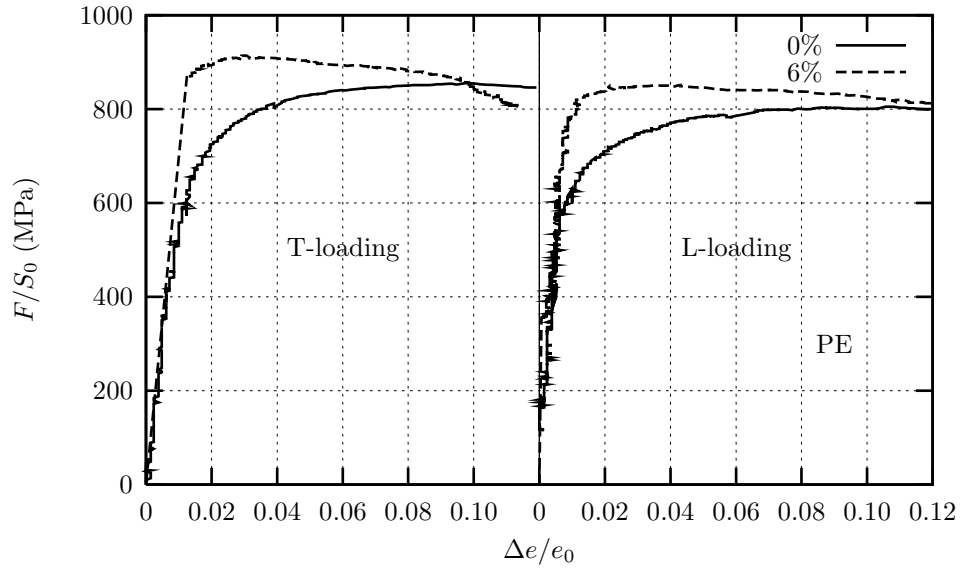

Figure IV.7 : Force—thickness reduction curves in plain strain tests of as-received and pre-strain steels

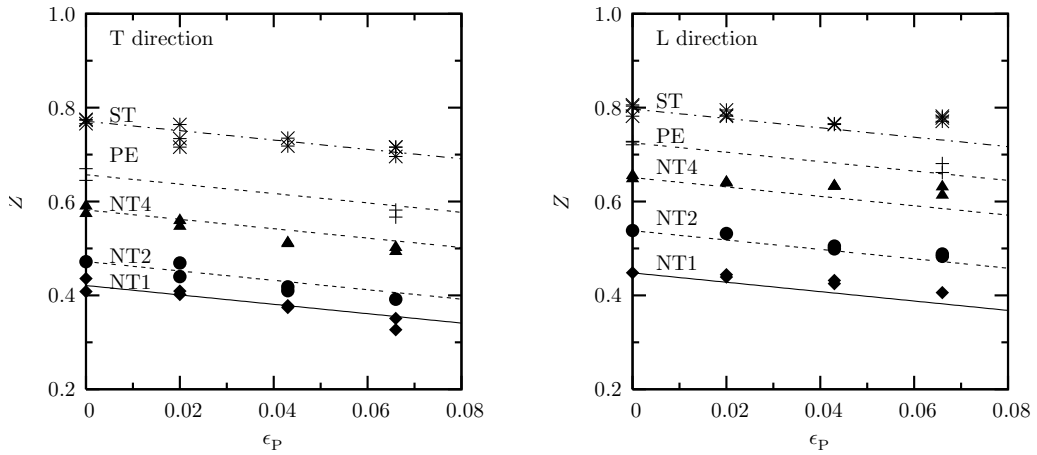

Figure IV.8 : Prestrain effect on reduction area Z

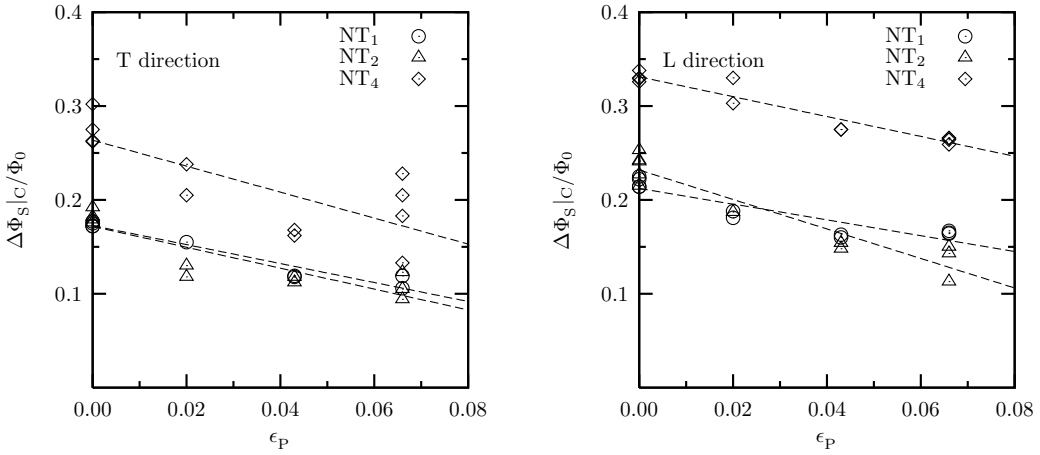

Figure IV.9 : Prestrain effect on the critical load drop point E_c

IV.3.2 Fracture toughness tests

Effect of prestrain on ductile crack growth resistance is investigated using CT specimens. The J-integral values against crack advance, Δa for the as-received and various prestrained materials are shown in Fig. IV.10. Toughness anisotropy is obvious. The J-integral value is higher for the L-T configuration than T-L one [1]. Prestrain significantly deteriorates the value for both configurations.

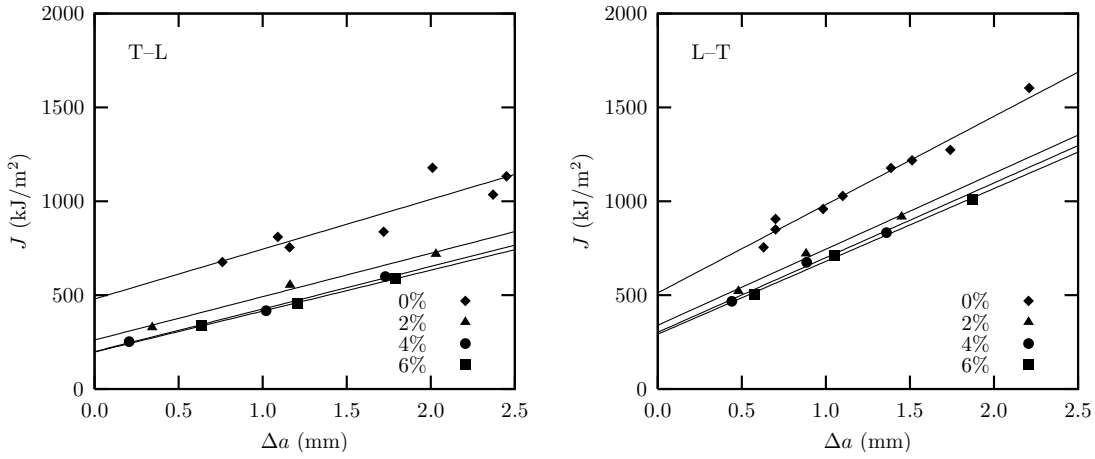

Figure IV.10 : J—Δa resistance curves of all materials for CT specimens for T–L and L–T loadings.

Fig. IV.11 shows comparison of the J—Δa relation between CT and SENB specimens for the as-received and 6% materials. The toughness is slightly higher in SENB tests than CT tests. Rupture anisotropy is still marked.

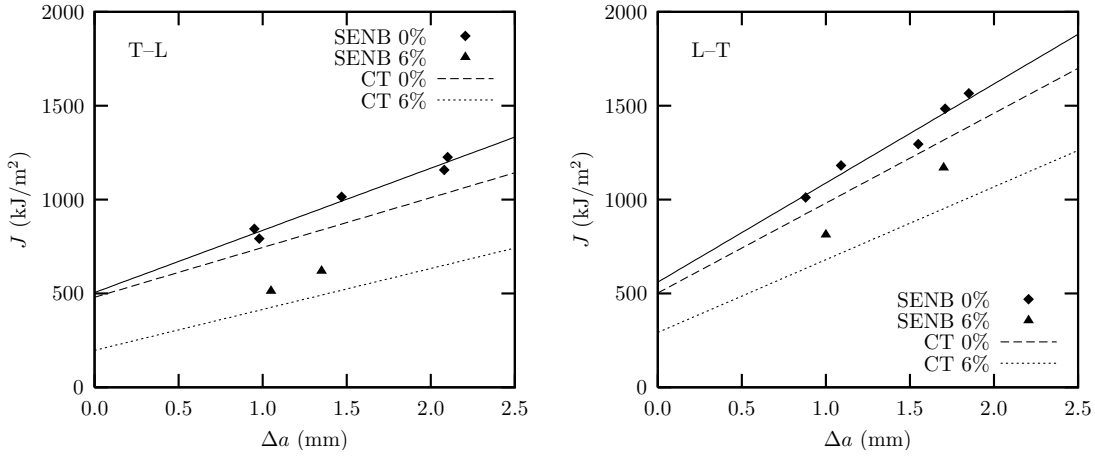

Figure IV.11 : J—Δa resistance curves for SENB specimens for L–T and T–L configurations and comparison with results for CT specimens.

In the case of SENT tests, results exhibit a much fracture toughness as shown in Fig. IV.12. Rupture anisotropy still exists but is less pronounced than in the case of CT or SENB specimens. The effect of pre-strain of also reduced (note that results were obtained for the T–L configuration only).

[1] In the L–T (resp. T–L) configuration, the specimen is loaded along the L (resp. T) direction whereas the crack propagates along the T direction (resp. L).

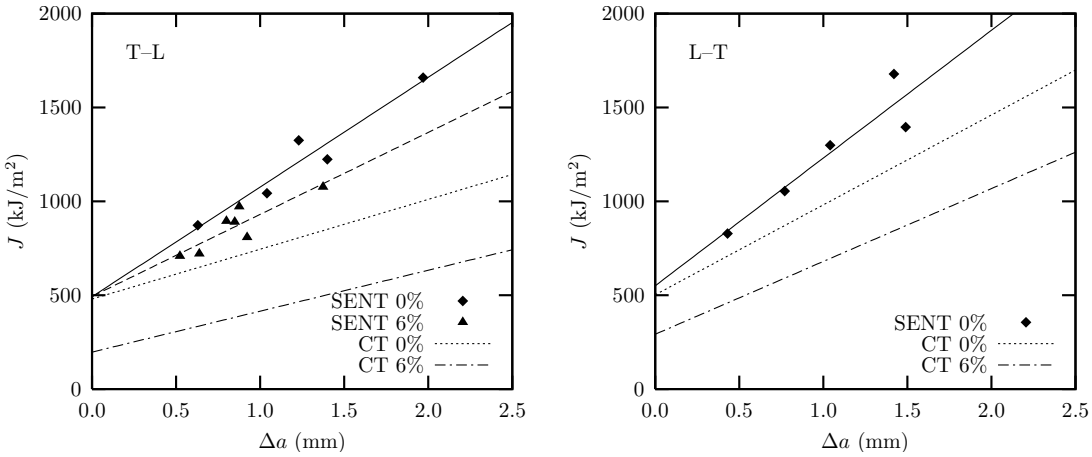

Figure IV.12 : J—Δa resistance curves for SENT specimens for L–T and T–L configurations and comparison with results for CT specimens.

Fig. IV.13 gathers values of J at crack initiation (J_0) obtained using a linear regression of the J—Δa curves (see e.g. fig. IV.12) for the various specimens geometries (CT, SENB and SENT) and both loading configurations (L–T and T–L) for the as received material. It is shows that J_0 hardly depends on the specimen geometry and is weakly affected by the loading configuration. The tearing resistance $\partial J/\partial(\Delta a)$ strongly depends on both the specimen geometry and the loading configuration. Its value is maximum in SENT tests and minimum in CT tests. $\partial J/\partial(\Delta a)$ is also higher in the L–T configuration than the T–L one.

Fig. IV.14 shows the prestrain effect on J_0 and $\partial J/\partial(\Delta a)$ of CT tests. J_0 is deteriorated by the prestraining for the both configurations, while the reduction of $\partial J/\partial(\Delta a)$ by the prestrain is very small. Opposite trends seem to be observed for SENT specimens ; note, however, that the number of tests is very limited in that case.

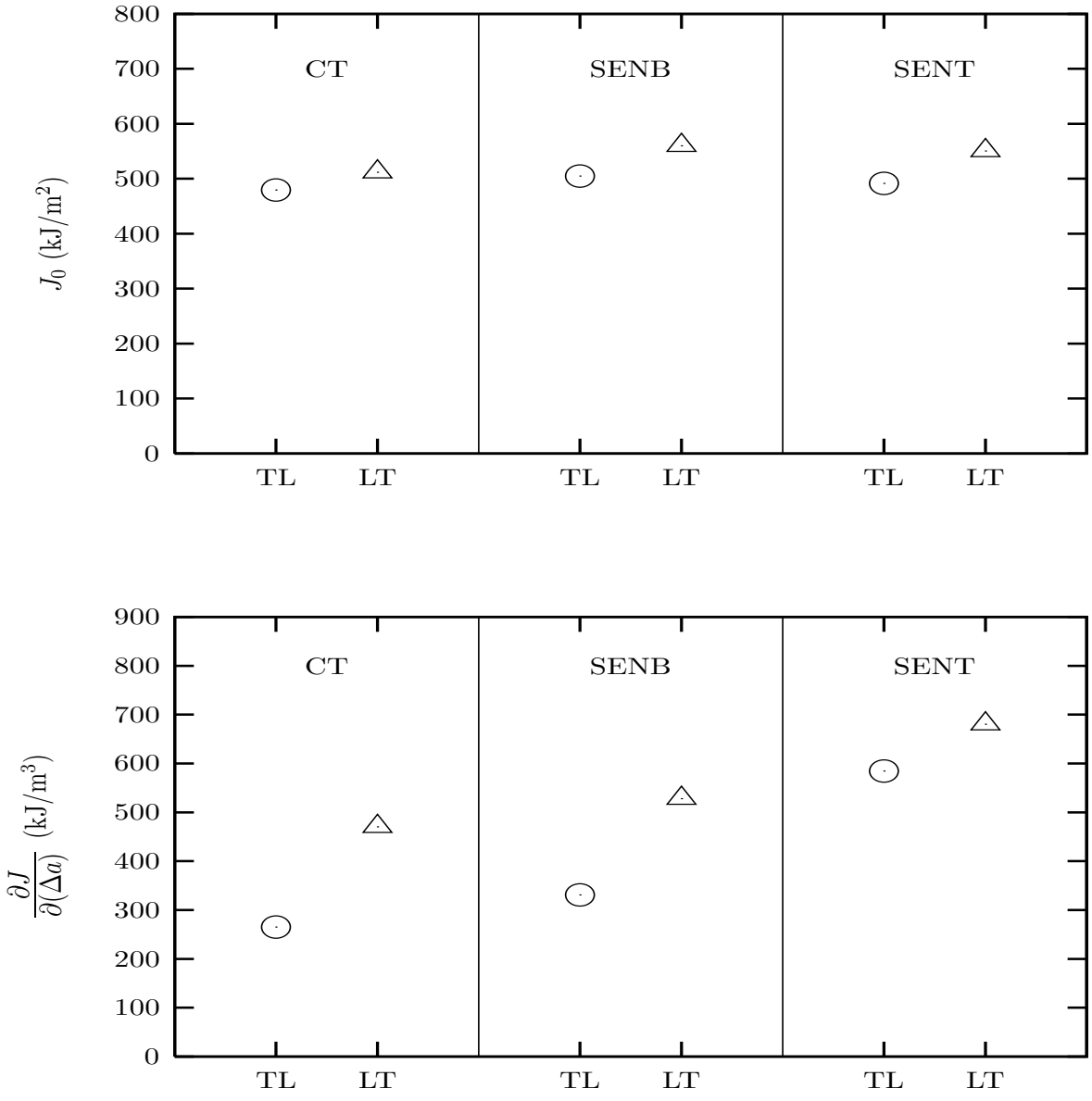

Figure IV.13 : comparison of J-integral value at crack initiation and crack advance ratio among CT, SENB and SENT tests (as-received material).

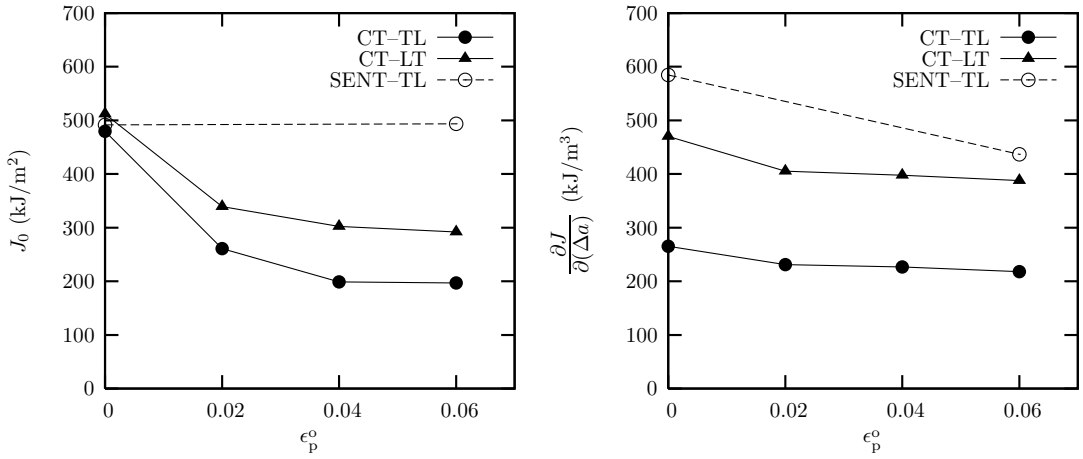

Figure IV.14 : Effect of prestrain on J–integral value at crack initiation, J_0 and on crack tearing resistance $\partial J/\partial(\Delta a)$ (CT and SENT test).

IV.3.3 Fractographic examination

Fracture surfaces of all tested specimens (ST NT and C(T)) are observed using scanning electron microscopy (SEM). In smooth and notched bar tensile specimens, macroscopic fracture surfaces present a cup-cone fracture pattern. The center of the fracture surfaces is closely observed as it corresponds to the location of ductile crack initiation.

Fig. IV.15 shows SEM micrographs of fracture surfaces of tensile specimens for the as-received material loaded along L-direction. In case of ST and NT_4 specimens, two populations of dimples are found: (i) large dimples (about 20 μm) mainly initiated at Ti-oxides, (ii) small dimples (about 1 μm) probably initiated at iron carbides. Large and small dimples are referred to as primary and secondary ones, respectively. On NT_2 and NT_1 specimens, the amount of the primary dimples is increased. This indicates that the primary voids first nucleate and grow under high triaxiality stress state. When stress triaxiality is relatively low (i.e. ST and NT_4), void growth is not as fast and plastic strain reaches the level necessary to nucleate the secondary voids so that both populations are observed on the fracture surfaces.

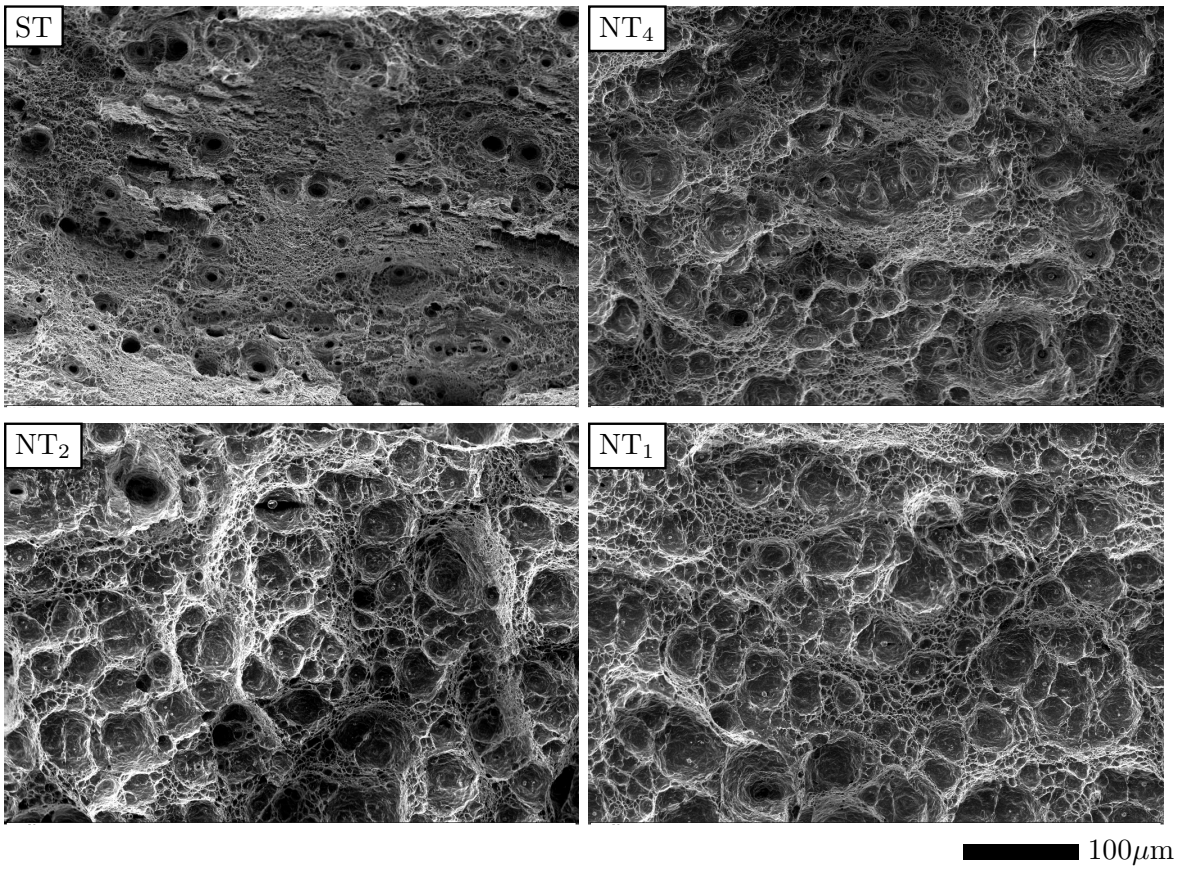

Figure IV.15 : Fracture surfaces of ST NT_4 NT_2 and NT_1 specimens (tested along the L direction)

As shown in fig. IV.16, primary void size (NT_1 specimens) is slightly larger in the T loading direction than the L one, while prestrain has no significant effect the void size. This result indicates that the primary void growth and coalescence could be dependent on loading direction, but independent on tensile prestrain level applied in this study.

Secondary void appearance is similar for the as-received and 6% prestrained materials loaded in both directions, as demonstrated in fig. IV.17 in the case of NT_4 specimens.

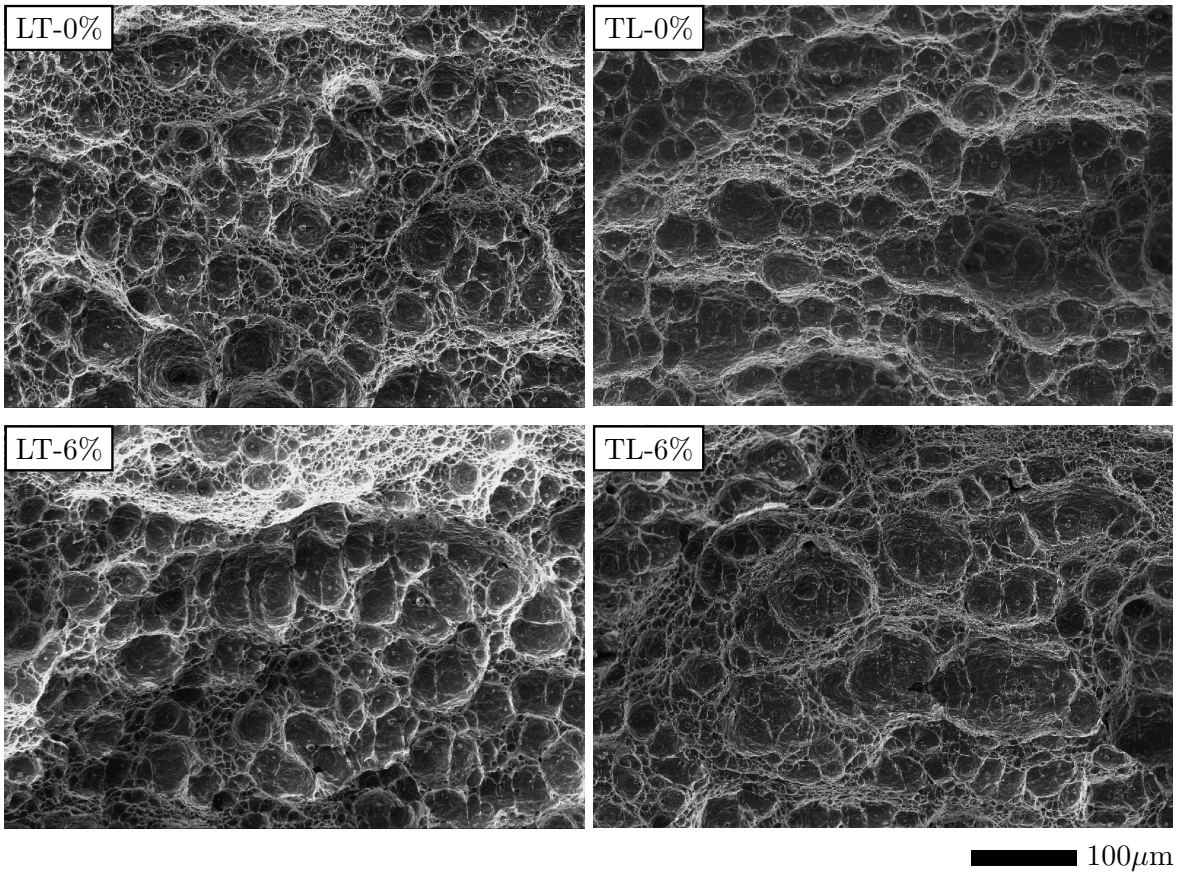

Figure IV.16 : Fracture surfaces of NT_1 specimens for the as-received and 6% prestrained materials

Fig. IV.18 shows fracture surfaces of C(T) specimens for the as-received and 6% prestrained materials. The fracture surface consists mainly in primary voids for all tested specimens. These photographs indicate that the main damage mechanism in C(T) tests is primary void growth and coalescence as in the severely notched tensile bar tests such as NT_1 and NT_2. Also, the primary dimple size is hardly changed by prestrain.

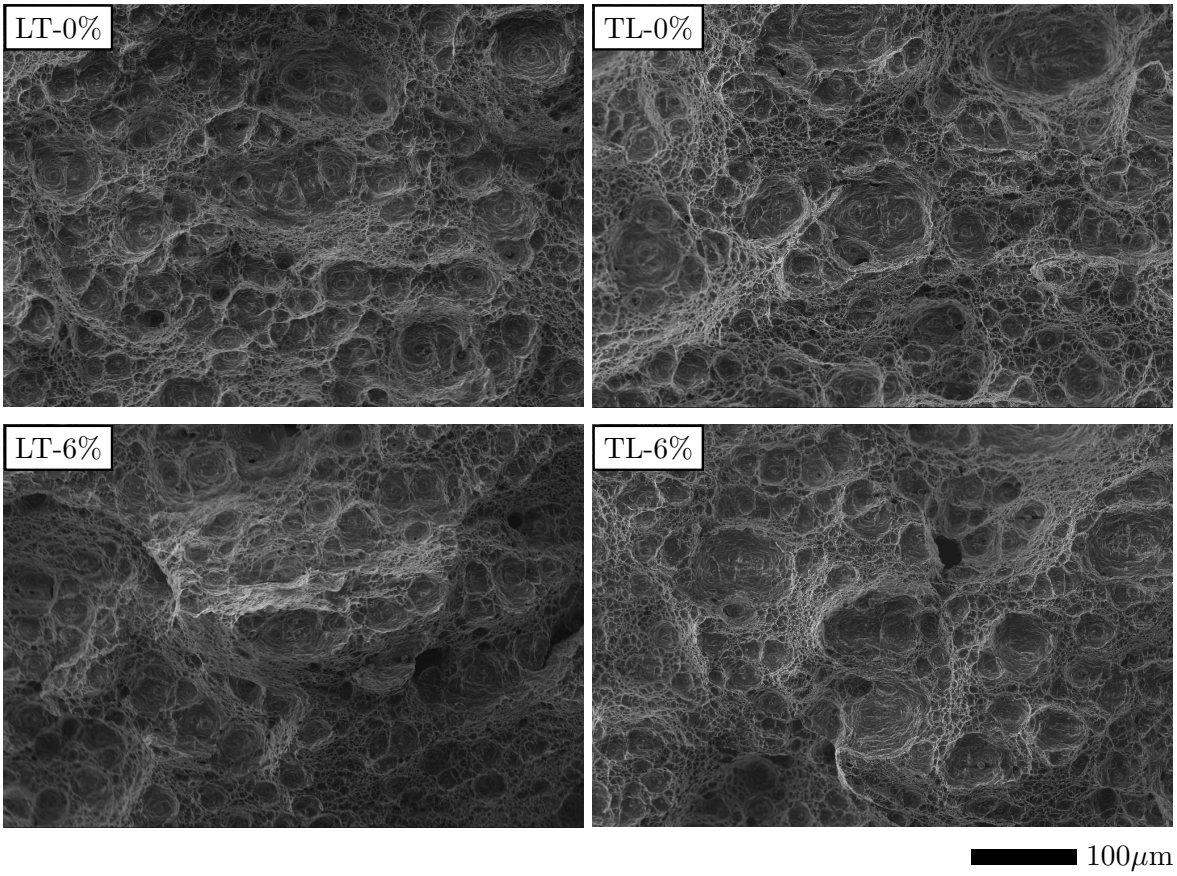

Figure IV.17 : Fracture surfaces of NT_4 specimens for the as-received and 6% prestrained materials

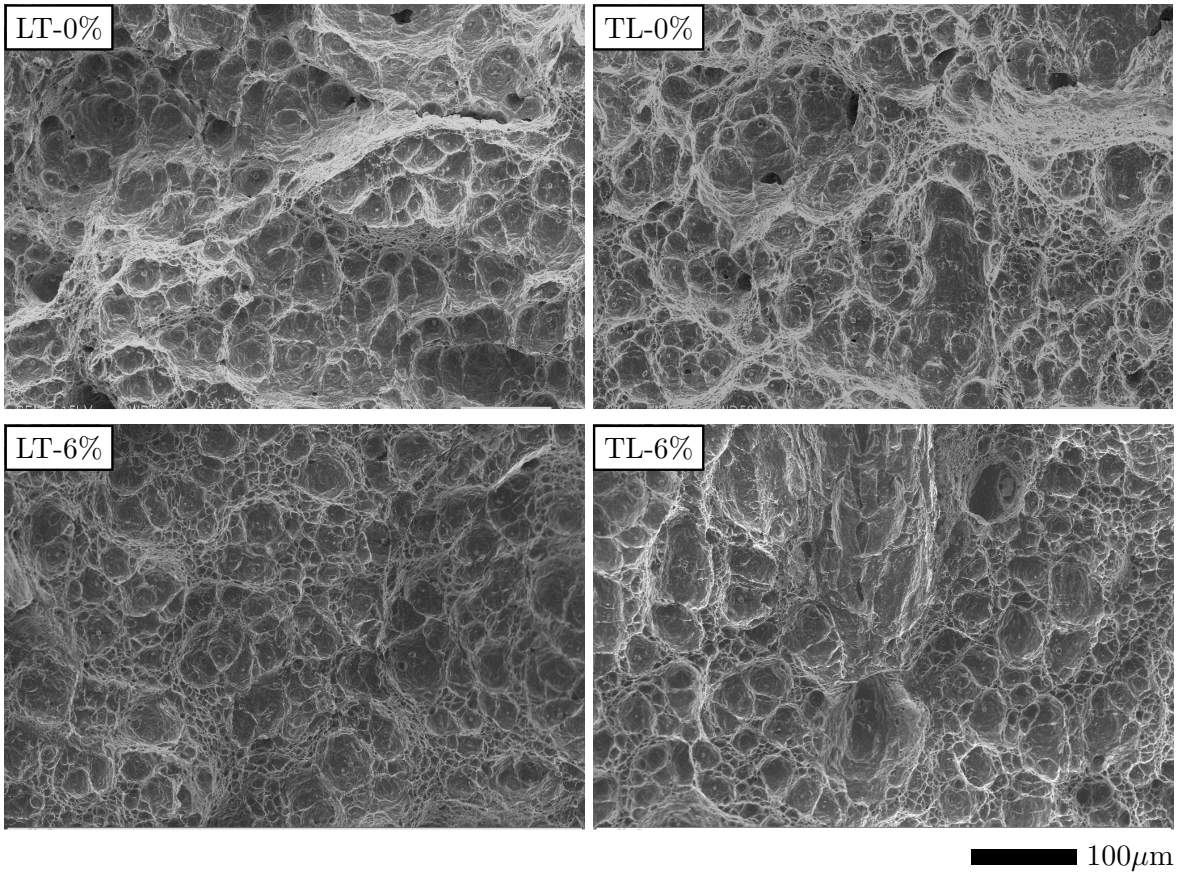

Figure IV.18 : Fracture surfaces of C(T) specimens for the as-received and 6% prestrained materials

IV.4 Conclusions

In this study, tensile tests via smooth and notched axisymmetric bars with different notch radii and plane strain specimens have been performed along different loading directions for as-received and prestrained materials, in order to investigate both anisotropic ductility and the prestrain effect for API grade X100 steel.

The critical strain at the onset of failure in the notched bar specimens was evaluated. The value was affected by loading-direction. The critical value was higher in L loading direction than T loading direction. Furthermore, the critical value was deteriorated by prestraining. The value was reduced by the prestrain level in the NT_4 specimen, while some deviation is observed for the other specimens. Ductility, which is characterized by the fracture area reduction in all tensile specimens, was evaluated. The value linearly decreased by the prestrain level in all types of tensile tests.

Three kinds of fracture toughness specimens (CT, SENB and SENT) were also used to evaluate the effect of prestraining on toughness of the API X100 steel. In the received state, the crack initiation was independent of the specimen geometry and the loading direction. On the other hand, the crack advance tearing resistance was strongly affected by the specimen geometry and the loading direction. The resistance for the L–T configuration was higher than for the T-L one. Value were lowest for CT specimens and highest of SENT specimens. Prestrain deteriorated crack initiation and had small effect on the tearing resistance in CT and SENB tests.

Chapter -V-

Anisotropic ductile failure of a grade X100 steel

Contents

Résumé en français :

Le chapitre 5 traite du modèle d'endommagement anisotrope établi pour représenter l'anisotropie du matériau. Le modèle de type Gurson-Tvergaard-Needlman, couplant le comportement et l'endommagement, a été étendu pour tenir compte de l'anisotropie ; ainsi :

- la plasticité anisotrope est introduite en utilisant la contrainte équivalente sE définie par le modèle de [Bron and Besson 2004] (cette contrainte remplace la contrainte de von Mises dans le modèle originel) ;
- la contrainte effective calculée de manière implicite est fonction à la fois de l'état de l'endommagement et de la contrainte macroscopique (supposée anisotrope au sens du modèle de Bron et Besson) ;
- la contrainte hydrostatique est remplacée par une moyenne pondérée des composantes de la trace du tenseur de contrainte anisotrope pour rendre compte de l'endommagement de façon phénoménologique.

Deux méthodologies sont abordées et discutées pour identifier les paramètres du modèle : calculs de cellules en utilisant le modèle de plasticité anisotrope sans couplage et identification sur la base des essais sur éprouvettes entaillées en utilisant le modèle d'endommagement couplé au comportement.

Les calculs de cellules montrent que la croissance des cavités peut être considérée comme « isotrope » en utilisant un taux de triaxialité des contraintes τ basé sur la contrainte équivalente σ_E au sens de Bron ($\frac{1}{3}\sigma_{kk}/\sigma_E$) contrairement à la définition standard ($\frac{1}{3}\sigma_{kk}/\sigma_{\mathrm{eq}}$) basée sur la contrainte de von Mises. Par conséquence, le modèle couplé identifié sur la base des calculs de cellule ne permet pas de reproduire l'anisotropie de rupture. Les analyses micro-structurales n'ont pas révélé de distribution anisotrope des inclusions qui pourraient expliquer cette anisotropie de rupture effective (notons que la fraction volumique est très faible donc difficilement détectable).

Les paramètres d'endommagement, identifiés sur la base des essais de traction entaillée NT, permettent de rendre compte de l'anisotropie de rupture. La validation du modèle est alors réalisée de manière concluante par la simulation des courbes J-Δa des éprouvettes fissurées CT et SENB. Les deux directions de chargement (L-T et T-L) montrent que le mécanisme d'endommagement est bien capturé et identique dans les deux cas.

V.1 Introduction

The worldwide increasing consumption of energy has led to the demand for development of natural resources such as oil and gas in remote locations. Economic studies have shown that development of oil and gas transportation over long distances requires the use of high grade steels whose mechanical properties allow to substantially increase the internal pressure for a given pipe thickness. Research has been focused of the development of new API grades such as X80, X100 or X120 [Graf et al. 2004]. The impurity content (mainly S and P) in these new materials is very low so that they have a low inclusion content and consequently a high ductility [Rivalin et al. 2000b]. In order to obtain high strength, these materials are produced using complex Thermo-Mechanical-Control-Processing which introduces preferred orientations within the steel and leads to anisotropic plastic properties in higher grades [Rivalin et al. 2000a, Tanguy et al. 2008, Shinohara et al. 2010, Treinen et al. 2008]. Rupture properties may also be anisotropic [Benzerga et al. 2004a].

Fully understanding and describing the material behavior is needed to produce safe and cost-effective pipelines. The anisotropic plastic behavior can be described by well established models such

as the Hill quadratic yield function [Hill 1950, Liu and Wang 2007]. However the simple Hill model does not allow to simultaneously describe yield stress anisotropy and Lankford coefficients so that more sophisticated models must be used [Barlat et al. 1991; 2005, Karafillis and Boyce 1993, Bron and Besson 2004]. These models can be extended to account for kinematic hardening [Vladimirov et al. 2010, Shinohara et al. 2010, Laurent et al. 2009]. Such an extension is needed in cases of non proportional loading such as UOE forming [1] or reeling-unreeling operations. Ductile damage is very often represented using models derived from the work by Gurson [1977] (see reviews in [Tvergaard 1990, Benzerga and Leblond 2010, Besson 2010]). They can be coupled with models for plastic anisotropy using the Hill criterion [Rivalin et al. 2000a, Brunet et al. 2005, Benzerga et al. 2004b, Ben Bettaieb et al. 2011] and also more advanced models as in [Bron and Besson 2006, Tanguy et al. 2008, Morgeneyer et al. 2009].

The purpose of the work is to study the interaction between anisotropic plasticity and ductile damage in the case of a grade X100 line pipe steel. Experiments including tests on tensile bars, notched bars, plane strain specimens, CT and SENB pre-cracked specimens were carried out. Plasticity is described using the model proposed by Bron and Besson [2004]. This model is coupled with a Gurson–like model for ductile damage which has been modified to account for plastic anisotropy and ductility anisotropy based on a phenomenological basis. The model is either tuned on unit cell simulations or directly on experimental results using notched bars. The tuned model is applied to simulate crack extension on CT and SENB specimens.

V.2 Material and testing procedures

V.2.1 Material

The material of this study is an experimental X100 grade high strength steel. It was supplied as a 16 mm thick plate by Nippon Steel Corp. This class of steel is used to manufacture pipelines. Compared to a pipe, which is usually produced by UOE forming, the plate can be considered as being in an unprestrained state. The nominal chemical composition is given in Tab. V.1. The plate was produced using thermo-mechanical controlled rolling and accelerated cooling (TMCP process). The resulting microstructure is mainly a dual phase structure consisting of fine polygonal ferrite and bainite (Fig. V.1).

Due to material processing, the plate has an anisotropic plastic behaviour [Tanguy et al. 2008] so that it is important to keep track of the material principal axes. In the following the longitudinal direction corresponding to the rolling direction is referred to as L; the transverse direction is referred to as T and the short transverse (thickness) direction is referred to as S. D stands for the diagonal direction (45 between direction L and T in the sheet plane). Note that grade X100 (i.e. a yield strength equal to 690 MPa along the T direction) is only reached in the pipe due to plastic straining during UOE forming operations.

Table V.1 : Nominal chemical composition (weight %).

C	Si	Mn	P	S	Ti	N
0.051	0.20	1.95	0.007	0.0015	0.012	0.004

Other minor alloying elements: Ni, Cr, Cu, Nb.

[1] UOE forming is a manufacturing process where the plate material is first deformed into an U-shape then an O-shape. The pipe seam is then welded. The pipe is finally Expanded using an internal mandrel. To achieve low ovality, the pipe is typically expanded by 0.8–1.3% from its diameter after the O-step [Herynk et al. 2007].

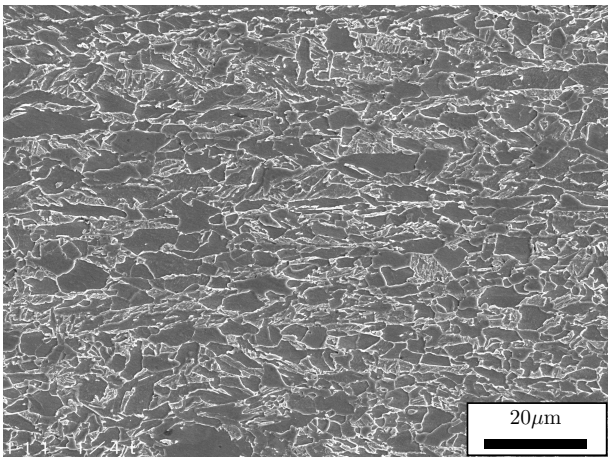

Figure V.1 : Plate microstructure consisting of fine polygonal ferrite and bainite (Nital etching, SEM observation).

V.2.2 Testing procedures

A comprehensive characterisation of the mechanical properties of the material was carried out along the different material directions using several specimen geometries to investigate both plastic and rupture properties. All tests were conducted at room temperature on a servo-hydraulic testing machine.

Smooth round tensile bars (ST, see Fig. V.2) are used to determine the hardening behaviour along L, T and D directions. Strain rate equal to $5.\,10^{-4}\mathrm{s}^{-1}$ is kept constant during the test. An extensometer is used to measure elongation. Diameter reduction across the S direction is also measured to obtain the Lankford coefficients. The S direction was carefully tracked during machining of specimens. The Lankford coefficient is defined as follows: $R_{\parallel} = \varepsilon_{\perp}/\varepsilon_{\mathrm{S}}$ where $\parallel$ corresponds to the loading direction and $\perp$ to the direction perpendicular to both the loading and S directions. ε corresponds to the true strain. $\varepsilon_{\perp}$ is computed assuming plastic incompressibility. Additional tests were conducted along the T direction at different strain rates ($5.\,10^{-3}\mathrm{s}^{-1}$ and $5.\,10^{-2}\ \mathrm{s}^{-1}$) to characterize strain rate sensitivity.

Axisymmetric notched tensile bars (NT_{χ}, see Fig. V.2) are used to characterise both plastic behaviour and damage growth. Tests are performed for L and T directions. Different notch radii are used to modify stress state and in particular the stress triaxiality ratio inside the specimens. Radii equal to 0.6, 1.2 and 2.4 mm are used corresponding to specimens NT_1, NT_2 and NT_4, respectively. The axial elongation as well as the minimum diameter variation along the S direction, $\Delta\Phi_{\mathrm{S}}$, are continuously measured. The mean strain rate computed from the diameter variation is controlled and fixed to $5.\,10^{-4}\mathrm{s}^{-1}$.

Wide and relatively thin specimens are used to generate plane strain (PE) conditions. The plane strain direction corresponds to the width of the specimen (see arrow in Fig. V.2) as deformation along this direction is constrained by the thicker lower and upper parts. Tests were carried out in the L and T main loading directions. An extensometer is used to measure the thickness reduction at the center of the specimen. Once again the displacement rate was chosen as that the strain rate at the centre of the specimen is about $5.\,10^{-4}\mathrm{s}^{-1}$.

Three tests were performed for each condition with very limited scatter. In the following, only one experimental curve is shown for each test condition; it corresponds to the experimental curve being the curve closest to the "average" response.

Crack growth resistance was investigated using compact tension (CT) and Single Edge Notch Bend (SENB) specimens according to ASTM-1820. CT specimens have a total thickness $B = 12.5$ mm and a width $W = 2B = 25$ mm. SENB specimens have a total thickness $B = 12.5$ mm and

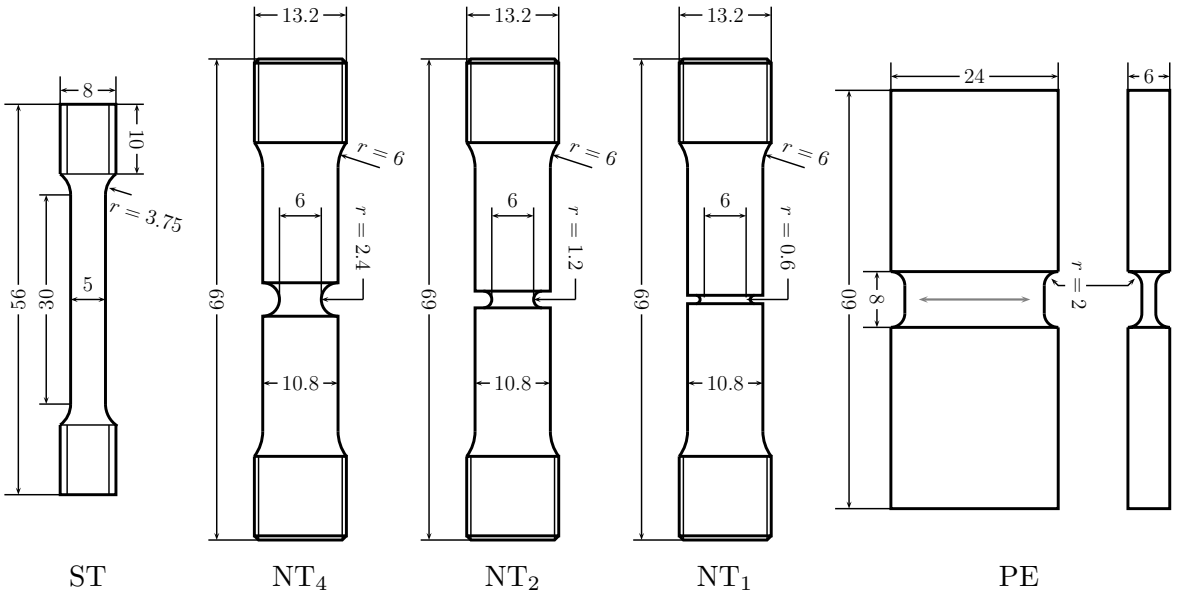

Figure V.2 : Samples for mechanical testing (dimensions in mm): smooth tensile bars (ST), notched tensile bars with different notch radii (NT_4, NT_2 and NT_1) and plane strain specimens (PE). The gray arrow indicates the plane strain direction. PE conditions are met at the centre of the specimen .

a width $W = 2B = 25$ mm ; the span is $S = 4W = 100$ mm. Specimens were fatigue-precracked in order to obtain an initial crack length a_0 between to 0.55 and $0.60W$ for CT and close to $0.5W$ for SENB specimens. Specimens do not have side grooves. The J—Δa resistance curve was determined using the multi-specimen technique in accordance with ASTM-1820. The plastic work (A_{pl}) was computed using the load line displacement. The corresponding J integral was computed as:

$$J = J_p + J_e = \frac{\eta A_{\text{pl}}}{B(W - a_0)} + J_e \tag{V.1}$$

where J_e is the elastic part of the J integral. All quantities (in particular η and J_e) were computed for the initial crack length. In the present case $J_e \ll J_p$ as the material is very ductile. Ductile crack extension was determined from direct measurements of crack advance of specimens which were broken at liquid nitrogen temperature after unloading. To investigate fracture anisotropy two loading configurations were studied: L–T and T–L. For the L–T (resp. T–L) configuration, load is applied in the L (resp. T) direction and crack extends in the T (resp. L) direction.

In the following F denotes the applied force, S_0 the initial minimum cross section, Φ_0 the initial diameter of the minimum cross section, $\Delta\Phi_{\text{S}}$ the diameter reduction along the S direction, L_0 the initial gauge length (tensile specimens), ΔL the gauge length increase, e_0 the initial specimen thickness (plane strain specimens) and Δe the thickness reduction.

V.3 Results

V.3.1 Anisotropic plastic behavior

Fig. V.3-a shows the nominal stress (F/S_0) as a function of the nominal strain ($\Delta L/L_0$) for different loading directions for smooth tensile bar tests. Flow stress depends on the loading direction: it is the highest for loading along the T direction and the lowest for loading along the D direction.

It is noticeable that the yield stress along the T direction corresponding to grade X100 (dashed line on Fig. V.3-a) is only reached after 2% deformation. In practice, this is achieved during pipe forming [Shinohara et al. 2010, Herynk et al. 2007]. Similar results are obtained in the case of plane strain specimens as shown on Fig. V.3-b where the nominal stress is plotted as a function of the thickness reduction ($\Delta e/e_0$). In that case, the flow stress along the T direction is higher than along the L direction.

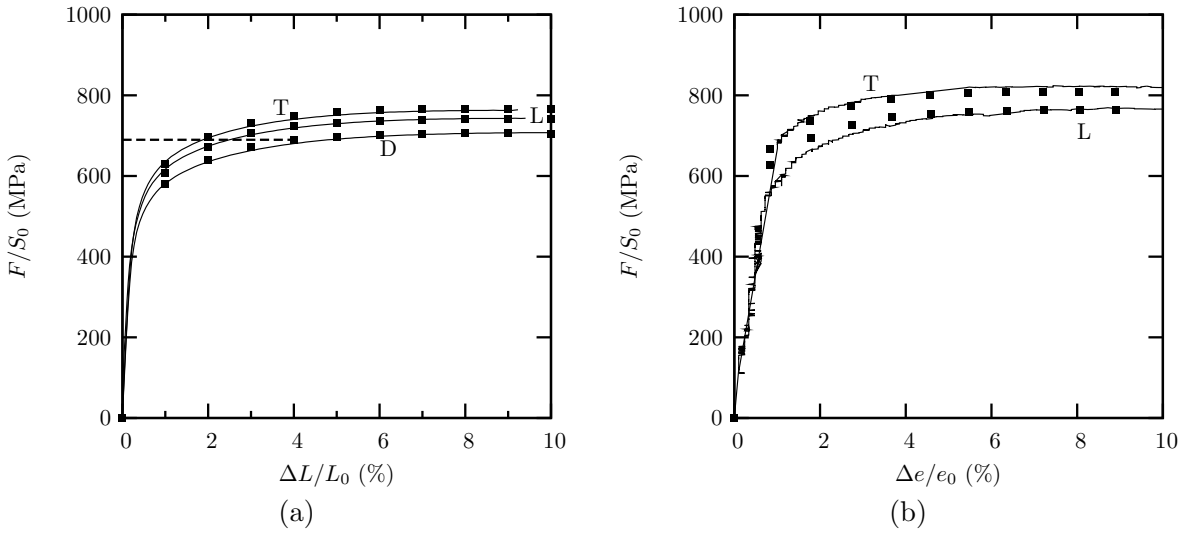

Figure V.3 : (a) Tensile tests: nominal stress–nominal strain curves for T, L and D directions. The dashed lines indicate the yield stress required for grade X100 along the T direction. (b) Plane strain tests : nominal stress–nominal thickness strain for T and L directions. Symbols (■) show the results of the elasto-plastic (i.e. without considering damage) simulations using the model presented in section V.4.1.

Plastic flow behavior also depends on the loading direction as shown in Fig. V.4-a where the diameter reduction along the S direction, $\Delta\Phi_S/\Phi_0$, is plotted as a function of the elongation $\Delta L/L_0$. In L and T loading, plastic anisotropy is obvious. Deformation along the S direction is larger than in the isotropic case so that initially round cross sections deform into ellipses (see e.g. [Tanguy et al. 2008]). On the other hand, D loading leads to an "isotropic" diameter reduction. These observations are also well corroborated by the examination of the fracture surfaces (see Fig. V.4-b) which have an elliptical shape, with a higher deformation along the S direction, in the case of L and T loading whereas they remain circular in the case of D loading.

V.3.2 Anisotropic ductility

The area reduction at failure Z is plotted for the different specimen types on Fig. V.5 for L and T loading indicating that in all cases ductility is slightly lower for T loading. As expected, ductility decreases with specimen severity (see [Mackenzie et al. 1977] and [Tanguy et al. 2008] on a similar material).

Fig. V.6 shows the experimental force—diameter reduction curves for notched bars tested in T and L directions. Curves present a sharp load drop which corresponds to the initiation of a macroscopic crack at the centre of the specimens. For a given specimen type, load is higher in the case of T loading due to plastic anisotropy. The sharp load drop occurs for lower diameter reductions ($\Delta\Phi_S/\Phi_0$) for these specimens ; this indicates a lower ductility along the T direction in agreement with results regarding the area reduction at failure (Fig. V.5).

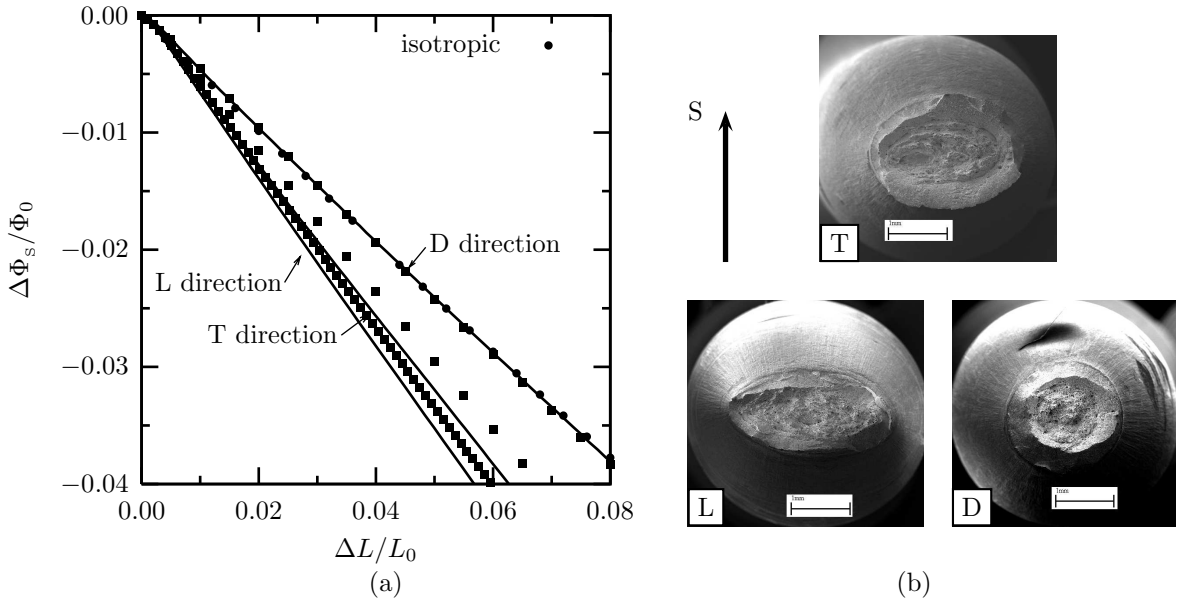

Figure V.4 : (a) Diameter reduction along the S direction as a function of elongation for L,T and D loading directions. The isotropic case (dots) corresponds to the equation: $\Delta\Phi_S/\Phi_0 = (1 + \Delta L/L_0)^{-\frac{1}{2}} - 1$. (b) Macroscopic fracture surfaces of ST specimens loaded along the different directions. The arrow indicates the S direction. Symbols (■) show the results of the elasto-plastic (i.e. without considering damage) simulations using the model presented in section V.4.1.

V.3.3 Anisotropic crack growth resistance

Fig. V.7 shows the crack extension resistance curves (J—Δa) for CT (Fig. V.7-a) and SENB (Fig. V.7-b) specimens tested under both T–L and L–T configurations. In the case of CT specimens, it is observed that crack growth resistance is higher in the case of L–T loading compared to T–L loading. This is also the case for SENB specimens. J values for SENB specimens are slightly higher that for CT specimens.

V.3.4 Fractographic examination

Fracture surfaces were examined using scanning electron microscopy (SEM). Fig. V.8 shows SEM photographs for the fracture surface of NT_1 specimens tested along the L and T directions. Photographs were taken at the center of the specimens where ductile cracks were initiated. Fracture surfaces mainly consist of relatively large primary dimples. Smaller dimples can also be seen; their amount increases as the notch severity (and consequently the stress triaxiality ratio) is decreased as already observed in [Tanguy et al. 2008]. Smaller dimples are initiated on iron carbides (Fe_3C). No significant difference could be found between both fracture surfaces. Similar conclusions were drawn from the examination of CT and SENB specimens.

Fig. V.9 shows the fracture surface of a preloaded NT_1 specimen which was subsequently broken in liquid nitrogen to prevent any further plastic deformation. The fracture surface exhibits numerous dimples in which spherical inclusions (mainly CaS or TiO_2) acting as void nucleation sites can be found. The volume fraction of inclusions was measured using image analysis and is equal to $2.\,10^{-4}$.

The present SEM investigation of the fracture surfaces did not evidence any clear origin for the anisotropic fracture behaviour. Polished cross sections were also examined to characterize inclusion/cavity spacing along different direction as anisotropic spacing may lead to anisotropic void

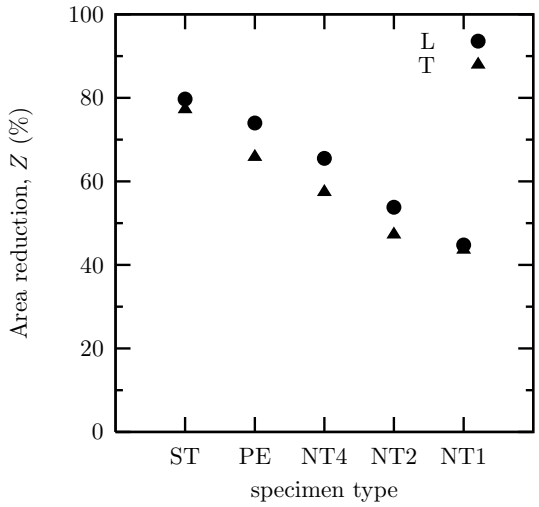

Figure V.5 : Area reduction at failure for the various specimen types for the different loading directions.

coalescence and consequently to anisotropic rupture properties [Thomason 1985a;b, Pardoen and Hutchinson 2003]. Examinations could not clearly evidence spacing anisotropic ; this could be due to the very low inclusion content which makes measurements difficult.

V.4 Model for anisotropic plasticity and ductile damage

V.4.1 Anisotropic plasticity

Due to the high plastic anisotropy of the material under investigation an appropriate model must be used to evaluate strains and stresses leading to fracture of tested specimens. The model used in this study to describe plastic anisotropy was initially developed by Bron and Besson [2004]. It is a generalization of previously published models [Karafillis and Boyce 1993, Barlat et al. 1991]. The model is briefly recalled here.

An anisotropic scalar stress measure, σ_E, is defined as a weighted average of N anisotropic scalar stress measures σ_{Ei}:

$$\sigma_E = \left(\sum_{k=1}^{N} \alpha_k \sigma_{Ek}^a \right)^{1/a} \tag{V.2}$$

with $\sum_k \alpha_k = 1$ and $\alpha_k \geq 0$, $\forall k$. In the following, two anisotropic scalar stress measures ($N = 2$) are used to define σ_E as in [Bron and Besson 2004, Tanguy et al. 2008]. One first defines two modified stress deviators:

$$\underline{s}_k = \underline{\underline{L}}_k : \underline{\sigma} \tag{V.3}$$

where the fourth order tensor $\underline{\underline{L}}_k$ is expressed using Voigt notations as:

$$\underline{\underline{L}}_k = \begin{pmatrix} \frac{1}{3}(c^k_{\mathrm{LL}} + c^k_{\mathrm{SS}}) & -\frac{1}{3}c^k_{\mathrm{SS}} & -\frac{1}{3}c^k_{\mathrm{LL}} & 0 & 0 & 0 \\ -\frac{1}{3}c^k_{\mathrm{SS}} & \frac{1}{3}(c^k_{\mathrm{SS}} + c^k_{\mathrm{TT}}) & -\frac{1}{3}c^k_{\mathrm{TT}} & 0 & 0 & 0 \\ -\frac{1}{3}c^k_{\mathrm{LL}} & -\frac{1}{3}c^k_{\mathrm{TT}} & \frac{1}{3}(c^k_{\mathrm{TT}} + c^k_{\mathrm{LL}}) & 0 & 0 & 0 \\ 0 & 0 & 0 & c^k_{\mathrm{TL}} & 0 & 0 \\ 0 & 0 & 0 & 0 & c^k_{\mathrm{LS}} & 0 \\ 0 & 0 & 0 & 0 & 0 & c^k_{\mathrm{ST}} \end{pmatrix} \tag{V.4}$$

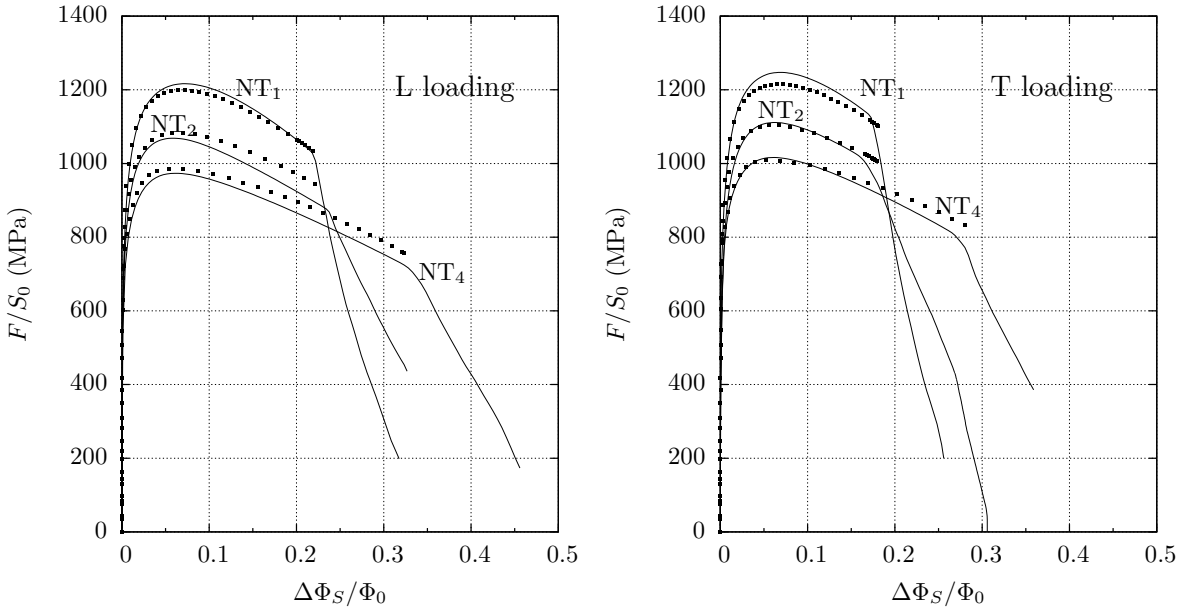

Figure V.6 : Comparison of experimental force—diameter reduction curves for notched specimens tested in the L and T directions. Symbols (■) show the results of the elasto-plastic (i.e. without considering damage) simulations using the model presented in section V.4.1.

The eigenvalues of $\underline{s}_k$ are then computed: $S_k^1 \geq S_k^2 \geq S_k^3$. σ_{E1} is then computed as:

$$\sigma_{E1} = \left(\frac{1}{2} \left(|S_1^2 - S_1^3|^{b_1} + |S_1^3 - S_1^1|^{b_1} + |S_1^1 - S_1^2|^{b_1} \right) \right)^{1/b_1} \tag{V.5}$$

and σ_{E2} as:

$$\sigma_{E2} = \left(\frac{3^{b_2}}{2^{b_2}+2} \left(|S_2^1|^{b_2} + |S_2^2|^{b_2} + |S_2^3|^{b_2} \right) \right)^{1/b_2} \tag{V.6}$$

The yield surface is finally expressed as

$$\phi = \sigma_E - R(p) \tag{V.7}$$

where $R(p)$ represents the flow stress expressed as a function of the effective cumulated plastic strain p. In this work it is expressed as:

$$R(p) = R_0 \left(1 + q_1(1 - \exp(-k_1 p)) + q_2(1 - \exp(-k_2 p))\right) \tag{V.8}$$

The plastic strain rate tensor, $\underline{\dot{\varepsilon}}_p$, is obtained assuming the normality rule so that: $\underline{\dot{\varepsilon}}_p = \dot{p}\partial\phi/\partial\sigma$. p is such that: $\underline{\dot{\varepsilon}}_p : \sigma = \dot{p}\sigma_E$. Considering that the material is slightly strain rate dependent, $\dot{p}$ is expressed using a simple Norton flow rule as:

$$\dot{p} = \dot{\varepsilon}_0 \left(\phi/\sigma_0\right)^n \tag{V.9}$$

Model parameters that need to be adjusted are therefore α_1 ($\alpha_2 = 1 - \alpha_1$), c_k^i ($k = 1, 2$ and $i = \mathrm{TT} \ldots \mathrm{ST}$), a, b_1 and b_2. In the following the model was simplified assuming $a = b_1 = b_2$. The parameter adjustment is carried out according to previous work [Bron and Besson 2004]. A cost function representing the difference between experimental results and simulations is constructed and minimized with respect to the model parameters. Tensile tests along L, T and D directions as

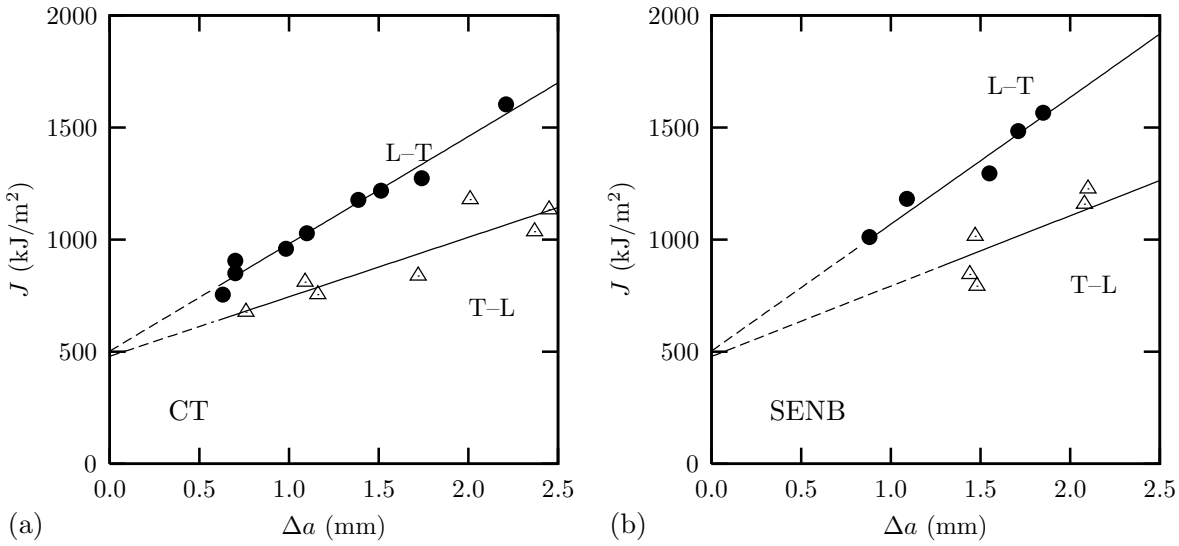

Figure V.7 : J—Δa resistance curves for CT (a) and SENB (b) specimens for L–T and T–L loading configurations (symbols: experiments, lines: trend).

well as all tests on notched bars with different minimum radii are considered when building the cost function. In the case of tensile smooth bars, force-axial displacement curves are used together with the relationship between axial and diameter displacement. In the case of notched bars, force-diameter reduction curves are used. In both cases, diameter displacement is measured along S direction. The large number fitting parameters allows to obtain a good fit in all cases. Comparisons of simulated results (assuming no damage) are shown in Figs. V.3, V.4 and V.6 where simulations are indicated by symbols (■). Adjusted material model parameters are shown in Tab. V.2.

V.4.2 Ductile damage

In addition to plastic anisotropy, the model to be developed to represent the material behavior must account for ductile damage and rupture anisotropy. The model proposed by Morgeneyer et al. [2009] is derived from the well accepted Gurson-Tvergaard-Needleman (GTN) model [Tvergaard and

Table V.2 : Material model parameters: anisotropic elasto-plastic behaviour.

Elastic properties	E	210 GPa
	ν	0.3
Plastic hardening	R_0, q_1, k_1	465 MPa, 0.42, 62.
	q_2, k_2	0.78, 2.05
Anisotropic model	a, α	8.84, 0.71
	c_1^{TT}, c_1^{LL}, c_1^{SS}	0.945, 0.984, 0.872
	c_1^{TL}, c_1^{LS}, c_1^{ST}	0.967, 1.148, 1.147
	c_2^{TT}, c_2^{LL}, c_2^{SS}	1.638, 0.428, 0.207
	c_2^{TL}, c_2^{LS}, c_2^{ST}	0.935, 1.053, 1.417
Strain rate effect	$\dot{\varepsilon}_0$, σ_0, n	1s^{-1}, 55 MPa, 5

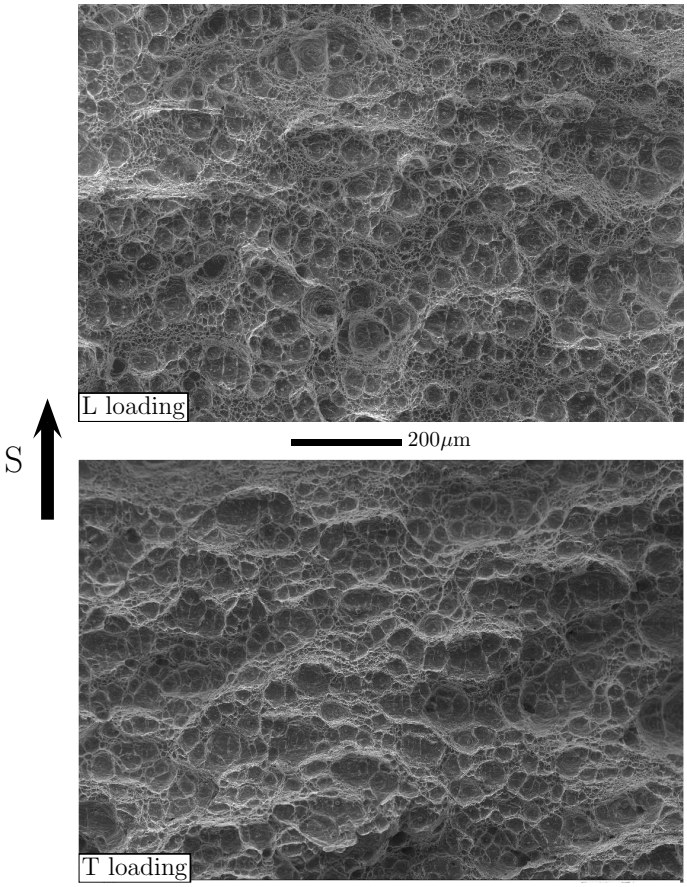

Figure V.8 : Example of fracture surface observed at the center of NT_1 specimens tested along L and T directions.

Needleman 1984, Needleman 1990] which is reformulated as in [Besson et al. 2001, Besson 2010] to introduce an effective scalar stress measure, σ_*, function of both ductile damage and the macroscopic stress tensor $\underline{\sigma}$. Damage is represented by one single variable, f, corresponding to the void volume fraction or porosity. The effective stress σ_* is implicitly defined by the following equation:

$$\frac{\sigma_E^2}{\sigma_*^2} + 2q_1 f_* \cosh\left(\frac{1}{2}\frac{\sigma_K}{\sigma_*}\right) - 1 - q_1^2 f_*^2 = 0 \tag{V.10}$$

Plastic anisotropy is introduced using an anisotropic stress measure σ_E defined above (eq. V.2) instead of the von Mises stress as in the original model. This solution has already been used by different authors [Bron and Besson 2006, Tanguy et al. 2008, Morgeneyer et al. 2009].

Models have been proposed to explain anisotropic rupture properties based on the existence of anisotropic cavities. They are based on the initial developments by Gologanu, Leblond and Devaux for prolate and oblate cavities [Gologanu et al. 1993; 1994, Pardoen and Hutchinson 2000; 2003]. As cavities are assumed to be axisymmetric, the model needs to be adapted in order to be applied to actual cases where the stress state is such that cavities do not remain axisymmetric [Benzerga et al. 1999; 2004b]. This class of model was recently extended to the case of an anisotropic matrix (Hill model) [Monchiet et al. 2006; 2008, Keralavarma and Benzerga 2008] but cavities are still assumed to be axisymmetric. Following the work by Thomason [Thomason 1968; 1985b, Benzerga et al. 1999, Pardoen and Hutchinson 2000, Gologanu et al. 2001], anisotropic ductile failure may also be attributed to anisotropic coalescence caused by different void mean spacing along the three material directions. This analysis of coalescence is usually coupled with the above mentioned models

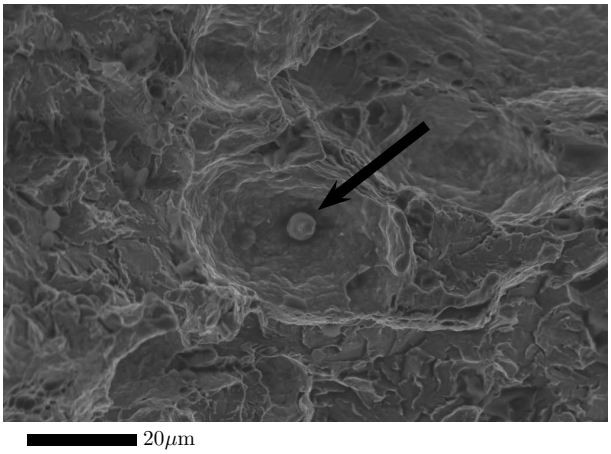

Figure V.9 : Spherical CaS inclusion (arrow) found at the origin of large primary dimples.

for anisotropic void growth. Models accounting for void shape and void orientation change have also been proposed in the context of variational estimates [Kailasam et al. 2000, Danas and Ponte-Castaneda 2009a;b].

Microstructural examinations of the investigated material could not evidence any initial microstructure isotropy possibly related to rupture anisotropy such as initial inclusion/void shape or mean spacing. Rupture anisotropy is introduced in the model replacing the trace of the stress tensor, σ_{kk}, by a weighted average, σ_K, of the stresses along the sheet principal directions [Morgeneyer et al. 2009]:

$$\sigma_K = \alpha_{\mathrm{T}}\sigma_{\mathrm{TT}} + \alpha_{\mathrm{L}}\sigma_{\mathrm{LL}} + \alpha_{\mathrm{S}}\sigma_{\mathrm{SS}} \tag{V.11}$$

where $\alpha_{\mathrm{T,\,L,\,S}}$ are parameters that need to be adjusted. This formulation is inspired from the above mentioned models for anisotropic void growth which introduce a weighted average of the stresses along the material principal directions similar to eq. V.11 with two of the weighting factors being equal due to void symmetry. This modelling strategy is indeed phenomenological but fully 3D whereas micromechanically based model presented above are limited to 2D cases. Its numerical implementation is straightforward so that the model could be an attractive alternative to the more complex models described above.

Void coalescence and material point failure is represented using the f_* function introduced in [Tvergaard and Needleman 1984]. It is expressed as:

$$f_* = \begin{cases} f & \text{if } f \leq f_c \\ f_c + \delta(f - f_c) & \text{otherwise} \end{cases} \tag{V.12}$$

where f_c represents the critical porosity for which coalescence starts. δ is an "accelerating" factor which represents the increased softening effect of pores once coalescence has started. In the following fixed values will be used with $f_c = 0.05$ and $\delta = 4.5$. As f_c is much larger than the initial porosity f_0, it has a small influence on the computed ductility and crack growth resistance. The value of δ was taken similar to the value used in [Tanguy et al. 2008].

The model is further developed writing the plastic yielding condition as [Besson 2010]:

$$\phi = \sigma_* - R(p) \geq 0 \tag{V.13}$$

where R represents isotropic work hardening of the undamaged material. p is a measure of plastic strain within the matrix material. Plastic flow is given by the normality rule as:

$$\dot{\underline{\varepsilon}}_p = (1-f)\dot{p}\frac{\partial \phi}{\partial \underline{\sigma}} = (1-f)\dot{p}\frac{\partial \sigma_*}{\partial \underline{\sigma}} \tag{V.14}$$

where $\underline{\dot{\varepsilon}}_p$ is the plastic strain rate tensor. As $\sigma_*$is a homogeneous function of degree one of $\underline{\sigma}$ one gets: $\underline{\dot{\varepsilon}}_p : \underline{\sigma} = (1-f)\dot{p}\sigma_*$ which expresses the equivalence of the macroscopic and the microscopic plastic dissipations. $\dot{p}$ is still expressed using eq. V.9.

Evolution of damage (porosity) is controlled by void growth only, so that

$$\dot{f} = (1-f)\text{trace}\,(\underline{\dot{\varepsilon}}_p) \tag{V.15}$$

An additional term corresponding to void nucleation [Chu and Needleman 1980] was not used in this study based on the fractographic examination which showed very limited secondary void nucleation on iron carbides at least for specimens in which a high stress triaxiality prevails.

V.4.3 Simulation techniques

The proposed model was implemented in a general purpose object oriented finite element software [Besson and Foerch 1997, Foerch et al. 1997]. Ductile rupture is always accompanied by large deformations so that a finite-strain formalism must be used when implementing constitutive equations. This was done using a generic formulation based on a reference frame which facilitates keeping the standard small strain formulation and using an additive strain rate decomposition (i.e. $\underline{\dot{\varepsilon}} = \underline{\dot{\varepsilon}}_e + \underline{\dot{\varepsilon}}_p$ where $\underline{\dot{\varepsilon}}$ is the strain rate tensor and $\underline{\dot{\varepsilon}}_e$ the elastic strain rate tensor) [Sidoroff and Dogui 2001]. In all cases, 20 nodes bricks with reduced integration (8 Gauss points) were used to perform the finite element (FE) simulations. Usual symmetry conditions were used so that $1/8$ of NT specimens and $1/4$ of CT and SENB specimens were meshed as exemplified on Fig. V.13 and Fig. V.14. The material is considered as broken when f_* reaches $1/q_1 - \epsilon$ with $\epsilon = 10^{-3}$. In that case, the material behaviour is replaced by an elastic behaviour with a very low stiffness (Young modulus: $E_b = 1$ MPa). When the material is considered as broken at four Gauss points within an element, the element is removed from the calculation. To avoid getting a singular global stiffness matrix, displacement increments of nodes belonging only to removed elements are then prescribed to 0.

V.5 Unit cell calculations

V.5.1 Calculations

Since the pioneering work by Koplik and Needleman [Koplik and Needleman 1988] unit cell calculations have being used to numerically study void growth in porous solids. This versatile methodology allows to easily study the effect of various parameters on void growth and coalescence such as hardening rate [Faleskog et al. 1998, Gao et al. 1998, Lecarme et al. 2011], void shape or cell shape [Pardoen and Hutchinson 2000], void population [Faleskog and Shih 1997, Fabrègue and Pardoen 2008], void distribution [Bandstra and Koss 2008], second phase particles [Steglich and Brocks 1997, Steglich et al. 1999]. Effect of plastic anisotropy was recently studied in the case of single crystals [Yerra et al. 2010, Yu et al. 2010] and for anisotropic plasticity [Steglich et al. 2010, Keralavarma et al. 2011].

In this study the effect of plastic anisotropy on void growth is studied using the above described model (section V.4.1). The finite element mesh used for the calculations is shown in Fig. V.10-(a). The cell is a 3D cube containing a central spherical void. The cell initial porosity corresponds to the inclusion volume fraction of the material, i.e. $f_0 = 2.10^{-4}$. Due to symmetry condition only $1/8$ of the cell is meshed. Corresponding boundary conditions on displacements are imposed. Periodic boundary conditions are imposed by keeping constant the normals to outer surfaces. The cell is submitted to an axisymmetric macroscopic stress state (see Fig. V.10-(b)) such that the macroscopic

stress tensor, $\underline{\Sigma}$, is expressed as:

$$\underline{\Sigma} = \begin{pmatrix} \Sigma_{11} & 0 & 0 \\ 0 & \Sigma_{22} & 0 \\ 0 & 0 & \Sigma_{33} = \Sigma_{22} \end{pmatrix} \tag{V.16}$$

It is assumed that $\Sigma_{11} > \Sigma_{22} = \Sigma_{33}$. The ratio $\Sigma_{22}/\Sigma_{11} = \eta$ is kept constant in order to maintain a constant stress triaxiality ratio, τ, with $\tau = \frac{1}{3}(1+2\eta)/(1-\eta)$ The principal loading direction (i.e. loading direction 1) corresponds to one of the three material directions (L, T or S). In the following the unit cell calculations will be used to calibrate the model for ductile failure. The material is considered as rate independent so that the Riks method could be used in order to keep the stress ratio constant during the loading history,

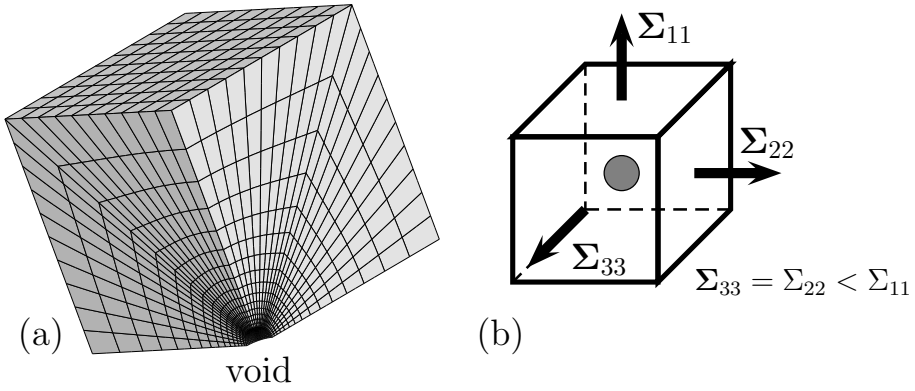

Figure V.10 : Unit cell calculation: (a) finite element mesh ($f_0 = 2.\,10^{-4}$), (b) boundary conditions.

V.5.2 Results

Results of unit cell calculations are shown on Fig. V.11 for stress triaxiality between 1.0 and 2.5. Lower triaxialities were not investigated as large void elongation is obtained for these conditions and as values reached in NT, CT and SENB tests are higher than 1.0. The relative porosity increase f/f_0 is plotted as a function of the cell elongation $\Delta l/l_0$ (where l_0 represents the initial cell height). As expected increasing the stress triaxiality leads to faster void growth. For each triaxiality level, it can be noticed that void growth is the highest for T loading and the lowest for S loading.

The model for ductile rupture presented above (section V.4.2) was fitted to reproduce the porosity increase obtained using the unit cell simulations. Parameters to be fitted are q_1, $\alpha_{\rm T}$, $\alpha_{\rm L}$ and $\alpha_{\rm S}$. A very good agreement (see Fig. V.11) was obtained with $q_1 = 2.39$ and $\alpha_{\rm T} = \alpha_{\rm L} = \alpha_{\rm S} = 0.896$. This result is in agreement with unit cell calculations reported in [Steglich et al. 2010]. It shows that void growth can still be considered as "isotropic" (as the weighting parameters $\alpha_{\rm T}$, $\alpha_{\rm L}$ and $\alpha_{\rm S}$ are equal) but that it is governed by the ratio $\frac{1}{3}\sigma_{kk}/\sigma_E$ and not by the standard stress triaxiality ratio $\frac{1}{3}\sigma_{kk}/\sigma_{\rm eq}$ where $\sigma_{\rm eq}$ is the von Mises stress. The void growth anisotropy exhibited in Fig. V.11 is only apparent and due to the fact that growth rate are compared for a fixed stress triaxiality and not for a fixed $\frac{1}{3}\sigma_{kk}/\sigma_E$ ratio.

V.5.3 Simulation of tests on NT and CT specimens

The various test on NT specimens were simulated using the above fitted parameters. Results are shown on Fig. V.12-a. The predicted ductility anisotropy is very small and does not correspond to the experimentally observed one although predicted ductilities are realistic (i.e. neither too large nor too

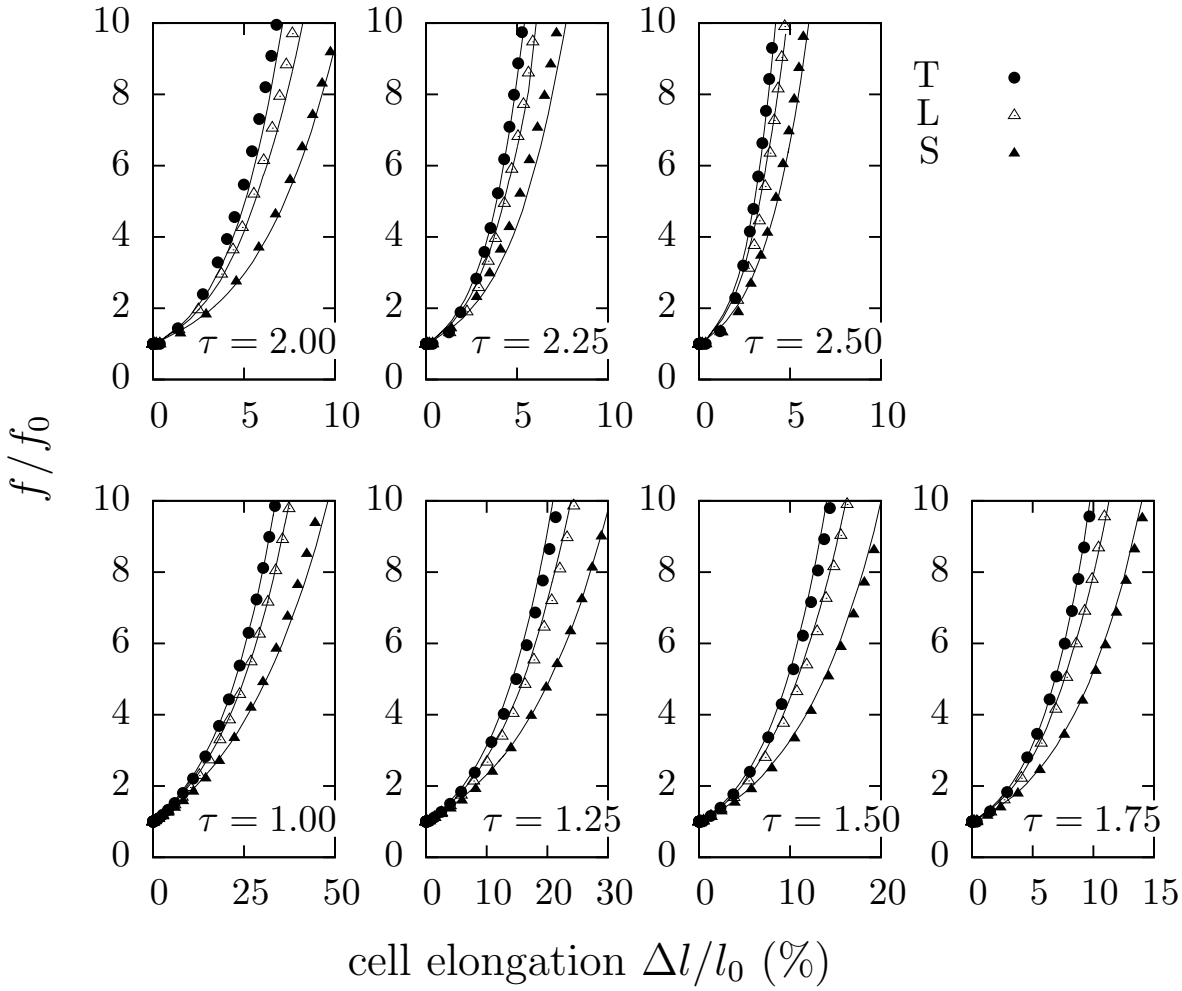

Figure V.11 : Unit cell calculation: results for axisymmetric loading for various values of the stress triaxiality ratio τ. Symbols show results of FE calculations and lines show model prediction.

small). In particular the model predicts that ductilities obtained on NT_2 and NT_1 specimens are very close. Predictions are close to experiments for specimens loaded along the L direction.

Simulation of J—Δa curves for CT specimens is shown on Fig. V.12-b. Details of the simulation technique are given in V.6.2. As in the case of NT specimens, anisotropy is not predicted but predictions for L loading are close to the experiments. Simulated J values for T–L loading are slightly higher than for L–T loading due to the higher flow stress along the T direction.

The results also show that ductility anisotropy cannot be attributed to plastic anisotropy. Voids are initially spherical and stress triaxiality in tested specimens is high enough so that cavities remain close to spheres. Microstructural examination of the material did not reveal an anisotropic inclusion distribution which could explain anisotropic rupture properties (note that as the inclusion volume content is very low, it is however possible that an anisotropic distribution could not be detected).

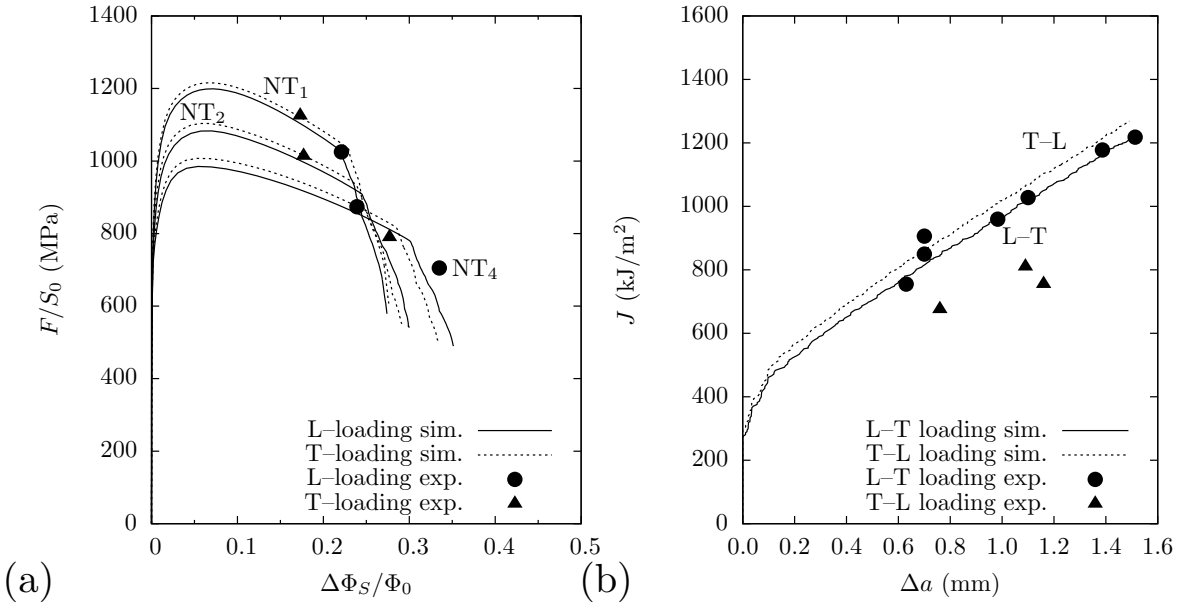

Figure V.12 : Simulation of (a) NT specimens and (b) CT specimens using damage model parameters fitted on the unit cell calculations.

Table V.3 : Material model parameters: damage behavior.

f_0	$2.\,10^{-4}$
q_1	1.80
$\alpha_{\rm T}$, $\alpha_{\rm L}$, $\alpha_{\rm S}$,	1.31, 0.60, 1.23
f_c, δ	0.05, 4.5
$h_\perp$	200 μm

V.6 FE Simulations of experiments

V.6.1 Model parameters fitting on NT specimens

As model parameters for damage (i.e. q_1, $\alpha_{\rm T}$, $\alpha_{\rm L}$ and $\alpha_{\rm S}$) could not be derived from the unit cell calculations, they were directly fitted using experiments on NT specimens. Parameters were fitted to match crack initiation (i.e. sharp load drop). A higher weight was given to NT$_1$ and NT$_2$ specimens as they have higher stress triaxiality levels which are closer to levels met in cracked specimens (CT and SENB). Results are show on Fig. V.13 and exhibit a good agreement except in the case of NT$_4$ specimens tested along the T direction. Optimized parameters are shown on Tab. V.3. Very different values are obtained for the $\alpha_{\rm T,L,S}$ coefficients which are between 0.60 (L direction) and 1.31 (T direction). The high value for the T direction corresponds to the lower ductility observed for this direction.

V.6.2 Simulation of CT and SENB tests

Adjusted model parameters were used to simulate both CT and SENB tests. Due to the softening character of the constitutive equations it is necessary to use a fixed mesh size in areas where cracks propagate in order to control the fracture energy [Rousselier 1987, Ruggieri et al. 1996, Gullerud

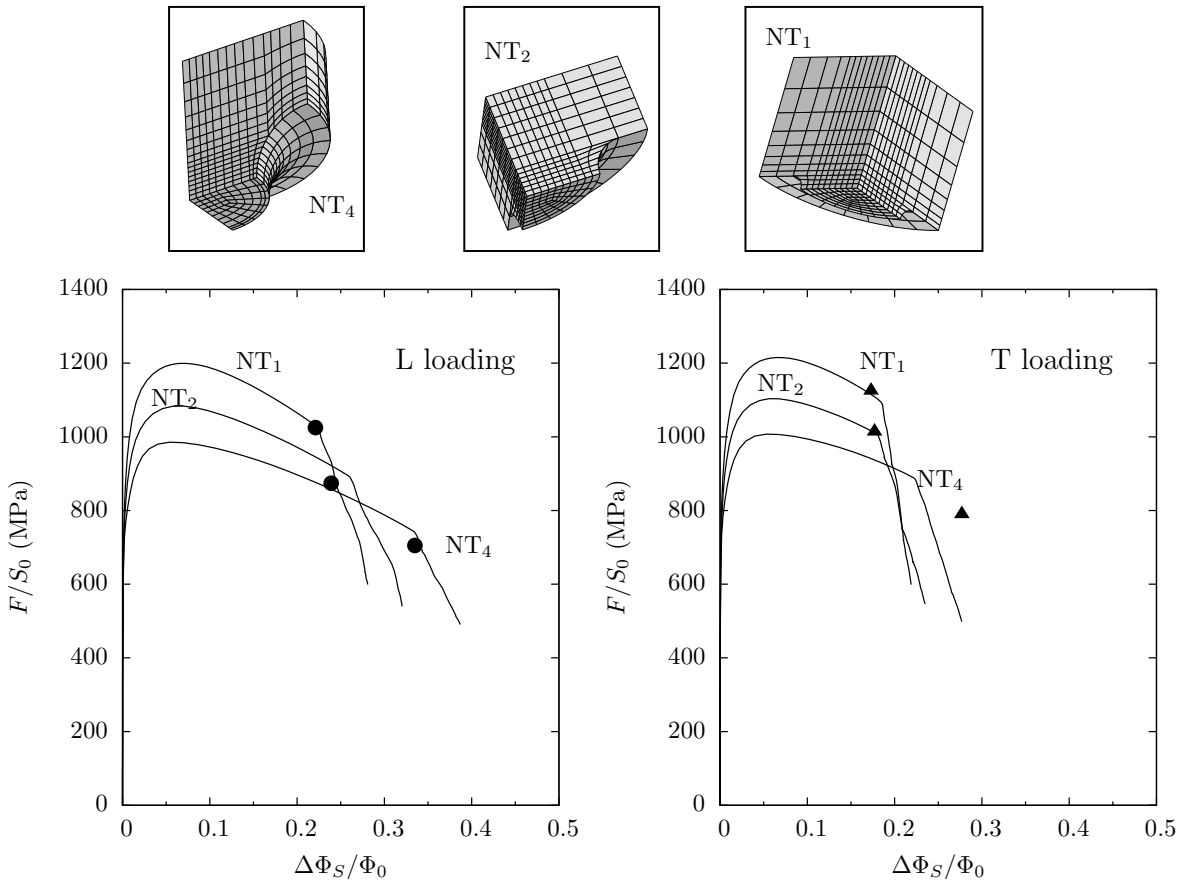

Figure V.13 : Simulation of the NT specimens using damage model parameters optimized on experimental results (lines). Symbols represent the experimental sharp load drop which corresponds to crack initiation. FE meshes for NT specimens are also shown.

et al. 2000]. The important mesh dimension is the height of the element along the direction normal to the crack propagation plane, $h_\perp$ [Siegmund and Brocks 1999]. It is fixed to 200μm. A possibly better solution is based on "non local" damage models which allow to avoid mesh dependent damage localization. These models are still under development for ductile materials [Mediavilla et al. 2006, Feld-Payet S. 2011].

CT and SENB specimens were simulated using the above described constitutive equations. In order to evaluate the J—Δa curves, simulations were considered as "numerical" experiments and analysed following the ASTM-1820 standard. For that purpose a specific post-processing tool was developed to compute the average crack advance. The J value can directly be obtained from the load—displacement curve using eq. V.1. Meshes are shown on Fig. V.14-a. The SENB specimens are supported by cylinders having a 18 mm diameter. The friction coefficient is taken equal to 0.1. In order to simplify the simulations, displacement was prescribed on two rows of nodes instead of representing the central support.

Experimental J—Δa curves are compared with simulations on Fig. V.15 for both CT and SENB specimens showing very good agreement. This indicates that rupture anisotropy observed on NT specimens and cracked specimens has the same origin.

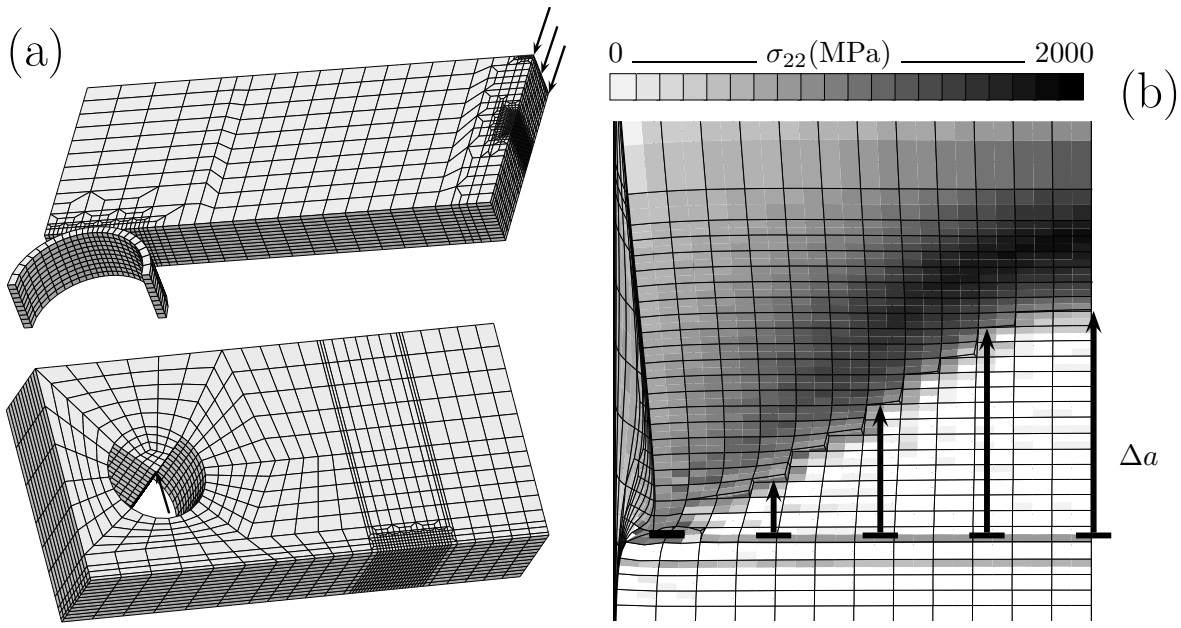

Figure V.14 : (a) 3D meshes of SENB and CT specimens (arrows indicate non zero prescribed displacements), (b) opening stress field and crack advance in a CT specimen (broken elements are removed).

V.7 Conclusions

A grade X100 plate used to manufacture line pipes was experimentally studied in this work. It was shown the plastic behavior is anisotropic and that it can be described using the model proposed by Bron and Besson [2004]. Rupture properties are also anisotropic in terms of both ductility (tensile bars) and crack growth resistance (CT and SENB tests).

Fractographic examination of broken specimens did not allow to identify the origin of rupture anisotropy. CaS/TiO particles at the origin of ductile damage (see Fig. V.9) are spherical so that initial void shape anisotropy cannot explain rupture anisotropy. Another origin of rupture anisotropy could be related to an anisotropic inclusion/cavity spacing leading to anisotropic void coalescence following the internal necking mechanism described by Thomason [1985a;b] (see also [Pardoen and Hutchinson 2003]). However examinations of polished cross sections could not evidence anisotropic spacing. Note that this could be due to the very low inclusion content which makes measurements difficult. In addition observation of fracture surfaces (see Fig. V.8) does not evidence anisotropic coalescence.

In absence of a clear origin for rupture anisotropy, a simple semi-phenomenological modification of the Gurson model (section V.4.2) was proposed which allows to describe both plastic anisotropy and rupture anisotropy.

Unit cell calculations were carried out in order to study the role of the main loading direction on void growth rate as this could also be an explanation for rupture anisotropy. For a constant stress triaxiality ratio ($\frac{1}{3}\sigma_{kk}/\sigma_{\rm eq}$), void growth rate depends on the main loading direction. However fitting the proposed damage model on the unit cell calculations shows that void growth rate should be expressed as a function of $\frac{1}{3}\sigma_{kk}/\sigma_E$ and not of $\frac{1}{3}\sigma_{kk}/\sigma_{\rm eq}$. In that case, void growth can be considered as "isotropic". This result is consistent with the theoretical derivations of Benzerga and Besson [2001] in the case of a matrix material obeying a Hill criterion. As a consequence the Gurson–like model tuned on the unit cell calculations is unable to reproduce fracture anisotropy (Fig. V.12) which is

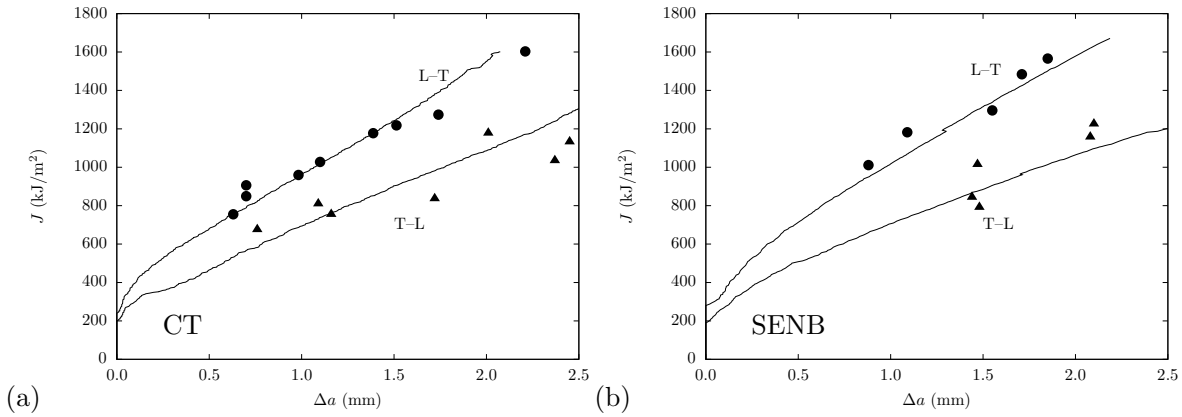

Figure V.15 : Simulation of the J—Δa curves for CT (a) and SENB (b) specimens (lines) and comparison with experimental results (symbols).

strongly underestimated.

The anisotropic rupture behavior could however be represented using the same semi-phenomenological modification of the Gurson model which was then tuned on experiments on notched bars. Using the tuned parameters it became possible to simulate crack extension in both CT and SENB pre-cracked specimens.

Chapter -VI-

Simulation of the effect of prestrain on ductility and toughness

Contents

Résumé en français :

Le chapitre 6 reprend les simulations du chapitre 4 démontrant l'effet de pré-déformation avec cette fois l'application du modèle « complet » présenté au chapitre 5 (plasticité anisotrope et endommagement anisotrope). La modèle d'écrouissage tient compte uniquement de la partie isotrope ; la partie cinématique étant difficile à ajuster avec les essais réalisés, elle a été négligée.

Le matériau a été pré-étiré selon la direction T simulant ainsi l'effet de pré-déformation selon les différents niveaux introduits expérimentalement (2, 4 et 6 $\%$). Les essais de traction entaillées NT et les essais CT ont ensuite été simulés selon les différents niveaux de pré-chargement (0, 2, 4 et 6 $\%$).

Le modèle permet alors de reproduire la baisse de ductilité ($E_c = \Delta\Phi_S|_c / \Phi_0$) des éprouvettes NT avec la pré-déformation. La baisse de ténacité en fonction de la pré-déformation est également reproduite pour les deux configurations L-T et T-L. La simulation montre que seul le pré-écrouissage joue et non l'accumulation d'endommagement durant la phase de pré-chargement. Des calculs sont également réalisés pour des niveaux de pré-déformation allant jusqu'à 30 $\%$ (non possible expérimentalement du fait de la striction). Ils mettent évidence une réduction de la ténacité J_{1mm} en fonction de la pré-déformation. La saturation observée expérimentalement n'est pas reproduite, une réduction de la pente est cependant observée. L'utilisation expérimentale d'un matériau laminé à froid permettant l'atteinte de plus forts niveaux d'écrouissage permettrait de valider ce résultat numérique.

VI.1 Introduction

In this chapter, the experimental results reported in chapter IV about the effect of prestrain on ductility and toughness are modelled using the constitutive equations and material parameters proposed in chapter V. Computational details (meshes...) are similar to those of chapter V. Although kinematic hardening plays a role on the plastic behaviour of the investigated X100 steel after prestraining (see chapter III), the damage model only accounts for isotropic hardening as the model including coupling between mixed hardening (isotropic+kinematic) and damage proposed by Besson and Guillemer-Neel [2003] was difficult to adjust. In addition convergence of finite element simulations was difficult to reach when coupling the description of plastic anisotropy and the description of kinematic hardening[1]. This short chapter is therefore a first attempt to model the effect of prestrain.

The X100 material is prestrained along the T direction under uniaxial tension. Prestrain levels (total engineering strain) are 0, 2, 4 and 6%. Values of the state variables p and f after prestrain are listed in Tab. VI.1. Due to the low stress triaxiality ratio $(1/3)$, the variation of damage is very limited during prestrain. These values will be used as initial state variables when simulating test on prestrained materials.

Table VI.1 : Values of p and f after prestrain.

prestrain (%)	0	2	4	6
p	0	$1.84\,10^{-2}$	$3.97\,10^{-2}$	$6.08\,10^{-2}$
f	$2.\,10^{-4}$	$2.084\,10^{-4}$	$2.186\,10^{-4}$	$2.293\,10^{-4}$

VI.2 Results for NT_χ specimens

Simulated load–diameter reduction curves for all notched geometries and prestrain levels are shown in Fig. VI.1. The maximum error between the experimental and simulated maximum loads is less than 5% with most of the differences being less than 2%. In all cases, it can be observed that the critical diameter reduction at crack initiation (see chapter IV), $E_c = \Delta\Phi_S|_c/\Phi_0$ decreases with increasing prestrain level.

$\Delta\Phi_S|_c/\Phi_0$ is plotted as a function of the prestrain level in Fig. VI.2. It is shown that the observed experimental trend (critical strain is decreased by the amount of prestrain) is well reproduced by the present model in particular for NT_4 specimens.

Prestrain has two effects: (i) it reduces the work-hardening capacity of the material, (ii) it induces initial damage. These two effects can be separated using the damage model. One series of calculations (referred to as "hardening only") was first performed using the values of the isotropic hardening variable p shown in Tab. VI.1 but using the initial value for damage $f = 2.\,10^{-4}$. A second series of calculations (referred to as "damage only") was performed using the values of damage listed in Tab. VI.1 together with $p = 0$ as initial state variables. Both series were performed for the NT_2 specimens tested along the L direction. Results are shown in Fig. VI.3. On the one hand it can be clearly seen (Fig. VI.3–c) that pre-damage is too small to significantly modify ductility. On the other hand pre-hardening only (Fig. VI.3–b) results is ductilities that are equal to those obtained assuming both pre-damage and pre-hardening (Fig. VI.3–a). This result is somehow obvious as pre-damage is very limited (see Tab. VI.1) ; however it clearly shows that pre-hardening can reduce ductility.

[1] In appendix A, a preliminary damage model incorporating damage, anisotropic plasticity and mixed isotropic/kinematic hardening is briefly presented based on the work by Besson and Guillemer-Neel [2003], Morgeneyer et al. [2009].

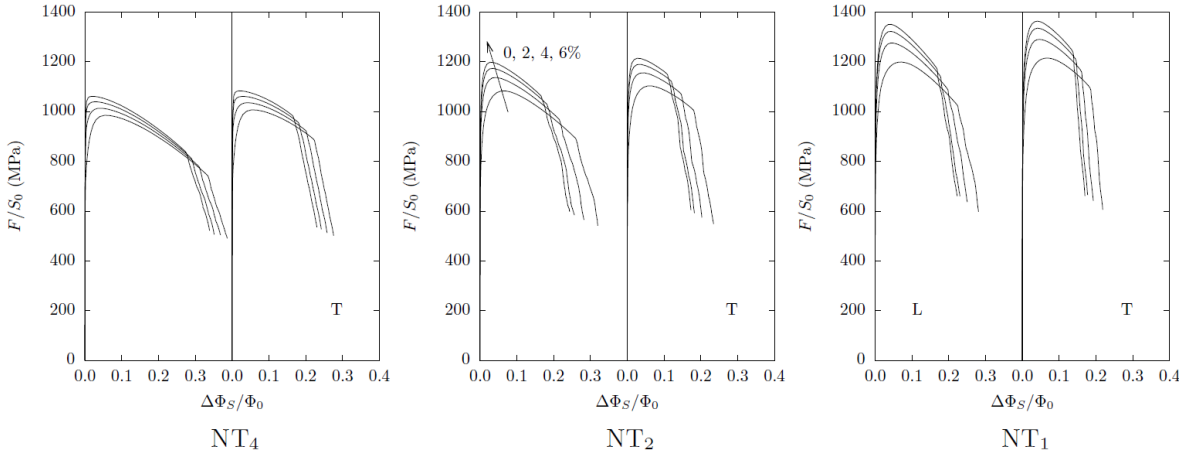

Figure VI.1 : Simulated normalized force—diameter reduction curves for $NT_{1,2,4}$ specimens and L and T directions for prestrain levels equal to 0, 2, 4 and 6%.

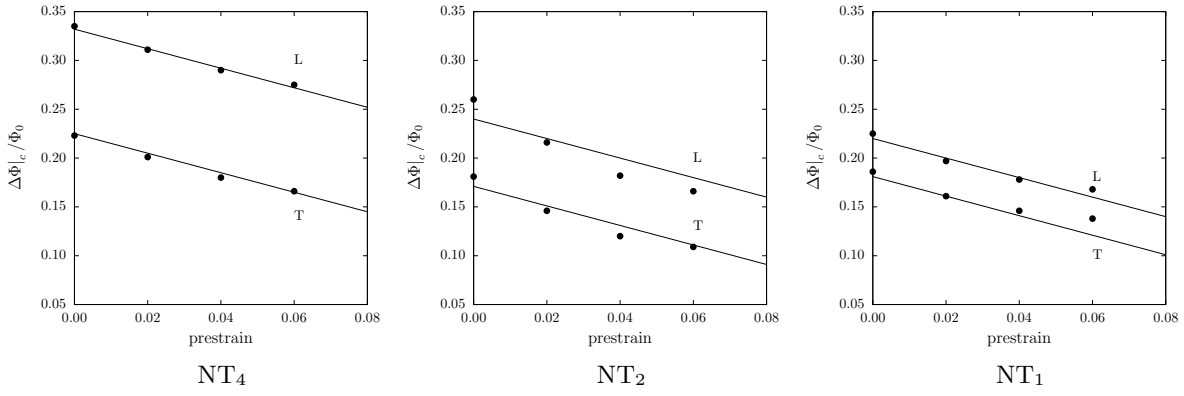

Figure VI.2 : Simulated evolution (symbols) of the critical diameter reduction $\Delta\Phi/\Phi_0|_c$ as a function of the prestrain level for $NT_{1,2,4}$ specimens and L and T directions. Lines corresponds to the experimentally observed trend: $\Delta\Phi|_c/\Phi_0(\text{prestrain}) \approx \Delta\Phi|_c/\Phi_0(0) - \text{prestrain}$.

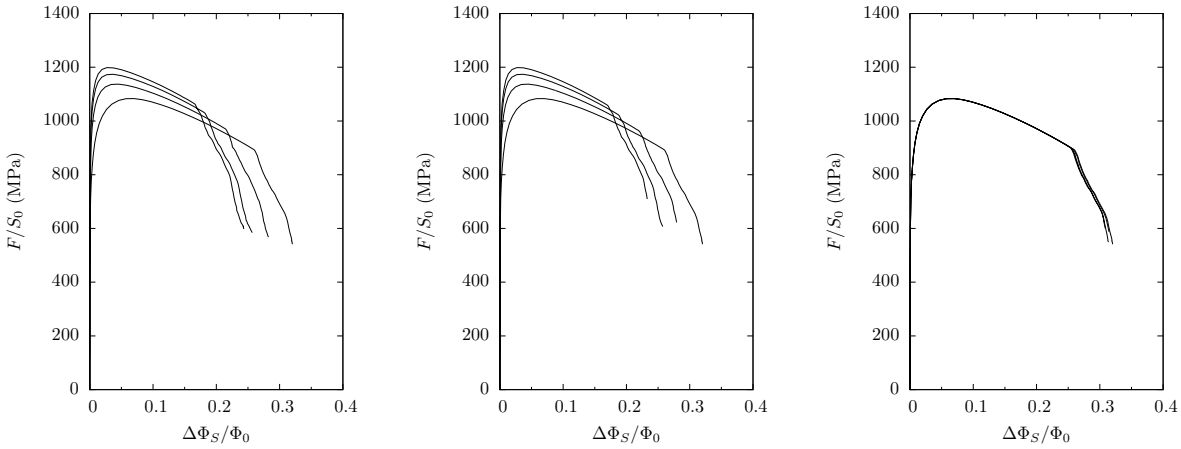

(a) hardening and damage (b) hardening only (c) damage only

Figure VI.3 : Simulated normalized force—diameter reduction curves for NT_2 specimens assuming that prestrain affects (a) both hardening and damage, (b) hardening only and (c) damage only.

Prestraining leads to a reduced hardening capability so that strain and damage localization become easier thus leading to a reduced ductility.

VI.3 Results for CT specimens

Simulated J—Δa curves for all prestrain levels are shown in Fig. VI.4 for the L–T and T–L configurations. In both cases J values for a given crack advance decrease with increasing prestrain level. The J value for 1 mm crack advance ($J_{1\mathrm{mm}}$) is plotted in Fig. VI.5 as a function of the prestrain level. It is observed that the decrease is faster for small values of prestrain. This result agrees with the observed experimental trends (see chapter IV) although the experimental results indicate a saturation of the decrease in toughness.

Calculations assuming that prestrain only affects damage or hardening were also performed. Conclusions are similar to those drawn from the study of notched bars: pre-damage has a negligible effect on toughness decrease which is only affected by pre-hardening. It is interesting to outline that prestraining increases the maximum load level obtained on CT specimens (as experimentally observed). This results, for a given CMOD, in a higher dissipated energy (e.g. A_p appearing in the calculation of J_p). Lower values of J for a given crack advance are therefore obtained because crack growth is faster in the prestrained material. In the present modelling framework this cannot be attributed to a change in damage growth rates as model parameters (in particular q_1 and q_2) are kept independent on the prestrain level. Crack growth is faster because of the easier strain and damage localization caused by the loss of hardening capability.

VI.4 Results for higher prestrain values

Prestrain of large tensile specimens was limited to 6% in order to prevent necking. Using the model, it is possible to simulate the effect of larger deformations. Results are presented in Fig. VI.6-a for notched specimens (L loading) and in Fig. VI.6-b for CT specimens for the L–T configuration. The predicted decrease in ductility and toughness does not appear to reach a plateau for prestrain levels up

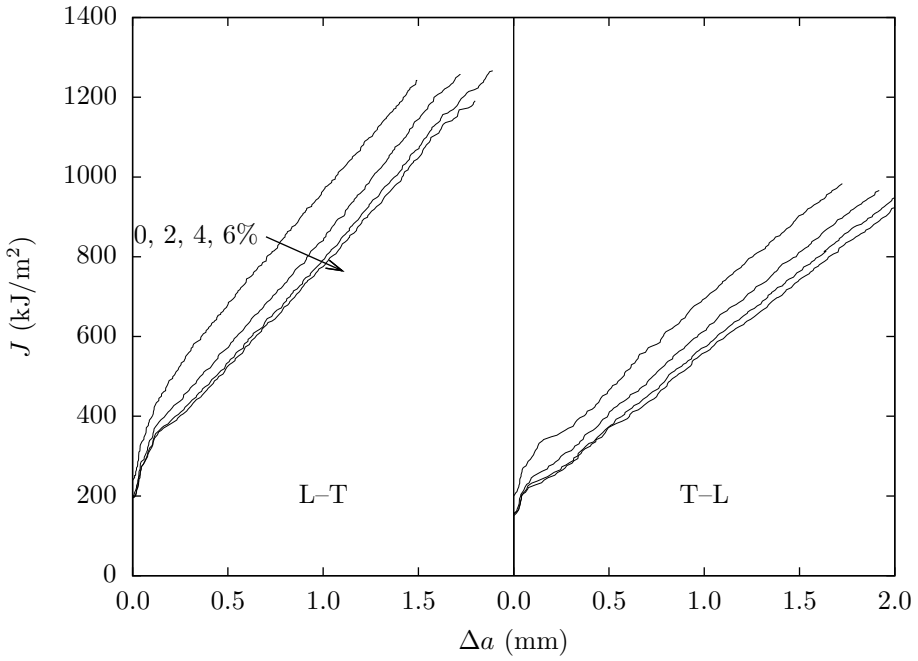

Figure VI.4 : J—Δa curves for L–T and T–L loading for prestrain levels equal to 0, 2, 4 and 6%.

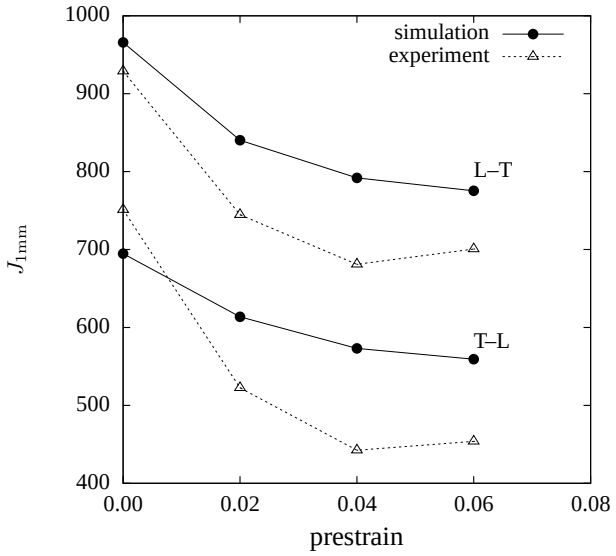

Figure VI.5 : J–value for 1mm crack advance ($J_{1\mathrm{mm}}$) as a function of prestrain level for L–T and T–L loading.

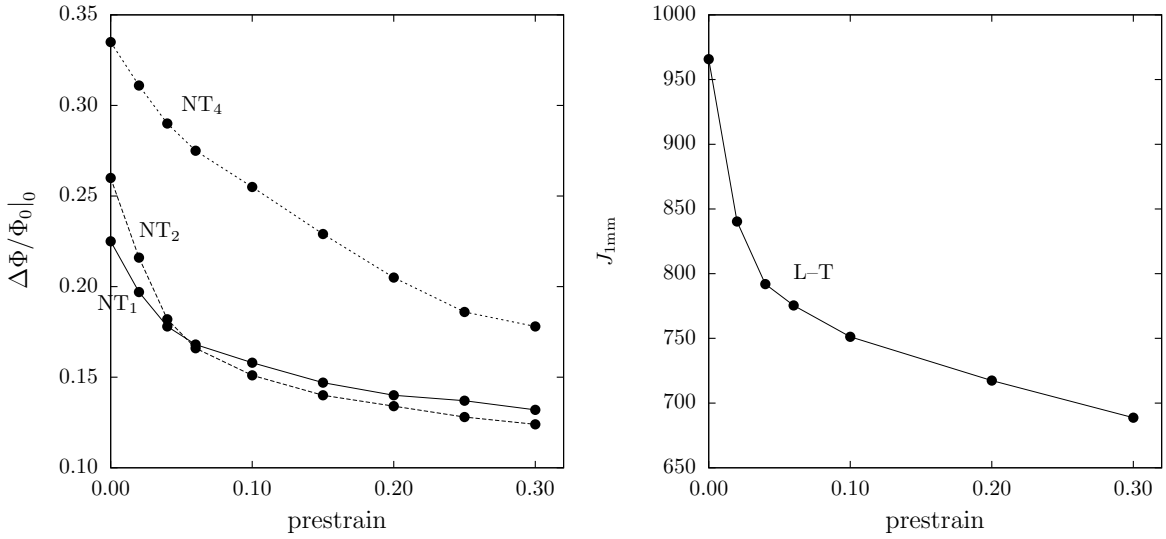

(a) NT specimens

(b) CT specimens

Figure VI.6 : (a) Variation of the the critical diameter reduction for L loading at large prestrain levels. (b) Variation of the $J_{1\mathrm{mm}}$ (L–T configuration) at large prestrain levels.

to 30%. However the decrease rate is reduced as the prestrain level is increased. These trends could be checked by using material prestrained using cold rolling in order to reach high prestrain levels.

VI.5 Conclusions

In this chapter, the effects of prestrain on ductility and toughness were evaluated using the constitutive equations and material parameters proposed in chapter V to reproduce results presented in chapter IV. Kinematic hardening was neglected. The X100 material was prestrained along the T direction under uniaxial tension. Prestrain levels (total engineering strain) were 0, 2, 4 and 6%.

The model is able to reproduce the fact that ductility ($E_c = \Delta\Phi_S|_c/\Phi_0$) of NT specimens is approximately decreased by the amount of prestrain. Decrease of toughness as a function of prestrain is also qualitatively reproduced for both L–T and T–L configurations.

Using the simulation tool, it was possible to evidence that the decrease of ductility and toughness is caused by the loss of work hardening caused by prestrain and not by damage accumulation during prestraining. The model also shows that prestrain levels larger than the necking strain could possibly cause a further decrease of ductility and toughness. This could be checked by using material prestrained using cold rolling.

Chapter -VII-

Conclusions and outlooks

Conclusions

In this thesis the influence of prestrain on anisotropic ductility and fracture toughness has been evaluated for API grade X100 line pipe steel. A comprehensive experimental investigation of microstructure, mechanical properties and fracture mechanisms has been carried out. A phenomenological model combining isotropic and kinematic hardening with anisotropic yield function has been developed, in order to represent anisotropic hardening behavior of the high strength steel. Additionally, a damage model incorporating anisotropic damage has been established for representation of prestrain effect on ductility and toughness of the X100 steel. The developed models could predict the bending capacity and the ductile fracture toughness of the cold-formed line pipes.

Plasticity : Tensile tests via a smooth and notched axisymmetric bars with different notch radii and plane strain specimens have been performed along different loading directions for as-received and prestrained materials, in order to investigate both anisotropy and prestrain effect of API grade X100 steel. It was found in the smooth bar tensile tests that the tested material had strong plastic anisotropy and isotropic/kinematic hardening behavior. Strain rate sensitivity was also investigated via smooth tensile tests at room temperature. X100 steel exhibits a slightly strain rate sensitivity. In order to represent these experimental results, the new phenomenological model was developed in this thesis. The model proposed by Bron and Besson [2004] was combined with the kinematic model. All parameters of the model were adjusted on the experimental results so that the model could simulate the anisotropic plasticity in all small-scale tensile tests. The bending capacity of the X100 pipe with geometric imperfection effect was analysed using the developed model. The numerical results suggest that prestraining level in the pipe forming process should strongly affect the bending capacity, especially under the end-capped condition.

Experimental characterisation of anisotropy rupture and prestrain effect : Three kinds of fracture toughness tests, such as CT, SENB and SENT, as well as a smooth bar, three types of notched bar and plane strain tensile tests were carried out to evaluate ductility and toughness of the API X100 steel. The critical strain at the onset of fracture in the notched bar specimens was evaluated. The critical strain decreased with increasing notch severity. In the specimen with sharp notch radii (NT_1), the strain was small. It is well-known as stress triaxiality effect. The value was also affected by loading-direction. The critical value was higher in T loading direction than L loading direction.

Furthermore, the critical value deteriorated by prestraining level. The value reduced by the prestrain level in the NT_4 specimen, while some deviation is observed for the other specimens. Ductility, which is characterized by the fracture area reduction in all tensile specimens, was evaluated. The value linearly decreased by the prestrain level in all types of tensile tests. Regarding ductile fracture toughness, the ductile crack initiation and the ductile tearing resistance were evaluated in three kinds of fracture toughness tests. As the received state, the crack initiation was independent of the specimen geometry and the loading direction. On the other hand, the crack advance resistance was strongly affected by the specimen geometry and the loading direction. The resistance for L-T configuration was higher than T-L one. The value became higher in CT, SENB and SENT specimen, respectively. Prestrain deteriorated the crack initiation, while had small effect on the tearing resistance, in CT and SENB tests.

Model for anisotropic ductile rupture : In order to represent the anisotropic ductility and toughness of API X100 steel as the received state, a semi-phenomenological modification of the Gurson damage model was developed. Unit cell calculations were carried out in order to clarify the effect of the main loading direction on void growth rate. For a constant stress triaxiality ratio, void growth rate depended on the main loading direction. The Gurson–like model tuned on the unit cell calculations was unable to reproduce fracture anisotropy which was strongly underestimated. The anisotropic rupture behavior could , however, be represented using the same semi-phenomenological modification of the Gurson model which was tuned on experiments on notched bars. Using the tuned parameters it became possible to simulate anisotropic crack extension in both CT and SENB.

Simulation of the effect of prestrain on ductility and toughness : Simulation of prestrain effect on ductility and toughness was attempted using the constitutive equation coupling anisotropic plasticity, damage and mixed hardening models. The X100 material was prestrained along the T direction under uniaxial tension. Prestrain levels (total engineering strain) were 0, 2, 4 and 6%. In the notched bar tensile simulations, the maximum error between the experimental and simulated maximum loads was less than 5%İn all cases, it was observed that the critical strain at crack initiation decreased with increasing prestrain level. Prestrain has two effects: (i) reduces the work-hardening capacity of the material, (ii) induces initial damage. However, the pre-damage was very limited and the pre-hardening strongly affected ductility. Namely, Prestraining might have a role of reduction in hardening capability so that strain and damage localization become easier leading to a reduced ductility and toughness.

Outlook

SENT test specimens : In this study a semi-phenomenological modification of the Gurson damage model was developed in order to represent the anisotropic ductility and toughness of API grade X100 steel. Simulations of anisotropic crack extension in both CT and SENB tests was able to be performed by using the optimized parameters of the developed model. However preliminary simulations have shown that the semi-phenomenological damage model could not simulate SENT tests in both L and T loading direction. That might be because the mechanism of ductile failure in the SENT specimen is different from in the CT and SENB ones. Although the J-integral value at crack advance initiation was almost the same level among SENT, SENB and CT tests, the crack tearing resistance of the SENT specimen was much higher than those of SENB and CT ones. It would be necessary to clarify effect of loading mode (tension and bend) on the stress field localized in the crack tip and improve the developed damage model for representation the ductile crack tearing behavior in tension loading mode such as the SENT test for which the crack tip stress triaxiality is significantly smaller.

Simulation combining forming, straining, and fracture : FE model for representation of anisotropic plasticity and kinematic hardening in API grade X100 steel was developed in this thesis. A welded pipe such as UOE has anisotropic tensile properties due to the cold pipe forming. The developed model could simulate the UOE pipe process and predict the pipe's anisotropy. Furthermore, the semi-phenomenological damage model proposed in this study, which can represent anisotropic ductility and toughness of prestrained material, has potential to use fracture assessment for strain-based design. Using the phenomenological combined model to represent anisotropic plasticity, kinematic hardening and damage anisotropy, a sequence of simulations (cold pipe forming in a UOE pipe mill, the UOE pipe's anisotropic properties and the ductile fracture behavior under the operation condition) could be developed in the further work.

Improving the damage model : The proposed model could be improved to better describe the fracture behavior of SENT specimens. This could possibly be done by incorporating the effect of the Lode parameter (third stress invariant) on damage developpement as proposed in Nahshon and Hutchinson [2008]. It is also well known that simulations using damage models leads to mesh dependent results (dependance on the mesh size but also mesh direction, element type...). These simulations would greatly benefit from improved computational methods (for instance based on non-local formulations) allowing having fracture energies independent on mesh design [Hütter et al. 2013, Mediavilla et al. 2006, Bargellini et al. 2009].

Bibliography

H. Asahi, T. Hara, E. Tsuru, and H. Morimoto, 2009. Development and commercialiation of high-strength linepipe. In: Proc. pipeline technology conference, Ostend 12-14 October 2009.

ASTM, 2006. Standard E1820-06.2006. Tech. rep., ASTM-International.

J.-H. Baek, Y.-P. Kim, C.M. Kim, W.S. Kim, and C.S. Seok, 2010. Effects of pre-strain on the mechanical properties of API 5L X65 pipe. Mater. Sci. Eng. A 527 (6), 1473–1479.

J.P. Bandstra and D.A. Koss, 2008. On the influence of void clusters on void growth and coalescence during ductile failure. Acta Mater. 56, 4429–4439.

R. Bargellini, J. Besson, E. Lorentz, and S. Michel-Ponnelle, 2009. A nonlocal finite element based on volumetric strain gradient: application to ductile fracture. Comput. Mat. Sci. , in press.

F. Barlat, H. Aretz, J.W. Yoon, M.E. Karabin, J.C. Brem, and R.E. Dick, 2005. Linear transfomation-based anisotropic yield functions. Int. J. Plasticity 21 (5), 1009–1039.

F. Barlat, D.J. Lege, and J.C. Brem, 1991. A six–component yield function for anisotropic materials. Int. J. Plasticity 7, 693–712.

M. Ben Bettaieb, X. Lemoine, O. Bouaziz, A.-M. Habraken, and L. Duchene, 2011. Numerical modeling of damage evolution of DP steels on the basis of X-ray tomography measurements. Mechanics of Materials 43 (3), 139–156.

A.A. Benzerga and J. Besson, 2001. Plastic potentials for anisotropic porous solids. Eur. J. Mech. A-solids 20A (3), 397–434.

A. Benzerga, J. Besson, and A. Pineau, 1999. Coalescence–controlled anisotropic ductile fracture. J. Engng Mater. Technol. 121, 121–229.

A.A. Benzerga, J. Besson, and A. Pineau, 2004a. Anisotropic ductile fracture Part I: experiments. Acta Mater. 52, 4623–4639.

A.A. Benzerga, J. Besson, and A. Pineau, 2004b. Anisotropic ductile fracture Part II: theory. Acta Mater. 52, 4639–4650.

A.A. Benzerga and J.-B. Leblond, 2010. Ductile Fracture by Void Growth to Coalescence. Advances in Applied Mechanics 44, 169–305.

J. Besson, 2010. Continuum models of ductile fracture : a review. Int. J. Damage Mech. 19, 3–52.

J. Besson and R. Foerch, 1997. Large scale object–oriented finite element code design. Comp. Meth. Appl. Mech. Engng 142, 165–187.

J. Besson and C. Guillemer-Neel, 2003. An extension of the Green and Gurson models to kinematic hardening. Mechanics of Materials 35, 1–18.

J. Besson, D. Steglich, and W. Brocks, 2001. Modeling of crack growth in round bars and plane strain specimens. Int. J. Solids Structures 38 (46–47), 8259–8284.

P.W. Bridgman, 1952. Studies in large plastic flow and fracture. McGraw–Hill.

F. Bron and J. Besson, 2004. A yield function for anisotropic materials. Application to aluminium alloys. Int. J. Plasticity 20, 937–963.

F. Bron and J. Besson, 2006. Simulation of the ductile tearing for two grades of 2024 aluminum alloy thin sheets. Engng Fract. Mech. 73, 1531–1552.

M. Brunet, F. Morestin, and H. Walter-Leberre, 2005. Failure analysis of anisotropic sheet-metals using a non-local plastic damage model. J. Mater. Processing Technol. 170, 457–470.

J.L. Chaboche, 1986. Time-independent constitutive theories for cyclic plasticity. Int. J. Plasticity 2, 149–188.

J.L. Chaboche, 2008. A review of some plasticity and viscoplasticity constitutive theories. Int. J. Plasticity 24, 1642–1693.

J.-L. Chaboche, 1989. Constitutive equations for cyclic plasticity and cyclic viscoplasticity. Int. J. Plasticity 5, 247–302.

C.C. Chu and A. Needleman, 1980. Void nucleation effects in biaxially stretched sheets. J. Engng Mater. Technol. 102, 249–256.

M. Civallero, M. Mirabile, and G.C. Sih, 1981. Fracture mechanics in pipeline technology. In: G.C. Sih and M. Mirabile (Eds.), Analytical and Experimental Fracture Mechanics. Rome, pp. 157–174.

K.T. Corbet, R.R Bowen, and C.W. Petersen, 2003. ?? In: Proc. international offshore and polar engineering (ISOPE) conference, Honolulu May 2003.

S. Cravero and C. Ruggieri, 2007. Estimation procedure of J-resistance curves for SE(T) fracture specimens using unloading compliance. Engng Fract. Mech. 74, 2735–2757.

K. Danas and P. Ponte-Castaneda, 2009a. A finite-strain model for anisotropic viscoplastic porous media: I — Theory. Eur. J. Mech./A 28 (3), 387–401.

K. Danas and P. Ponte-Castaneda, 2009b. A finite-strain model for anisotropic viscoplastic porous media: II — Applications. Eur. J. Mech./A 28 (3), 402–416.

K. Decamp, L. Bauvineau, J. Besson, and A. Pineau, 1997. Size and geometry effects on ductile rupture of notched bars in a C–Mn steel: Experiments and modelling. Int. J. Frac. 88 (1), 1–18.

L. Devillers-Guerville, J. Besson, and A. Pineau, 1997. Notch fracture toughness of a cast duplex stainless steel: modelling of experimental scatter and size effect. Nucl. Eng. Design 168, 211–225.

DNV, 2006. Fracture control for pipeline installation methods introducing cyclic plastic strain. Tech. rep.

K. Enami, 2005. The effects of compressive and tensile prestrain on ductile fracture initiation in steels. Engng Fract. Mech. 72 (7), 1089–1105.

D. Fabrègue and T. Pardoen, 2008. A constitutive model for elastoplastic solids containing primary and secondary voids. J. Mech. Phys. Solids 56, 719–741.

D. P. Fairchild, W. Cheng, S. J. Ford, K. Minnaar, N. E. Biery, A. Kumar, and N. E. Nissley, 2008. Recent advance in curved wide plate testing and implications for strain-based design. Int. J. of offshore and polar engineering 18 (3), 161–170.

J. Faleskog, X. Gao, and C.F. Shih, 1998. Cell model for nonlinear fracture analysis — I. Micromechanics calibration. Int. J. Frac. 89, 355–373.

J. Faleskog and C.F. Shih, 1997. Micromechanics of coalescence — I. Synergistic effects of elasticity, plastic yielding and multi–size–scale voids. J. Mech. Phys. Solids 45 (1), 21–50.

J. Besson Feld-Payet S., F. Feyel, 2011. Finite element analysis of damage in ductile structures using a nonlocal model combined with a three-field formulation. Int. J. Damage Mech. 20, 655–680.

R. Foerch, J. Besson, G. Cailletaud, and P. Pilvin, 1997. Polymorphic constitutive equations in finite element codes. Comp. Meth. Appl. Mech. Engng 141, 355–372.

X. Gao, J. Faleskog, and C.F. Shih, 1998. Cell model for nonlinear fracture analysis — ii. fracture–process calibration and verification. Int. J. Frac. 89, 375–398.

A. Glover and B. Rothwell, 2008. Yield strength and plasticity of high strength pipelines. In: Proc. 4th international conference on pipeline technology (IPC), Ostend 9-13 May 2008.

M. Gologanu, J.B. Leblond, and J. Devaux, 1993. Approximate models for ductile metals containing non–spherical voids — case of axisymmetric prolate ellipsoidal cavities. J. Mech. Phys. Solids 41 (11), 1723–1754.

M. Gologanu, J.B. Leblond, and J. Devaux, 1994. Approximate models for ductile metals containing non–spherical voids — case of axisymmetric oblate ellipsoidal cavities. J. Engng Mater. Technol. 116, 290–297.

M. Gologanu, J.B. Leblond, G. Perrin, and J. Devaux, 2001. Theoretical models for void coalescence in porous ductile solids. I. Coalescence “in layers”. Int. J. Solids Structures 38, 5581–5594.

M.K. Graf, H.G. Hillenbrand, C.J. Heckmann, and K.A. Niederhoff, 2004. High-strength large-diameter pipe for long-distance high-pressure gas pipelines. Int. J. Offshore Polar Eng. 14 (1), 69–74.

A.S. Gullerud, X. Gao, R.H. Dodds Jr, and R. Haj-Ali, 2000. Simulation of ductile crack growth using computational cells: numerical aspects. Engng Fract. Mech. 66, 65–92.

A.L. Gurson, 1977. Continuum theory of ductile rupture by void nucleation and growth: Part I—Yield criteria and flow rules for porous ductile media. J. Engng Mater. Technol. 99, 2–15.

H. Haddadi, S. Bouvier, M. Banu, C. Maier, and C Teodosiu, 2006. Towards an accurate description of the anisotropic behaviour of sheet metals under large plastic deformations. Int. J. Plasticity 22, 2226–2271.

M. D. Herynk, S. Kyriakides, A. Onoufriou, and H. D. Yun, 2007. Effects of the UOE/UOC pipe manufacturing processes on pipe collapse pressure. Int. J. Mech. Sci. 49 (5), 533–553.

R. Hill, 1950. The mathematical theory of plasticity. Clarendon Press, Oxford.

T. Hoc and S. Forest, 2001. Polycrystal modelling of IF-Ti steel under complex loading path. Int. J. Plasticity 17, 65–85.

O.S. Hopperstad, M. Landseth, and S. Remseth, 1995a. Cyclic stress-strain behaviour of alloy AA6060 Part II:uniaxial experiments and modelling. Int. J. Plasticity 11, 725–739.

O.S. Hopperstad, M. Landseth, and S. Remseth, 1995b. Cyclic stress-strain behaviour of alloy AA6060 T4 Part II:biaxial experiments and modelling. Int. J. Plasticity 11, 741–762.

T.J.R. Hughes, 1980. Generalization of selective integration procedures to anisotropic and non linear media. Int. J. Numer. Meth. Engng 15, 1413–1418.

N.S. Huh, Y.J. Kim, and Y.J. Kim, 2007. Limit load solutions for pipes with through-wall crack under single and combined loading based on finite element analyses. J. Pressure Vessel Technol. 129, 468–472.

G. Hütter, T. Linse, U. Mühlich, and M. Kuna, 2013. Simulation of ductile crack initiation and propagation by means of a non-local Gurson-model. Int. J. Solids Structures 50, 662–671.

IEA, 2009. Key world energy statistics.

S. Igi, J. Kondo, N. Suzuki, and D. Duan, 2008. Strain capacity of x100 high-strain linepipe for strain-based design application. In: Proc. 7th international pipeline conference, Calgary 29 September-3 October 2008.

M. Kailasam, N. Aravas, and P. Ponte Castañeda, 2000. Porous metals with developing anisotropy: Constitutive models, computational issues and applications to deformation processing. Comput. Model. Engrg Sci. 1 (2), 105–118.

A.P. Karafillis and M.C. Boyce, 1993. A general anisotropic yield criterion using bounds and a transformation weighting tensor. J. Mech. Phys. Solids 41, 1859–1886.

S.M. Keralavarma and A.A. Benzerga, 2008. An approximate yield criterion for anisotropic porous media. C. R. Mécanique 336, 685–692.

S.M. Keralavarma, S. Hoelscher, and A.A. Benzerga, 2011. Void growth and coalescence in anisotropic plastic solids. Int. J. Solids Structures 48 (11-12), 1696–1710.

D. Kim, F. Barlat, S. Bouvier, M. Rabahallah, T. Balan, and K. Chung, 2007. Non-quadratic anisotropic potentials based on linear transformation of plastic strain rate. Int. J. Plasticity 2, 1380–1399.

J. Koplik and A. Needleman, 1988. Void growth and coalescence in porous plastic solids. Int. J. Solids Structures 24 (8), 835–853.

H. Laurent, R. Greze, P. Y. Manach, and S. Thuillier, 2009. Influence of constitutive model in springback prediction using the split-ring test. Int. J. Mech. Sci. 51 (3), 233–245.

L. Lecarme, C. Tekoğlu, and T. Pardoen, 2011. Void growth and coalescence in ductile solids with stage III and stage IV strain hardening. Int. J. Plasticity 27 (8), 1203–1223.

D.H. Lee, B.H. Kim, H. Lee, and J.S. Kong, 2009. Seismic behavior of a buried gas pipeline under earthquake excitations. Eng. Struct. 31 (5), 1011–1023.

D.B. Lillig, 2008. The first (2007) isope strain-based design symposium - a review. In: Proc. 18th international offshore and polar engineering (ISOPE) conference, Vancouver 6-11 july 2008.

M. Liu and Y.-Y. Wang, 2007. Modeling of anisotropy of TMCP and UOE linepipes. Int. J. Offshore Polar Eng. 17 (4), 288–293.

R.W. Logan and W.F Hosford, 1980. Upper-bound anisotropic yield locus calculations assuming (111)-pencil glide. Int. J. Mech. Sci. 22 (7), 419–430.

A.C. Mackenzie, J.W. Hancock, and D.K. Brown, 1977. On the influence of state of stress on ductile failure initiation in high strength steels. Engng Fract. Mech. 9, 167–188.

H. Makino, I. Takeuchi, and R. Higuchi, 2008. Fracture propagation and arrest in high-pressure gas transmission pipeline by ultra high strength line pipes. In: Proc. 7th international pipeline conference, Calgary 29 September-3 October 2008.

W.A. Maxey, 1981. Dynamic crack propagation in line pipe. In: G.C. Sih and M. Mirabile (Eds.), Analytical and Experimental Fracture Mechanics. Rome, pp. 109–123.

H. Mecking and U.F. Kocks, 1981. Kinetics of flow and strain-hardening. Acta Metall. 29 (11), 1865–1875.

J. Mediavilla, R.H.J. Peerlings, and M.G.D. Geers, 2006. Discrete crack modelling of ductile fracture driven by non-local softening plasticity. Int. J. Numer. Meth. Engng 66 (4), 661–688.

G. Mirone, 2004. A new model for the elastoplastic characterization and the stress–strain determination on the necking section of a tensile specimen. Int. J. Solids Structures 2004, 3545–3564.

V. Monchiet, O. Cazacu, E. Charkaluk, and D. Kondo, 2008. Macroscopic yield criteria for plastic anisotropic materials containing spheroidal voids. Int. J. Plasticity 24, 1158–1189.

V. Monchiet, C. Gruescu, E. Charkaluk, and D. Kondo, 2006. Approximate yield criteria for anisotropic metals with prolate or oblate voids. C. R. Mécanique 334 (7), 431–439.

T.F. Morgeneyer, J. Besson, H. Proudhon, M.J. Starink, and I. Sinclair, 2009. Experimental and numerical analysis of toughness anisotropy in AA2139 al alloy sheet. Acta Mater. 57 (13), 3902–3915.

K. Nahshon and J.W. Hutchinson, 2008. Modification of the Gurson model for shear failure. Eur. J. Mech. A-solids 27A, 1–17.

A. Needleman, 1990. An analysis of tensile decohesion along an interface. J. Mech. Phys. Solids 38, 289–324.

M Ohata and M Toyoda, 2004. Damage concept for evaluating ductile cracking of steel structure subjected to large-scale cyclic straining. Sci. Technol. Adv. Mater. 5 (1-2), 241–249.

T. Pardoen and J.W. Hutchinson, 2000. An extended model for void growth and coalescence. J. Mech. Phys. Solids 48 (12), 2467–2512.

T. Pardoen and J.W. Hutchinson, 2003. Micromechanics–based model for trends in toughness of ductile metals. Acta Mater. 51, 133–148.

F. Rivalin, J. Besson, M. Di Fant, and A. Pineau, 2000a. Ductile tearing of pipeline-steel wide plates — II.: Modeling of in–plane crack propagation. Engng Fract. Mech. 68 (3), 347–364.

F. Rivalin, A. Pineau, M. Di Fant, and J. Besson, 2000b. Ductile tearing of pipeline-steel wide plates — I. dynamic and quasi-static experiments. Engng Fract. Mech. 68 (3), 329–345.

G. Rousselier, 1987. Ductile fracture models and their potential in local approach of fracture. Nucl. Eng. Design 105, 97–111.

C. Ruggieri, T.L. Panontin, and R.H. Dodds Jr., 1996. Numerical modeling of ductile crack growth in 3-d using computational cell elements. Int. J. Frac. 82, 67–95.

K. Sai, G. Cailletaud, and S. Forest, 2006. Micro-mechanical modeling of the inelastic behavior of directionally solidified materials. Int. J. Plasticity 38, 203–217.

H. Samrout, R. ElAbdi, and J.L. Chaboche, 1997. Model for 28CrMoV5-8 steel undergoing thermomechanical cyclic loadings. Int. J. Solids Structures 34 (35-36), 4547–4556.

Y. Shinohara, Y. Madi, and J. Besson, 2010. A combined phenomenological model for the representation of anisotropic hardening behavior in high strength steel line pipes. Eur. J. Mech. A-solids 29 (6), 917–927.

Y. Shinohara, E. Tsuru, H. Asahi, T. Hara, Y. Terada, N. Doi, N. Ayukawa, and M. Murata, 2008. Development of high-strength steel line pipe for SBD applications. Int. J. of offshore and polar engineering 18 (3), 220–225.

F. Sidoroff and A. Dogui, 2001. Some issues about anisotropic elastic-plastic models at finite strain. Int. J. Solids Structures 38, 9569–9578.

T. Siegmund and W. Brocks, 1999. Prediction of the work of separation and implications to modelling. Int. J. Frac. 99, 97–116.

J.C. Simo and R.L. Taylor, 1985. Consistent tangent operators for rate–independent elastoplasticity. Comp. Meth. Appl. Mech. Engng 48, 101–118.

S. Sivaprasad, S. Tarafder, V.R. Ranganath, and K.K Ray, 2000. Effect of prestrain on fracture toughness of hsla steels. Mater. Sci. Eng. A 284, 195–201.

D. Steglich and W. Brocks, 1997. Micromechanical modelling of the behaviour of ductile materials including particles. Comput. Mat. Sci. 9, 7–17.

D. Steglich, T. Siegmund, and W. Brocks, 1999. Micromechanical modeling of damage due to particle cracking in reinforced metals. Comput. Mat. Sci. 16, 404–413.

D. Steglich, H. Wafai, and J. Besson, 2010. Interaction between anisotropic plastic deformation and damage evolution in Al 2198 sheet metal. Engng Fract. Mech. 77 (17), 3501–3518.

B. Tanguy, T.T. Luu, G. Perrin, A. Pineau, and J. Besson, 2008. Plastic and damage behavior of a high strength X100 pipeline steel: experiments and modelling. Int. J. of Pressure Vessels and Piping 85 (5), 322–335.

V. Tarigopula, O. S. Hopperstad, M. Langseth, and A. H. Clausen, 2008. Elastic-plastic behaviour of dual phase, high-strength steel under strain-path changes. European Journal of Mechanics A/solids 27, 764–782.

V. Tarigopula, O. S. Hopperstad, M. Langseth, and A. H. Clausen, 2009. An evaluation of a combined isotropic-kinematic hardening model for representation of complex strain-path changes in dual-phase steel. Eur. J. Mech. A-Solids 28 (4), 792–805.

C. Teodosiu and Z. Hu, 1995. Evalution of the intragranular microstructure at moderate and large strains. In: Proceedings of the 5th NUMIFORM conference. Simulation of materials proceeding: Theoroy, Methods and Applications.

P. F. Thomason, 1968. A theory for ductile fracture by internal necking of cavities. J. Ins. Metals 96, 360–365.

P. F. Thomason, 1985a. A three–dimensional model for ductile fracture by the growth and coalescence of microvoids. Acta Metall. 33 (6), 1087–1095.

P. F. Thomason, 1985b. Three–dimensional models for the plastic limit–loads at incipient failure of the intervoid matrix in ductile porous solids. Acta Metall. 33 (6), 1079–1085.

C.M.J. Timms, D.D. DeGeer, M.R. Tsuru Chebaro, and E. Tsuru, 2009. Compressive strain limits of large diameter X80 UOE linepipe. In: Proc. 19th international offshore and polar engineering (ISOPE) conference, Osaka 21-26 june 2009.

J.M. Treinen, W.E. Luecke, J.D. Colskey, P.P. Darcis, and Y.Y. Wang, 2008. Anisotropic behavior of x100 pipeline steel. In: Proc. Eighteenth Int. Offshore and Polar Engineering Conf., Vancouver, Canada. ISOPE.

E. Tsuru and J. Agata, 2009. Buckling resistance of line pipes with girth weld evaluated by new computational simulation and experimental technology for full-scale pipes. In: Proc. 19th international offshore and polar engineering (ISOPE) conference, Osaka 21-26 june 2009.

E. Tsuru, Y. Shinohara, and H. Asahi, 2008. Evaluation precept for buckling resistance of high-strength uoe line pipes used in strainbased design SBD applications. Int. J. of offshore and polar engineering 18 (3), 176–182.

E. Tsuru, Y. Shinohara, H. Asahi, and Y. Terada, 2005. Strain capacity of line pipe with yield point elongation. In: Proc. 15th international offshore and polar engineering (ISOPE) conference, Seoul 2005.

V. Tvergaard, 1990. Material failure by void growth to coalescence. Advances in Applied Mechanics 27, 83–151.

V. Tvergaard and A. Needleman, 1984. Analysis of the cup–cone fracture in a round tensile bar. Acta Metall. 32, 157–169.

I.N. Vladimirov, M.P. Pietryga, and S. Reese, 2010. Anisotropic finite elastoplasticity with nonlinear kinematic and isotropic hardening and application to sheet metal forming. Int. J. Plasticity 26 (5), 659–687.

Y. Wang and M. Liu, 2007. The role of anisotropy, toughness transferability and weld misalignment in the strain based design of pipelines. In: Proc. 17th international offshore and polar engineering (ISOPE) conference, Lisbon 1-6 july 2007.

W.W. Wiedenhoff, G.H. Vogt, and P.A. Peters, 1984. Toughness requirements of large-diameter line pipe in gas transmission pipelines. In: International Seminar on Fracture in Gas Pipelines. Moscou.

S.K. Yerra, C. Tekoglu, F. Scheyvaerts, L. Delannay, P. Van Houtte, and T. Pardoen, 2010. Void growth and coalescence in single crystals. Int. J. Solids Structures 47, 1016–1029.

Q. M. Yu, N. X. Hou, and Z. F. Yue, 2010. Finite element analysis of void growth behavior in nickel-based single crystal superalloys. Comput. Mat. Sci. 48 (3), 597–608.

Z.L. Zhang, M. Hauge, J. Ødegård, and C. Thaulow, 1999. Determining material true stress–strain curve from tensile specimens with rectangular cross–section. Int. J. Solids Structures 36, 3497–3516.

T.J.E. Zimmerman, M.J Stephens, D.D. DeGeer, and C. Chen, 1995. Compressive strain limits for burried pipelines. In: Proc. 14th international conference on offshore mechanics and arctic engineering (OMAE 1995).

N. Zouhal, A. Molinari, and L.S. Tóth, 1996. Elastic-plastic effects during cyclic loading as predicted by the Taylor–Lin model of polycrystal elasti-viscoplasticity. Int. J. Plasticity 12 (3), 343360.

Appendix -A-

Anisotropic Damage Behavior in High-Strength Line Pipe Steels

Paper published int Int. J. Offshore and Polar Engineering

International Journal of Offshore and Polar Engineering (ISSN 1053-5381)

Vol. 22, No. 1, March 2012, pp. 83–89

http://www.isope.org/publications

Anisotropic Damage Behavior in High-Strength Line Pipe Steels

Yasuhiro Shinohara
Steel Research Laboratories, Nippon Steel Corporation, Futtsu, Japan

Yasuhiro Shinohara and Jacques Besson
Centre des Matériaux, Mines Paris, Paristech, CNRS UMR 7633, Evry, France

Yazid Madi
Ermess, EPF, Ecole d'Ingénieurs, Sceaux, France

High-strength steel line pipes have different mechanical properties (plasticity, ductility and toughness) in each direction. This anisotropy is developed by a thermo-mechanical control process (TMCP) in a heavy plate mill and a cold forming process in a pipe mill. In this study, experimental work was carried out using both as received and pre-strained (up to 6% along the T direction) steel plates for X100-grade pipes, in order to analyze anisotropic toughness. Compact tests were conducted in the longitudinal (L) and transverse (T) directions. Further, a new damage model based on the GTN model was proposed, in order to represent anisotropic damage behavior in high-strength line pipe steels.

INTRODUCTION

As consumption of energy is increasing worldwide, demand for the development of oil and gas resources in remote locations becomes strong. These development areas are often far from major consumers because the potential locations are in harsh environments. Environmental loads by offshore ice, discontinuous permafrost and seismic activity impose a strain-caused burden on the pipeline structures transporting the oil and gas from these remote resources to the population centers.

While the stress-based design (SBD) of pipelines is normally preferred, the nature of these environmental loads makes (SBD) a necessity in these harsh environments. The accurate prediction of the environmentally imposed strain by pipeline designers, and the accommodation of this strain by installation of advanced steels for pipelines, are essential to the operation of a safe and reliable pipeline.

The basic materials requirements for the SBD line pipe steels are generally the control of longitudinal yield strength, low yield-to-tensile strength (Y/T) ratio, high strain-hardening exponent, high uniform elongation, and good toughness (Glover and Rothwell, 2004). Additionally, aging effects on tensile properties during the coating process must be minimized and fully characterized (Shinohara et al., 2005; Timms et al., 2005).

For the accurate prediction of strain demand in the new design, we need to consider strain limits at both tensile and compressive sides during the pipe's bending deformation (Tsuru et al., 2008; Igi et al., 2008).

In order to determine these strain limits, the full-size pipe bending test and the curved wide-plate tests are performed. Finally, the numerical simulations using finite element analysis (FEA) are utilized for specifying the effective mechanical properties in the pipes, checking the predicted values against the experimental results. Recently, the detailed mechanical properties of UOE line pipes in practical use have been discussed for investigating the high reliability of SBD. The strengths in UOE pipes are distributed by the plastic strain developed in the pipe forming process, so the strain capacity under the bending moment is dependent on the loading orientation. The strength is also different between the longitudinal direction and the circumferential direction, the so-called orthogonal anisotropy (Shinohara et al., 2006; Tsuru et al., 2008).

The effects of strength anisotropy in UOE pipes on the strain capacity under the bending moment have recently been studied (Tsuru et al., 2008). A constitutive model with anisotropic strain-hardening based on Hill's quadratic yield function was developed. The numerical analysis indicated that the anisotropic hardening significantly affected the buckling resistance, especially under high internal pressure.

Moreover, some recent reports have indicated that the pipe properties, including the anisotropy between the hoop and longitudinal tensile properties of the pipe, could have an influence on the tensile strain limit (Wang and Liu, 2007; Gordon et al., 2007).

Orthogonal anisotropy is enhanced by pre-straining as well as development of crystallographic texture. This study's objective is to reveal the anisotropic damage behavior of high-strength line pipe steels by conducting fracture toughness tests for as-received and pre-strained X100 steel plates.

MATERIAL AND EXPERIMENTAL PROCEDURE

The tested steel was a high-strength, 16-mm-thick steel plate. The plate was produced in a commercial heavy-plate mill for experimental manufacture of API X100-grade UOE line pipe. The chemical composition is shown in Table 1. The steel was made through thermo-mechanical controlled rolling and an accelerated cooling process. The microstructure was a dual-phase structure

C	Si	Mn	P	S	Ti	N	Others
0.051	0.2	1.95	0.007	0.0015	0.012	0.004	Ni, Cr, Cu, Nb

Table 1 Chemical compositions of steel used in this study

Received March 25, 2010; revised manuscript received by the editors October 15, 2011. The original version (prior to the final revised manuscript) was presented at the 20th International Offshore and Polar Engineering Conference (ISOPE-2010), Beijing, June 20–25, 2010.
KEY WORDS: High-strength steel, anisotropy, damage, ductile fracture.

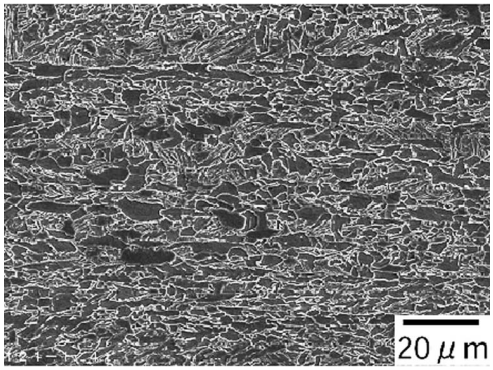

Fig. 1 SEM image of steel used in this study

consisting of fine polygonal ferrite and granular bainite, as shown in Fig. 1.

A plate made by TMCP has, generally speaking, an anisotropic plastic behavior (Tanguy et al., 2008) so that it is important to keep track of the principal material axes. Below, L is the longitudinal direction corresponding to the rolling direction; T, the transverse direction; and S, the short transverse (thickness). D stands for the diagonal direction (45° between direction L and T in the sheet plane).

Large flat tensile specimens (Fig. 2) were machined from the steel plate, in order to pre-strain the material. The specimen was strained up to approximately 6% on a 4000-kN tensile machine. The maximum level of pre-straining is close to the uniform elongation of the tested steel; specimens started necking above this limit. The specimen shape was optimized to make a 200-mm × 300-m zone where applied plastic strain was uniform. Strain gauges were glued on the test specimen to check the pre-strain level. Tensile straining was performed along the T direction, which corresponded to the main pre-straining direction during the UOE pipe forming process.

Table 2 shows the tested plate had anisotropic tensile properties even before pre-straining. Both yield and tensile strength were highest, while elongation was lowest in the T load direction. Regarding plastic deformation behavior, the anisotropy was obvious in the L and T directions, while the isotropy is in the D direction. (See Lankford values in Table 2 or Fig. 3.)

Pre-straining enhanced the anisotropy, as shown in Fig. 3. In the T direction, which was parallel to the pre-strain one, stress immediately reached the ultimate point after more than 4% pre-straining. In the L and D directions, some plastic hardening was kept even after applying the same pre-strain level.

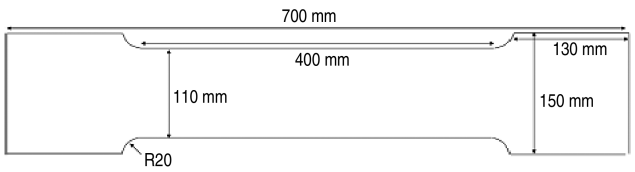

Fig. 2 Schematic illustration of pre-strain test specimen

	T-0%	L-0%	D-0%
YS (MPa)	567	538	500
TS (MPa)	771	741	708
U.EI (%)	9.2	9.8	10.0
T.EI (%)	19	21	22
Lankford	0.67	0.40	1.00

Table 2 Tensile properties of as-received plate in each direction

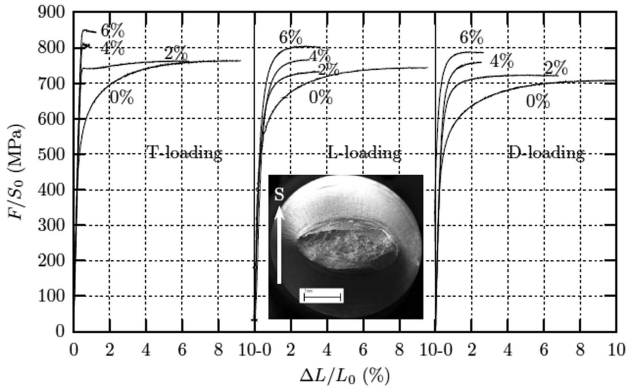

Fig. 3 Stress-strain curves in different directions before and after pre-straining

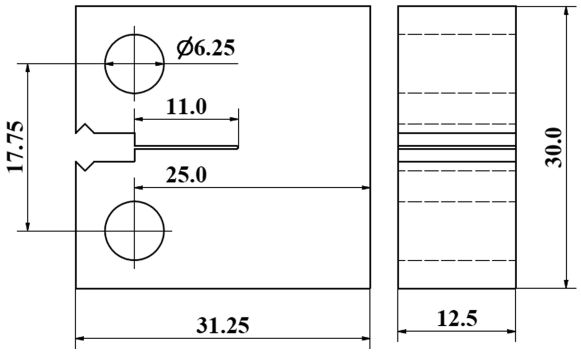

Fig. 4 Schematic illustration of compact testing specimen (units in mm)

The fracture toughness test was carried out along different directions using compact testing C(T) specimens without side grooves, shown in Fig. 4. All tests were carried out at 25°C for the as-received and pre-strained steels. The B of the C(T) specimen was 12.5-mm thick, and the width W was equal to $2B$ (25 mm). All specimens contained notches that were sharpened with fatigue cracks. The crack size was between 0.55 and 0.60 W. The J-Δa resistance curve was determined from which single point the initiation toughness value was evaluated, using multiple samples in accordance with the ASTM-1820 standard. The ductile crack advance was directly measured on a fracture surface of a specimen which was broken at a liquid nitrogen temperature after the toughness test.

FRACTURE TOUGHNESS TESTS USING C(T) SPECIMENS

Anisotropy of Damage Behavior in As-Received Material

Fig. 5 shows J-Δa resistance curves in different directions (L and T) of the as-received steel. The letters L and T identify the orientation of the used fracture toughness specimen; the first letter indicates the load direction, and the second denotes the direction of crack propagation. The tested plate (API-X100) had anisotropic crack growth resistance between the L and T loading directions. Toughness was higher in the L-T configuration than in the T-L configuration. This result was in agreement with experimental results on the ductility of the same plate using smooth and notch tensile specimens (Shinohara et al., 2009).

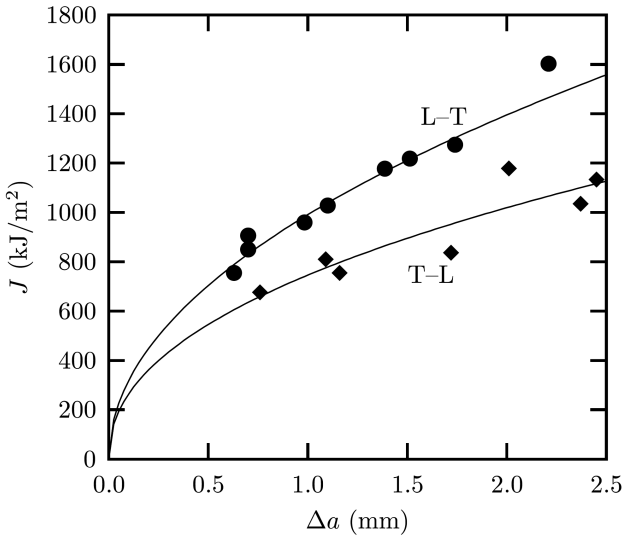

Fig. 5 J-Δa resistance curves of specimens tested along different directions (L and T)

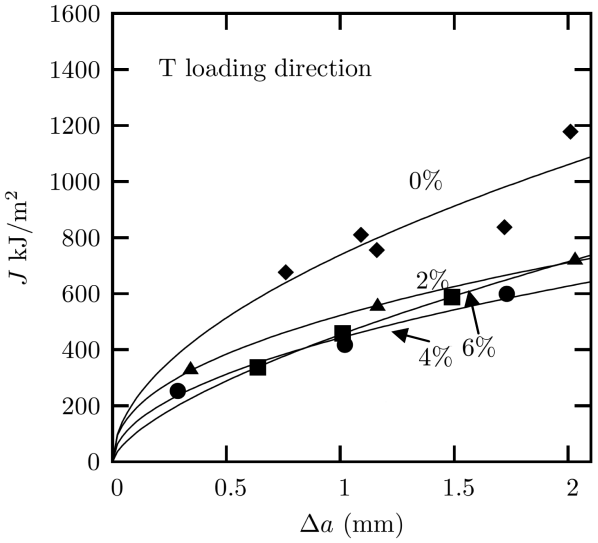

Fig. 7 Crack resistance curves of pre-strained steels in T-L configuration

Effect of Pre-Straining on Ductile Crack Resistance

Figs. 6 and 7 show the effect of pre-strain on crack growth resistance for the L-T and T-L configurations, respectively. It was observed that pre-strain had a large effect on toughness for both load directions. However, in the range of applied strain from 2% to 6%, the change of crack growth resistance was small.

Fig. 8 shows J integral values at a 1-mm crack advance for the as-received and pre-strained materials loaded along the 2 directions. The J value was reduced by about 30% for the L-T configuration, and by 45% for the T-L configuration when pre-strain was applied to 4% and larger. Plus, both slopes appear to be the same; the deterioration of toughness by pre-straining might be independent of the loading direction.

Fractographic Examination

Fracture surfaces close to the crack tips of the entire tested C(T) specimens were observed by SEM. Fig. 9 shows the fracture surfaces in both as-received and pre-strained materials. It was found that the main damage mechanism in the toughness tests was void growth of primary dimples which nucleated at oxides. Also, the average size of dimples in the pre-strained material was almost the same as one of the as-received material. The effect of pre-strain on dimple size might be limited.

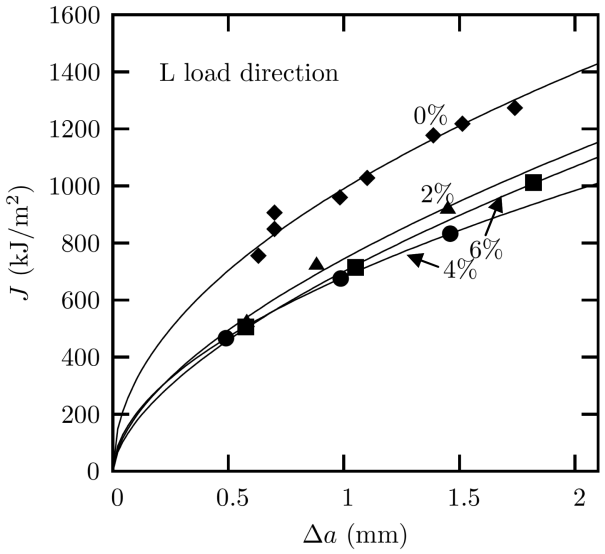

Fig. 6 Crack resistance curves of pre-strained steels in L-T configuration

NUMERICAL ANALYSIS OF ANISOTROPIC TOUGHNESS IN AS-RECEIVED STATE

As noted above, the tested API-X100 steel plate had anisotropy of toughness as well as plasticity. The observed crack advance in the C(T) test coincided with primary void growth and coalescence. Numerical analysis was performed using a unit cell model with a small void, in order to reveal anisotropic void growth.

Constitutive Model

The model used here included the anisotropic yield condition proposed in the previous study (Bron, 2004), which was extended

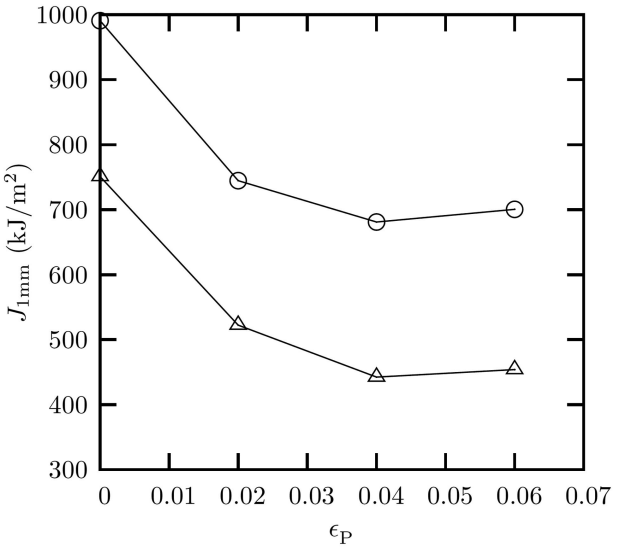

Fig. 8 Change of ductile crack resistance by pre-straining

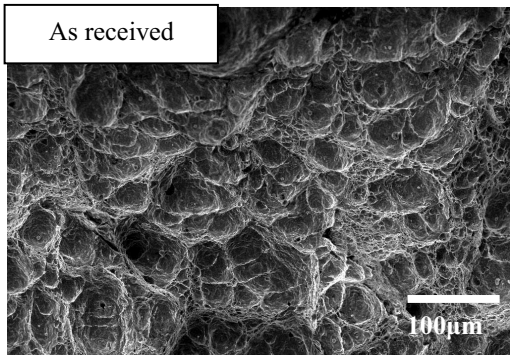

(a) As received material

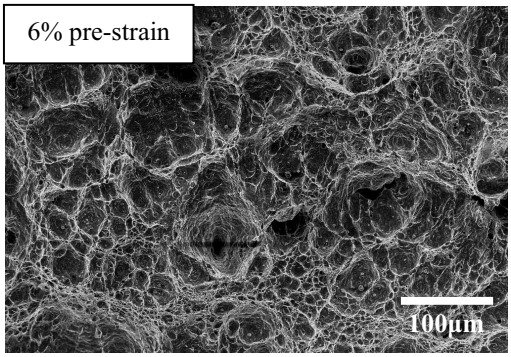

(b) Pre-strained material

Fig. 9 Fracture surfaces of C(T) specimens (LT configuration)

to account for kinematic hardening. In the following, $\underline{\sigma}$ is the Cauchy stress tensor and $\underline{X}$ the back-stress representing kinematic hardening and $\underline{\beta} = \underline{\sigma} - \underline{X}$. The yield function is then defined as:

$$\phi = \beta_E - R(p) \tag{1}$$

where β_E is an equivalent anisotropic stress measure, $R(p)$ the isotropic hardening function expressed as:

$$R(p) = R_0(1 + Q_1(1 - \exp(-k_1 p)) + Q_2(1 - \exp(-k_2 p))) \tag{2}$$

where p is the equivalent plastic strain.

The yield function can describe Lankford coefficients in any direction as well as yield anisotropy. Plastic anisotropy is represented by 12 parameters in the form of two 4th-order symmetric tensors; 4 other parameters influence the shape of the yield surface. The model is based on the definition of an equivalent stress measure defined for any 2nd-order tensor $\underline{a}$ and given by:

$$a_E = (\alpha(\psi^1)^{a/b^1} + (1-\alpha)(\psi^2)^{a/b^2})^{1/a} \tag{3}$$

$$\psi^1 = \frac{1}{2}(|S_2^1 - S_3^1|^{b^1} + |S_3^1 - S_1^1|^{b^1} + |S_1^1 - S_2^1|^{b^1}) \tag{4}$$

$$\psi^2 = \frac{3^{b^2}}{2^{b^2}+2}(|S_1^2|^{b^2} + |S_2^2|^{b^2} + |S_3^2|^{b^2}) \tag{5}$$

where $S^k_{i=1-3}$, $k = 1, 2$ are the principal values of a modified stress deviator $\underline{s}^k$ defined as follows:

$$\underline{s}^k = \underline{\underline{L}}^k : \underline{a} \tag{6}$$

where $\underline{\underline{L}}^k$ is the 4th-order tensor expressed as in the Voigt representation:

$$\underline{\underline{L}}^k = \begin{pmatrix} \frac{c^k_{LL}+c^k_{SS}}{3} & -\frac{c_{SS}{}^k}{3} & -\frac{c^k_{LL}}{3} & 0 & 0 & 0 \\ -\frac{c_{SS}{}^k}{3} & \frac{c^k_{SS}+c^k_{TT}}{3} & -\frac{c^k_{TT}}{3} & 0 & 0 & 0 \\ -\frac{c^k_{LL}}{3} & -\frac{c^k_{TT}}{3} & \frac{c^k_{TT}+c^k_{LL}}{3} & 0 & 0 & 0 \\ 0 & 0 & 0 & c^k_{TL} & 0 & 0 \\ 0 & 0 & 0 & 0 & c^k_{LS} & 0 \\ 0 & 0 & 0 & 0 & 0 & c^k_{ST} \end{pmatrix} \tag{7}$$

The effective plastic strain, p, is defined by the condition:

$$\beta_E \dot{p} = \underline{\beta} : \underline{\dot{\varepsilon}}_p \tag{8}$$

where $\underline{\dot{\varepsilon}}p$ is the plastic strain rate tensor defined by the normality rule:

$$\underline{\dot{\varepsilon}}_p = \dot{p}\frac{\partial \phi}{\partial \underline{\sigma}} \tag{9}$$

The evolution of the back stress tensor is given by the Prager rule (Chaboshe, 1989):

$$\underline{\dot{X}} = \frac{2}{3} C \underline{\dot{\varepsilon}}_p - \dot{p} D \underline{X} \tag{10}$$

The model is complex and has several material parameters to be adjusted: the anisotropic yield function parameters $(a, b_1, b_2, \alpha, c_1^{TT\ldots ST}, c_2^{TT\ldots ST})$ and the isotropic hardening parameters (Q_1, Q_2, b_1, b_2). Below, the model is simplified assuming $a = b_1 = b_2$. The parameter adjustment for the tested steel had already been carried out in the previous work (Shinohara, 2009).

Numerical Analysis of Anisotropic Void Growth

Three-D unit cell calculations (Koplik and Needleman, 1988; Brocks et al., 1995) for different load directions (L and T) were carried out. The 3D mesh is shown in Fig. 10. The unit cell was a cube. The initial porosity f_0 was set at 0.1%. The stress triaxiality was kept constant (1.5) while pulling the cell.

Fig. 11 shows the results of a unit cell calculation in terms of deformation and evolution of void volume fraction in the 2 load

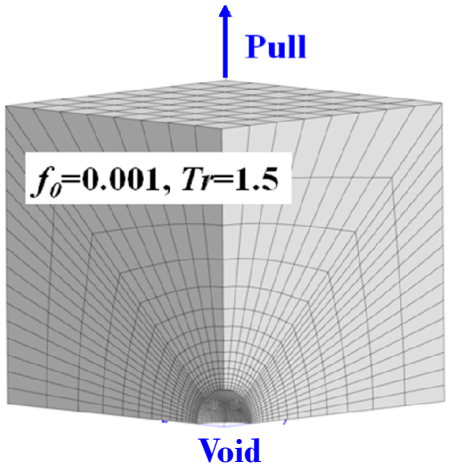

Fig. 10 3D unit cell mesh with cube void

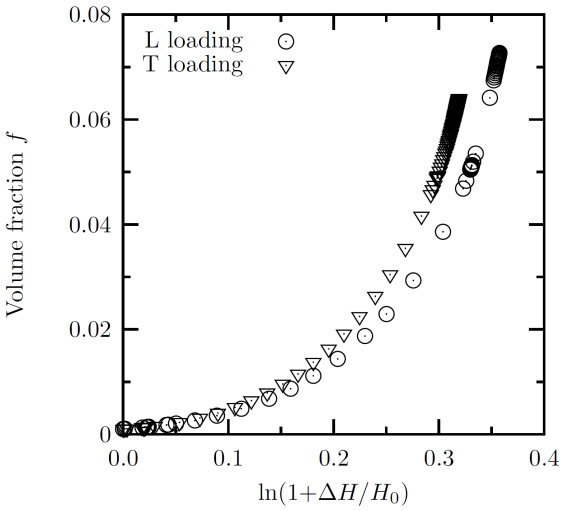

Fig. 11 Change of void growth by loading direction

directions. The volume fraction of void gradually increased in the range of small deformation. When the plastic strain was over 0.3, the void rapidly grew, which correlated with the onset of coalescence. The growth rate depended on the pulling direction. A void grew more quickly in the T load direction than in the L direction. The critical strain of the coalescence is also different between the 2 directions: the value is smaller in the T than in the L load direction. The numerical results are consistent with experimental results. The results also suggest that a new damage model should be developed to account for the anisotropic ductile damage.

PROPOSED DAMAGE MODEL TO REPRESENT ANISOTROPIC DAMAGE BEHAVIOR

High-strength steel line pipe has anisotropic ductile damage as well as plasticity due to the crystallographic texture and pre-straining. The damage model proposed in this study must coincide with the model for anisotropy of plastic behavior in the absence of damage. Additionally, the model must account for ductile failure anisotropy.

Proposed Damage Model

The proposed model is based on the Gurson-Tvergaard-Needleman (GTN) model (Tvergaard, 1990) extended to take into account plastic anisotropy and kinematic hardening (Besson, 2009). In this study, the representation of damage anisotropy is based on the simple phenomenological model given by the previous literature (Morgeneyer et al., 2009). Damage is represented by the void volume fraction f. The model is based on the definition of an effective scalar stress measure a_* expressed as a function of tensor $\underline{a}$ and damage f. It is implicitly defined by solving the following:

$$S(\underline{a}, f, a_*) = \frac{a_E^2}{a_*^2} + 2q_1 f_* \cosh\left(\frac{q_2}{2}\frac{a_K}{a_*}\right) - 1 - q_1^2 f_*^2 \equiv 0 \qquad (11)$$

where f_* is a function of damage introduced to void coalescence. q_1 and q_2 are fitting parameters. The anisotropic stress measure a_E is denoted by Eqs. 3∼7. a_K is used to take into account the anisotropic ductile damage instead of the trace of $\underline{a}$ (Morgeneyer et al., 2009). It is expressed as:

$$a_K = \alpha_{LL} a_{LL} + \alpha_{TT} a_{TT} + \alpha_{SS} a_{SS} \qquad (12)$$

β_* is implicitly defined by:

$$S(\beta_*, \beta_E, \beta_K, f) = 0 \qquad (13)$$

The yield function is then expressed as:

$$\phi = \beta_* - R(p) \qquad (14)$$

where the function $R(p)$ still represents isotropic hardening, which is denoted by Eq. 2. The plastic strain rate tensor is given by the normality rule as:

$$\underline{\dot{\varepsilon}}_p = (1-f)\dot{p}\frac{\partial \phi}{\partial \underline{\sigma}} = (1-f)\dot{p}\frac{\partial \beta_E}{\partial \underline{\sigma}} \qquad (15)$$

So that:

$$\underline{\dot{\varepsilon}}_p : \underline{\beta} = (1-f)\dot{p}\beta_* \qquad (16)$$

Damage growth is described considering void growth and void nucleation on carbides so that:

$$\dot{f} = (1-f)\,\mathrm{trace}(\underline{\dot{\varepsilon}}_p) + A_n \dot{p} \qquad (17)$$

where A_n is the nucleation rate. Primary particles are assumed to de-bond at the onset of plastic strain so that the initial void volume fraction f_0 corresponds to the particles' volume fraction. The evolution law for the back stress $\underline{X}$ has to be modified as detailed in Morgeneyer et al., 2009.

Simulation of C(T) Test for Pre-Strained Steel

Calculations were carried out using quadratic elements with reduced integration. The 3D mesh of a C(T) specimen is shown in Fig. 12.

Fig. 13 shows simulation result of the J-Δa curves for the as-received material loaded in different directions (L and T). J and Δa were computed following the ASTM-1820 standard. Using the proposed damage model with the modified trace a_K, ductile tearing anisotropy was well represented. The J integral value of the L-T configuration was higher than one of the T-L configuration. The simulation results were in agreement with experimental trends for the as-received steel.

Fig. 14 shows simulated J-Δa curves of pre-strained materials in the T-L configuration. As experimentally observed, crack advance resistance decreased with increasing pre-strain level. The pre-strain effect on toughness could be demonstrated, thanks to the extension of the damage model to the kinematic hardening model.

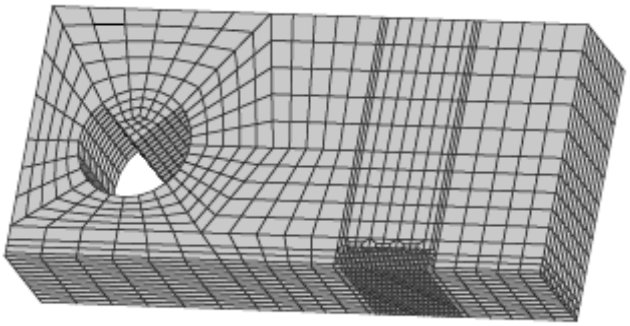

Fig. 12 3D mesh of a C(T) specimen

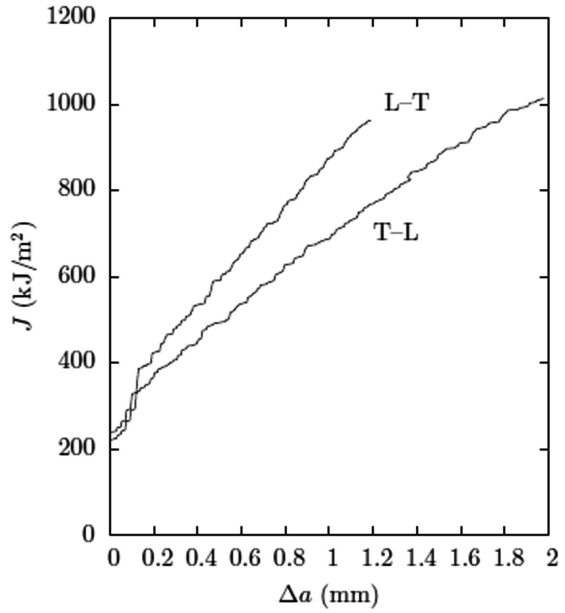

Fig. 13 Simulated J-Δa curves for as-received material

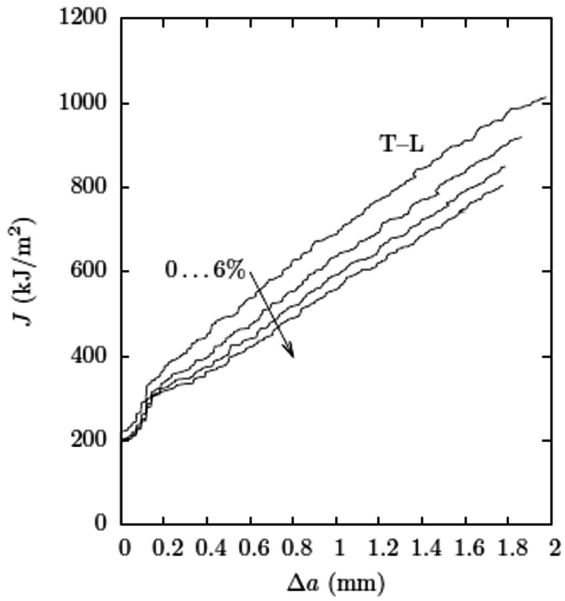

Fig. 14 Simulated J-Δa curves for pre-strained material

Further Work

All parameters in the proposed damage model should be more precisely optimized, in order to get good agreement with all experimental results. The damage model is now applied to other kinds of fracture toughness test, such as the ingle edge notch bend (SENB) and single edge notch tension (SENT) test.

Further, the application will be extended to a numerical analysis of a curved wide plate tensile test and a full-scale pipe tensile test with internal pressure.

CONCLUSIONS

Fracture toughness tests using C(T) specimens were performed along different directions for as-received and pre-strained X100 line pipe steel plates. The new damage model was proposed to represent anisotropic damage behavior. The main results obtained are:

• The experimental test results showed ductile tearing anisotropy in the as-received state; the J integral value in L loading was higher than the one in T loading.

• The experimental test also revealed that pre-strain deteriorated toughness; the J integral value was reduced by about 30% for the L-T configuration and by 45% for the T-L configuration when pre-strain was applied to 4% and larger.

• According to unit cell simulation, the void growth and coalescence, which corresponded to ductile advance, was dependent on the loading direction; the growth rate was faster in T loading than L loading. The result was int agreement with the trend of experimental results.

• The new model was proposed in this study in order to represent ductile damage anisotropy. It was based on the GTN model extended to take into account anisotropic plasticity and kinematic hardening. In addition, it was proposed to phenomenologically describe anisotropic damage growth by replacing the trace of the stress tensor by a modified value. The proposed model could represent pre-strain effect on damage as well as damage anisotropy.

ACKNOWLEDGEMENTS

The authors thank Nippon Steel Corporation for financial support.

REFERENCES

Besson, J (2009) "Damage of Ductile Materials Deforming Under Multiple Plastic or Viscoplastic Mechanisms," *Int J Plasticity*, Vol 25, pp 2204–2221.

Brocks, W, Sun, DZ, and Honig, A (1995). "Verification of the Transferability of Micromechanical Parameters by Cell Model Calculations with Visco-Plastic Materials," *Int J Plasticity*, Vol 11, pp 971–989.

Bron, F, and Besson, J (2004). "A Yield Function for Anisotropic Materials: Application to Aluminum Alloys," *Int J Plasticity*, Vol 20, pp 937–963.

Chaboshe, JL (1989). "Constitutive Equations for Cyclic Plasticity and Cyclic Viscoplasticity," *Int J Plasticity*, Vol 5, pp 243–302.

Glover, A, and Rothwell, B (2004). "Yield Strength and Plasticity of High Strength Pipelines," *Proc Int Pipeline Tech Conf*, Ostend, Belgium, pp 65–79.

Gordon, JR, Zettlemoyer, N, and Mohr, WC (2007). "Crack Driving Force in Pipelines Subjected to Large Strain and Biaxial Stress Conditions," *Proc 17th Int Offshore and Polar Eng Conf*, Lisbon, ISOPE, Vol 4, pp 3129–3140.

Igi, S, Kondo, J, Suzuki, N, Zhou, J, and Duan, D (2008). "Strain Capacity of X100 High-strain Linepipe for Strain-based Design Application," *Proc 7th Int Pipeline Conf*, Calgary, Paper IPC2008-64518.

Koplik, J, and Needleman, A (1988). "Void Growth and Coalescence in Porous Plastic Solids," *Int J Solids and Struct*, Vol 8, pp 835–853.

Morgeneyer, T, Besson, J, Proudhon, H, Starink, M, and Sinclair, I (2009). "Experimental and Numerical Analysis of Toughness Anisotropy in AA2139 Al-Alloy Sheet," *Acta Mater*, Vol 57, No 13, pp 3902–3915.

Shinohara, Y, Hara, T, Tsuru, E, Asahi, H, Terada, Y, and Doi, N (2005). "Change of Mechanical Properties of High Strength Line Pipe by Thermal Coating Treatment," *Proc 24th Int Conf Offshore Mech and Arct Eng,* Halkidiki, Greece, Paper OMAE-67055.

Shinohara, Y, Hara, T, Tsuru, E, Asahi, H, Terada, Y, and Doi, N (2006). "Effect of Tensile Property Distribution on Strain-based Design Application of High Strength UOE Line Pipe," *Proc 25th Int Conf Offshore and Mech and Arct Eng,* Hamburg, Paper OMAE2006-92302.

Shinohara, Y, Besson, J, and Madi, Y (2009). "Effect of Pre-Strain on Ductility in High Strength Line Pipe Steels," *Proc 19th Int Offshore and Polar Eng Conf*, Osaka, ISOPE, Vol 4, pp 146–153.

Tanguy, B, Luu, T, Perrin, G, Pineau, A, and Besson, J (2008). "Plastic and Damage Behavior of a High Strength X100 Pipeline Steel: Experiments and Modeling," *Int J Pressure Vessels and Piping*, Vol 85, pp 322–335.

Thomason, PF (1900). *Ductile Fracture of Metals*, Oxford, Pergamon.

Timms, C, DeGeer, D, and McLamb, M (2005). "Effect of Thermal Coating Process on X100 UOE Line Pipe," *Proc 24th Int Conf Offshore Mech and Arct Eng,* Halkidiki, Greece, Paper OMAE2005-67401.

Tsuru, E, Shinohara, Y, and Asahi, H (2008). "Evaluation Precept for Buckling Resistance of High-Strength UOE Line Pipes Used in Strain-Based Design Applications," *Int J Offshore and Polar Eng*, ISOPE, Vol 18, No 3, pp 176–182.

Tsuru, E, Yoshida, K, Shirakami, S, and Kuwabara, T (2008). "Numerical Simulation of Buckling Resistance for UOE Line Pipes with Orthogonal Anisotropic Hardening Behavior," *Proc 18th Int Offshore and Polar Eng Conf*, Vancouver, ISOPE, Vol 4, pp 104–110.

Tvergaard, V (1990). "Material Failure by Void Growth to Coalescence," *Advances in Appl Mech*, Vol 27, pp 83–151.

Wang, YY, and Liu, M (2007). "The Role of Anisotropy, Toughness Transferability and Weld Misalignment in the Strain-Based Design of Pipelines," *Proc 17th Int Offshore and Polar Eng Conf*, Lisbon, ISOPE, Vol 4, pp 3164–3171.

Effet de pré-déformation sur l'anisotropie du comportement plastique et sur la ténacité d'un acier API X100 pour pipeline

Résumé : Dans le cadre de cette étude, l'influence de la pré-déformation sur l'anisotropie du comportement plastique et sur la ténacité d'un acier API X100 pour pipeline a été abordée. Une étude expérimentale approfondie de la microstructure, des propriétés mécaniques et de l'endommagement du matériaux a été mise en oeuvre. Un modèle phénoménologique anisotrope combinant les écrouissages isotrope et cinématique a été développé dans l'objectif de rendre compte du comportement ductile de cet acier à haute résistance. De plus, un modèle d'endommagement anisotrope a été établi pour représenter l'effet de pré-déformation sur la ductilité et la ténacité de cet acier. L'application des modèles à la flexion sous contrainte illustre, par exemple, l'effet négatif de la pré-déformation sur la charge limite (Moment de flexion maximum) supportée avant flambement du pipe.
Mots clés : X100, anisotrope, pipeline, ductile, endommagement, ténacité, flambement.

Prestrain effect on anisotropic ductile damage in API grade X100 line pipe steel

Abstract: In this thesis the influence of prestrain on anisotropic ductility and fracture toughness has been evaluated for API grade X100 line pipe steel. A comprehensive experimental investigation of microstructure, mechanical properties and fracture mechanisms has been carried out. A phenomenological model combining isotropic and kinematic hardening with anisotropic yield function has been developed, in order to represent anisotropic hardening behavior of the high strength steel. Additionally, a damage model incorporating anisotropic damage has been established for representation of prestrain effect on ductility and toughness of the X100 steel. The developed models could predict the bending capacity and the ductile fracture toughness of the cold-formed line pipes.
Keywords: X100, anisotropy, line pipe, ductile, damage, toughness, buckling.

この論文では、APIグレードX100ラインパイプ用鋼に対して延性および破壊靭性の異方性に及ぼす予ひずみの影響を評価した。組織解析、機械的特性調査および破壊力学的検討を行った。異方性降伏関数を含んだ移動硬化則モデルを開発し、高強度鋼の異方硬化特性を表現可能とした。加えて、異方ダメージモデルを開発し、X100ラインパイプ用鋼の延性および破壊靭性に及ぼす予ひずみの影響を表現可能とした。これら開発モデルは冷間成形された鋼管の曲げ変形能および延性破壊抵抗の予測技術として期待される。

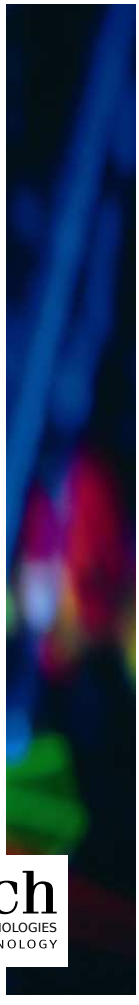

MINES ParisTech

ParisTech
INSTITUT DES SCIENCES ET TECHNOLOGIES
PARIS INSTITUTE OF TECHNOLOGY